UNIVERSITY OF SOUTHAMPTON

DYNAMICS OF HYDROGEN INTERACTION ON AND IN URANIUM

A thesis submitted to the University of Southampton in support of candidature for the degree of Doctor of Philosophy

by Scott Gordon Bazley

School of Chemistry

Sep 2004

UNIVERSITY OF SOUTHAMPTON

ABSTRACT

FACULTY OF ENGINEERING, SCIENCE AND MATHEMATICS

SCHOOL OF CHEMISTRY

Doctor of philosophy

DYNAMICS OF HYDROGEN INTERACTION ON AND IN URANIUM

by Scott Gordon Bazley

The adsorption of hydrogen on polycrystalline uranium surfaces, with modified oxygen overlayers, has been investigated using supersonic molecular beams, TPD and XPS techniques. An indirect channel dominated hydrogen adsorption on clean uranium with an absolute sticking probability of 8.6×10^{-2}. This produced a single second order desorption peak (α_1) in the TPD spectrum at 450 - 410 K that had a saturation coverage of 0.22 ML. The activation energy of desorption was calculated to be 74.58 ± 7 kJmol^{-1}. In contrast, an activated direct channel dominated the adsorption of hydrogen on oxidised uranium surfaces with an absolute sticking probability of 1×10^{-2}. The TPD spectra exhibited three desorption peaks at 250 (β_2), 470 (β_1) and 650 – 610 (β_3) K. These were attributed to weakly bonded hydroxyl groups that were affected by the presence of subsurface metal regions, to desorption from the oxide and to the presence of defects or edges on the oxide that increased the strength of the hydrogen bonding to the surface respectively. The "initial" surface also exhibited three desorption peaks, with a fourth being observed at 63 meV, as an additional peak (α_3) growing as a shoulder on the β_2 peak at 350 K. This was attributed to either edge effects or the population of unfavourable sites near the metal/oxide interface.

Using the Time Lag method, we have investigated the role of the uranium oxide overlayer in the permeation of deuterium through 0.178 and 1 mm thick uranium metal membranes. Palladium coating the inlet surface enabled permeation through "clean" metal to be investigated. There appears to be a number of factors that control the level of influence the oxide overlayer is seen to have on the diffusion process; the thickness of the oxide overlayer, the thickness of the metal membrane, the microstructure of the oxide overlayer and the level of impurities in the gas-phase and the bulk. The only consistent factor between Sets was the calculated apparent activation energy of deuterium diffusion (~27 – 35 kJmol^{-1}), which is associated with diffusion through uranium metal. It is expected that the deuterium species diffuse down low-energy pathways in the oxide overlayer, i.e. grain boundaries or line defects, rather than through oxide lattice sites. The diffusing deuterium species must fill all available surface and bulk trap sites before passing into the uranium metal. Once in the metal, the diffusion of deuterium becomes a relatively facile process.

Acknowledgements

First of all, I would like to thank AWE plc. for financially supporting this research project. I would also like to thank Prof. Brian Hayden for giving me the opportunity to work within his research group. Thanks also to Dr. Tim Nunney for answering my many questions and initiating me into the world of surface science and Dr. Joe Glascott for his informative discussions regards the permeation reaction.

A big thanks has to go to members of the Hayden Group (past and present) who made my time in Southampton enjoyable and memorable; in no particular order: Mike (an invaluable source of information, not all of it useful!), Oli (sarcasm, it's a wonderful thing!), Claire (the only person I know to throw their toys more than me!), Pete Stone and Lefteris (for introducing me to the joys of curry), Nauro, Sam, Ben, Chris Lee, Peter Suchsland, Raf, Alex and Duncan. A mention also has to go to the members of the Russell Group; Abi (elves!!), Helen, Richard, Colin, Peter Wells and Chris.

One of my biggest thanks has to go to the Mechanical Workshop (Rob, Dave, Alan and Jon), without whom my rig would still be sat in the corner of a lab!

Finally, I would like to thank three people; my parents, for always being at the end of the phone when things went wrong, and Laura, whose unwavering support and motivation has helped me through the last few years.

Table Of Contents

Abbreviations

Acronyms

UHV	Ultra-High Vacuum
PES	Potential Energy Surface
QMS	Quadrupole Mass Spectrometer
TSP	Titanium Sublimation Pump
LEED	Low Energy Electron Diffraction
XPS	X-ray Photoelectron Spectroscopy
TPD	Temperature Programmed Desorption
IMFP	Inelastic Mean Free Path
AES	Auger Electron Spectroscopy

Symbols

z	Molecule-surface separation
σ	Molecular bond length at zero potential energy
ε	Well depth at equilibrium separation
r	Molecular bond length
E_L	Energy of the dispersion forces
μ	Dipole moment
α	Polarisabillity of a species
E_{DP}	Energy of the dipole-dipole forces
S	Sticking probability / Solubility
S_0	Initial sticking probability
μ_i	Chemical potential of a substance (i)
G	Gibbs free energy
n_i	Amount of component i
T	Temperature
P	Pressure
a	Activity of a solute
μ_0	Constant depending only on temperature
R	Gas constant
c	Concentration of a substance
J	Flux
D	Diffusion coefficient
P_n	Region of high pressure

P_b	Region of low pressure
H_0	Stagnation enthalpy
m	Mass of a gas molecule
v	Velocity of a gas molecule
M	Mach number
x_M	Position of the Mach disk
d	Nozzle diameter / Detected sampling depth
τ	Ratio of the number of required number of collisions (Z) to the collision frequency (υ) / Residence time of the adsorbed species
dH	Change in enthalpy
C_p	Molar heat capacity at constant pressure
C_v	Molar heat capacity at constant volume
U	Internal energy
k_B	Boltzmann constant
F_0	Flux due to the background
S_P	Pumping speed
F_b	Flux due to the beam
F_d	Fraction of diffusely scattered molecules
θ	Surface coverage / Angle of the detector from the surface normal
θ_{sat}	Saturation coverage
E_{BE}	Binding energy
E_{KE}	Kinetic energy
ϕ	Work function of a solid
λ_m	Inelastic mean free path in monolayers
a	Monolayer thickness
N	Avogadro's number
ρ	Bulk density
n	Kinetic order of a reaction
E_{des}	Activation energy of desorption
v	Frequency factor
Q_t	Total amount of gas permeating through the membrane in time t
l	Thickness of the membrane
L	Time lag / Langmuir
A	Area of the membrane
J_0	Specific permeability
E_D	Activation energy of diffusion

Chapter 1: Introduction

1.1 Introduction

Many important chemical reactions are influenced by the actions of a surface, with nearly all industrial applications of chemistry requiring some consideration of surface chemistry. The development of ultra-high vacuum (UHV) in the early 1960's allowed clean, well-defined surfaces to be studied for the first time. This high degree of environmental control allows the fundamental processes of many reactions to be accurately probed. One such interaction is the role of surface contaminants, such as CO or O_2, which will often block active surface sites decreasing rates of reaction [1].

Uranium has an extremely high affinity for oxygen and in most technical situation there will be a surface overlayer of uranium oxide present [2]. This thesis will attempt to further elucidate the mechanism for hydrogen interaction with uranium and the role of the uranium oxide overlayer. This thesis will comprise of two parts; initially the influences of the oxide overlayer upon the dynamics of surface hydrogen interactions will be studied using temperature programmed desorption (TPD) and supersonic molecular beam experiments. Next, the Time-Lag method will be used to study the permeation characteristics of deuterium diffusion through uranium membranes of varying thickness and oxide coverage.

1.2 Potential Energy Surfaces

The interaction between atoms, or molecules, can be described using potential energy surfaces (PES) or diagrams. The one-dimensional Lennard-Jones model [3] can be used to represent the change in potential energy as an atom, or molecule, approaches a surface, shown in Figure 1.1.

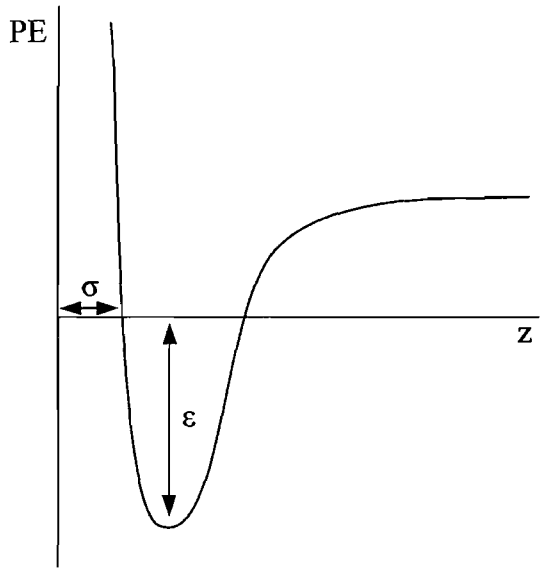

Figure 1.1 – Lennard-Jones one-dimensioanl Potential Energy Model.

where, z is the molecule-surface separation, σ is the bond length at zero potential energy and ε is the well depth. The zero-point of a system refers to the energy of the system when the molecule is infinitely far from the surface. However, this model is a simplification and does not account for the site of impact on the surface, the rotational orientation or the molecular bond length. Therefore, it is desirable to increase the model to two-dimensions, where the potential energy is a function of the molecular bond length (r) and molecular-surface separation, Figure 1.2 [4]. The PES consists of two channels connected by an elbow. The entrance channel represents the impinging molecule, while the exit channel represents the adsorbed molecular state. The transition from gas molecule to adsorbed atoms occurs at the saddle point. Molecules impinging on the surface with translational energies below the saddle-point will be simply reflected away, while molecules with sufficient energy will enter the channel and dissociate. For a non-activated system the saddle point occurs below the zero point energy. This leads to a high dissociation probability that extends to zero incident energy. If the adsorption process is activated then the saddle point will be above the zero point energy for the system and create a barrier. If this barrier occurs early within the reaction coordinate then dissociation is enhanced by the translational energy of the molecule. Whereas an increase in vibrational energy will enhance dissociation when the barrier is within the exit channel, a late barrier [5].

The two dimensional PES model also has its limitations. It ignores the site of impact on the unit cell, moving across the unit cell can lead to a change in the z position of the saddle point (geometric corrugation). This may also lead to a variation in the magnitude of the barrier (energetic corrugation). The role of parallel momentum is also ignored by the two-dimensional PES. Parallel momentum can couple with geometric corrugation to aid dissociation. However, parallel momentum on an energetically corrugated surface will decrease the time available for the dissociation barrier to be overcome [6].

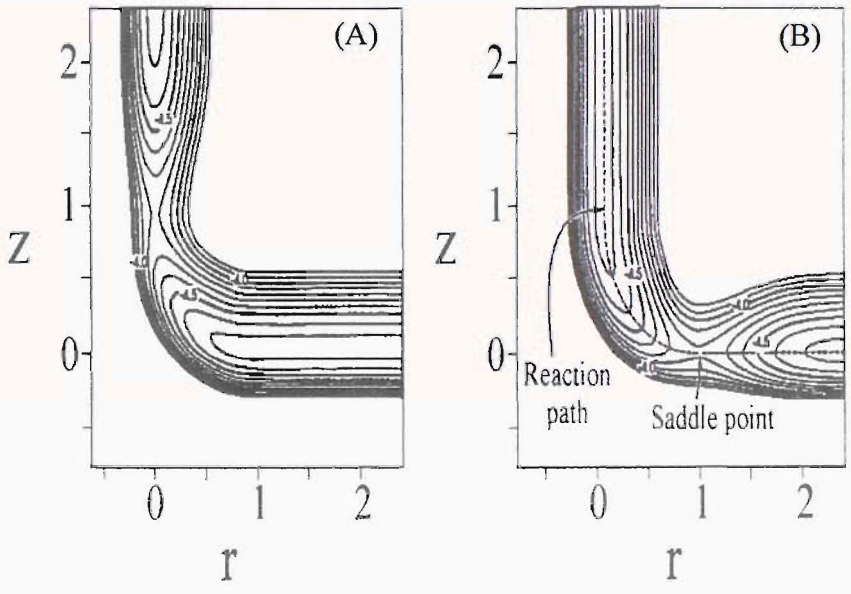

Figure 1.2 – Two-dimensional Potential Energy Surfaces (PES) depicting (A) – an early barrier and (B) – a late barrier to dissociation.

1.3 Adsorption on Surfaces

A molecule can interact with a surface via two types of adsorption processes. Physical adsorption (physisorption) and chemical adsorption (chemisorption) differ in many ways, such as the strength of the adsorbate-surface bond and desorption temperature, which will be discussed below.

1.3.1 Physisorption

Physisorption is the non-reactive adsorption of atoms, or molecules, onto a surface resulting from van der Waals forces. These are weak long-range interactions, with the adsorbate residing in a shallow potential energy well. Van der Waals forces can be split into two distinct groups. The universal dispersion forces, or London forces, arise from instantaneous fluctuations in the electronic distribution of an atom, or molecule. The resulting temporary dipole induces a dipole in an adjacent atom, or molecule, which leads to an attractive force being experienced between the two. The resulting energy (E_L) can be calculated by:

$$E_L \propto -\frac{\mu_1 \mu_2}{r^3} \qquad \text{Equation 1.1}$$

where μ_1 and μ_2 are the dipole moments of the two species and r is the bond length. The second group are dipole forces, which occur when a molecule containing a dipole approaches a second molecule that may, or may not, have a dipole itself. The attractive force (E_{DP}) experienced is proportional to:

$$E_{DP} \propto -\frac{\alpha_2 \mu_1^2}{r^6} - \frac{\alpha_1 \mu_2^2}{r^6} \qquad \text{Equation 1.2}$$

where α is the polarisability of the species. Physisorption is non-surface specific, with the trapped species occupying an area dependent on its size. A molecule approaching a surface will become accelerated due to the attractive potential. As it approaches more closely, repulsive forces due to the Pauli exclusion principle become more dominant. For it to become successfully trapped on the surface it must lose sufficient kinetic energy to either the surface or to another degree of freedom. The ability of a surface to successfully trap an impinging molecule is modelled using the classical hard-cube model, which is discussed in detail in Appendix A.

1.3.2 Chemisorption

Chemisorption occurs when specific electronic orbitals on the adsorbate form a chemical bond with the surface. The strength of the bond formed is highly surface specific and will vary from metal to metal and between surface planes.

The chemisorption of a molecule onto a surface may occur through either dissociative (the molecular bonds break as that molecule binds to the surface) or associative adsorption (the molecule stays intact during binding). Dissociative adsorption is often the critical step in many catalytic reactions and it is therefore one of the most important reactions in surface chemistry. This mechanism is comprised of a direct and an indirect channel. The channel in which a molecule will adsorb is dependent on the PES of the gas-surface interaction, however it is possible for both mechanisms to be accessible on the same surface.

1.3.2.1 Direct Dissociation

Direct dissociation is said to have occurred when a molecule's bonds are broken on collision with a surface. The speed at which this process occurs means that there is insufficient time for the adsorbed molecules to come into thermal equilibrium with the surface; therefore, they will exhibit almost no surface temperature dependence. Thus, the adsorption characteristics will reflect the initial state of the impinging molecule (orientation and energy) and the type of PES experienced during collision. However, the direct dissociation process will be dependent on the number of surface sites available for dissociation. In 1918, Langmuir proposed a model for this coverage dependence [7], which assumed that two adjacent sites were necessary for a diatomic molecule to dissociate. If the number of unoccupied sites is equal to $(1-\vartheta)$, where ϑ is the surface coverage, then the sticking probability (S) is:

$$S \propto (1-\vartheta)^2 \qquad \text{Equation 1.3}$$

The dissociation of a first order process showing $(1-\vartheta)$ dependence occurs at a single surface site with one of the products migrating to another surface site before adsorbing [8].

Direct dissociation can be either activated or non-activated depending the position of the energy barrier relative to the zero-point energy level, discussed in Section 1.2. Both mechanisms will experience an increase in the dissociation probability with increasing incident kinetic energy, due to the greater accessibility of non-optimised trajectories.

1.3.2.2 Indirect Dissociation

It is often the case that the impinging adsorbate molecule does not dissociate upon impact but becomes trapped on the surface in a precursor state. The adsorbed molecule will be mobile across the surface until it finds a favourable geometry or surface site, such as a step or defect, whereby dissociation can occur. This is known as indirect dissociation. There are many experimental examples of systems, which exhibit precursor mechanisms; including H_2 on Pt(533) [9] and Ni(111) [10]. The magnitude of the molecules mobility depends upon the relative strength of the precursor bond, whether physisorbed (high mobility) or chemisorbed (low mobility). The precursor can be either intrinsic (requiring a free surface site to adsorb) or extrinsic (forming on top of an adsorbate covered surface). Intrinsic precursors are characterised by an initial sticking probability (S_0) that decreases with increasing surface temperature, while extrinsic precursors are independent of both surface temperature and coverage.

In contrast to the direct dissociation channel increasing the energy of the incident molecule, or the surface temperature, will lead to a decrease in the sticking probability. In order for a molecule to become trapped it must dissipate energy on collision. This can be achieved by either excitation of surface phonons or by the non-adiabatic excitation of electron-hole pairs. If the molecule has more energy than can be transferred in these ways then the molecule cannot become trapped and will be scattered away from the surface.

1.4 Diffusion

Diffusion is defined as the migration of particles down a concentration gradient [11]. The different substances will mix as a result of the random motion of their component atoms, ions and molecules. Within this mixture the chemical potential (μ_i) of a substance (i) is defined as the partial Gibbs free energy [12]:

$$\mu_i = \left(\frac{\partial G}{\partial n_i}\right)_{T,P,n} \qquad \text{Equation 1.4}$$

where, G is the Gibbs free energy, n_i is the amount of component i, T and P are temperature and pressure, and n is the amount of other component in the mixture. The chemical potential can be related to the activity of a solute (a) by:

$$\mu = \mu_0 + RT \ln a \qquad \text{Equation 1.5}$$

where μ_0 is a constant depending only on temperature and R is the gas constant. If the solution is not uniform then the change in the chemical potential along the x-direction will be:

$$\left(\frac{\partial \mu}{\partial x}\right)_t = \frac{RT}{c}\frac{\partial c}{\partial x}\frac{\partial \ln a}{\partial \ln c} \qquad \text{Equation 1.6}$$

where c is the concentration of the substance. If it is assumed that the flux (J) is proportional to the gradient of the change in chemical potential, $J \propto (\partial\mu/\partial x)$, then Equation 1.6 becomes:

$$J = -D\frac{\partial c}{\partial x}\frac{\partial \ln a}{\partial \ln c} \qquad \text{Equation 1.7}$$

where D is the diffusion coefficient. If the activity coefficient (a/c) is constant then,

$$\frac{\partial \ln a}{\partial \ln c} = \frac{c}{a}\frac{\partial a}{\partial c} = 1$$ Equation 1.8

substituting Equation 1.8 into Equation 1.7 leads to,

$$J = -D\frac{\partial c}{\partial x}$$ Equation 1.9

This is known as Fick's first law of diffusion. The flux of a diffusing species will be from high to low concentration, with the flux being proportional to the concentration gradient at that point. This is shown schematically in Figure 1.3.

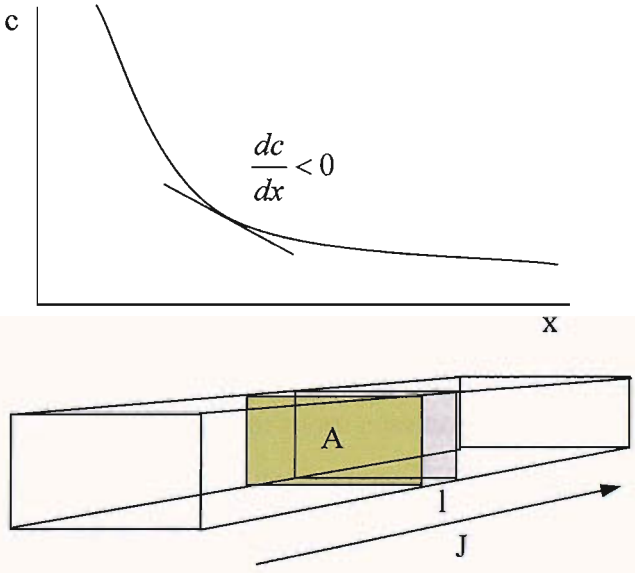

Figure 1.3 – Flux of particles down a concentration gradient through an area (A).

If we now consider the time dependency of diffusion, then the amount of particles entering the volume Al in the time dt is $JAdt$. If the initial volume concentration is c, then the increase in concentration due to the incoming particle flux is:

$$\frac{\partial c}{\partial t} = \frac{JAdt}{Aldt} = \frac{J}{l}$$ Equation 1.10

The corresponding decrease in volume concentration due to the outgoing flux (J'):

$$\frac{\partial c}{\partial t} = -\frac{J' A dt}{A l dt} = -\frac{J'}{l} \qquad \text{Equation 1.11}$$

therefore, the net change in volume concentration is:

$$\frac{\partial c}{\partial t} = \frac{J - J'}{l} \qquad \text{Equation 1.12}$$

Both the incoming and outgoing fluxes are proportional to the concentration gradients at their respective positions. So, from Fick's first law (Equation 1.9):

$$J - J' = -D\frac{\partial c}{\partial x} + D\frac{\partial c'}{\partial x} = -D\frac{\partial c}{\partial x} + D\frac{\partial}{\partial x}\left(c + \frac{\partial c}{\partial x} l\right) = Dl\frac{\partial^2 c}{\partial x^2} \qquad \text{Equation 1.13}$$

substituting Equation 1.13 into Equation 1.12 gives:

$$\frac{\partial c}{\partial t} = D\frac{\partial^2 c}{\partial x^2} \qquad \text{Equation 1.14}$$

This is known as Fick's second law, or more commonly the diffusion equation, and is only valid if D is not a function of concentration. Equations 1.9 and 1.14 are the fundamental diffusion equations from which solutions for different geometries, diffusion with chemical reaction and diffusion with D as a function of concentration can be calculated [12-14].

1.5 References

[1] Gee, A.T., B.E. Hayden, C. Mormiche, T.S. Nunney, Surf. Sci. 512 (2002) 165-172.

[2] Weigel, F., in: J.J. Katz, G.T. Seaborg, L.R. Morss (Eds.), The Chemistry of the Actinide Elements, London, New York, 1986, pp. 169-442.

[3] Lennard-Jones, J., Trans.Far.Soc. 28 (1932) 334.

[4] Halstead, D., S. Holloway, J. Chem. Phys. 93 (1990) 2859-2870.

[5] Hayden, B.E., C.L.A. Lamont, J.Chem.Soc.Faraday Diss. (1991) 415-423.

[6] Darling, G.R., S. Holloway, Surf.Sci. 304 (1994) L 461-L 467.

[7] Langmuir, I., J. Am. Chem. Soc. 40 (1918) 1361.

[8] Alnot, P., A. Cassuto, D.A. King, Surf.Sci. 215 (1989) 29-46.

[9] Gee, A.T., B.E. Hayden, C. Mormiche, T.S. Nunney, J. Chem. Phys. 112 (2000) 7660-7668.

[10] Rendulic, K.D., A. Winkler, H.P. Steinruck, Surf. Sci. 185 (1987) 469-478.

[11] Atkins, P.W., Physical Chemistry, Oxford, Oxford University Press, 1998.

[12] Doremus, R.H., Diffusion of Reactive Molecules in Solids and Melts, New York, Wiley, 2002.

[13] Jost, W., Diffusion in Solids, Liquids, Gases, New York, Academic Press, 1952.

[14] Crank, J., The Mathematics of Diffusion, Oxford, Oxford University Press, 1975.

Chapter 2: Experimental Instrumentation

2.1 Supersonic Molecular Beam Ultra-High Vacuum System

All of the experiments carried out in Chapter 4 were performed under UHV conditions in the system described below, shown in Figure 2.1. The system consisted of three chambers. The first chamber contained the nozzle and skimmer assembly for supersonic molecular beam generation, see Sections 2.1.3 and 3.1 for more details. The second chamber housed the mechanical chopper system for beam modulation, not used within this thesis. Both chambers one and two were pumped by Edwards EO6 6" oil diffusion pumps (1000 ls^{-1}), with water-cooled baffles, which were backed by an Edwards E2M40 rotary pump and an Edwards E2M18 respectively. The third chamber was the main reaction chamber. Leybold turbo molecular pumps, a 1000 ls^{-1} and a 51 ls^{-1}, pumped the main reaction chamber and the differentially pumped rotatable quadrupole mass spectrometer (QMS) respectively. An Edwards EO4 oil diffusion pump and an Edwards E2M18 rotary pump provided backing for both turbo pumps. The main chamber also housed a titanium sublimation pump (TSP, VG), to aid pumping. The base pressures for each of the chambers were $1x10^{-7}$, $1x10^{-8}$ and $<1x10^{-10}$ mbar respectively and these were achieved by baking the entire system for 24 hours at 393 K.

For surface analysis the main chamber housed low energy electron diffraction (LEED) optics (4-grid rear view, Omicron) and a twin anode (Mg/Al) X-ray source with Clam 2 analyser (VG) for X-ray photoelectron spectroscopy (XPS). A fixed QMS (VG Quartz 200D) was employed for residual gas analysis, King and Wells sticking experiments and temperature programmed desorption (TPD) experiments. A rotatable QMS (VSW) was available for time-of-flight and scattering experiments (not performed here).

The main chamber was also equipped with argon ion bombardment facilities (IonTech) and a gas dosing line, connected to a 3 mm diameter stainless steel

capillary, which allowed gases to be dosed directly onto the front surface of the sample.

Gas flow into the beam line was regulated through three flow controllers (Bronkhurst). This allowed reactant gases to be accurately seeded in noble gases, such as argon, neon and helium.

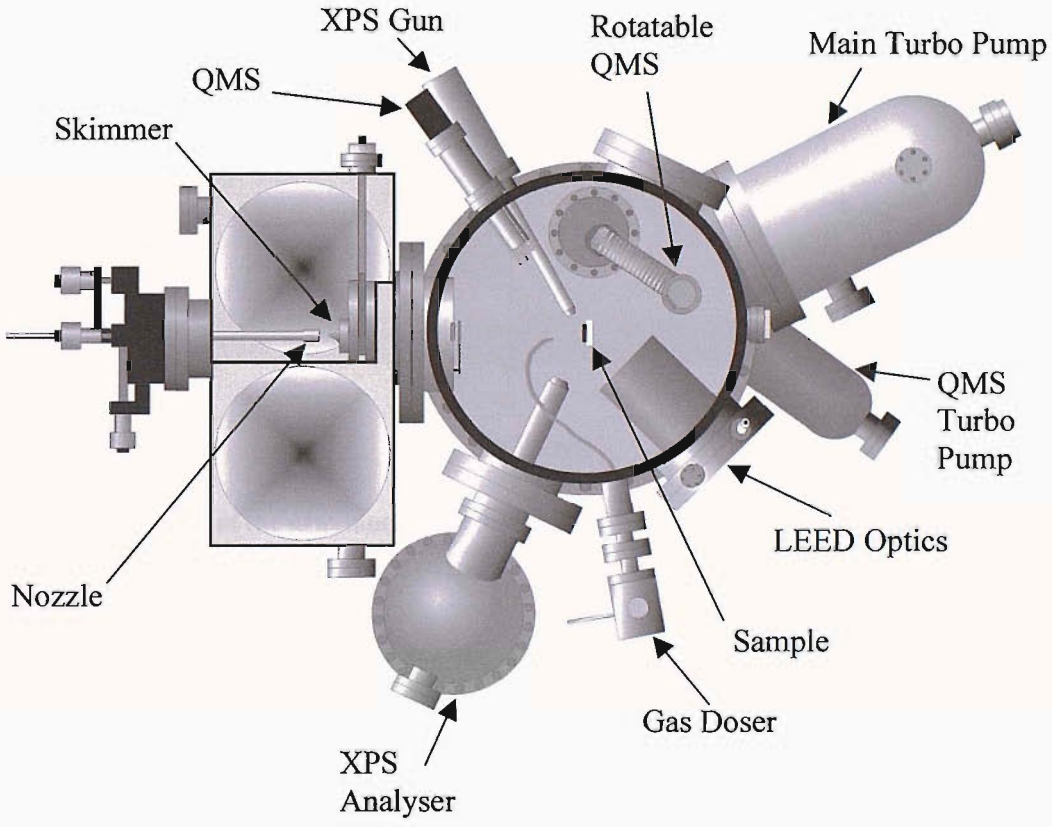

Figure 2.1 - Schematic of the supersonic molecular beam UHV system

2.1.1 Sample Mounting

AWE plc. Aldermaston provided the polycrystalline depleted uranium sample used throughout Chapter 4. The sample had a surface area of 10x10 mm^2 and was approximately 2 mm thick. Shown in Figure 2.2, is a schematic of the uranium sample holder.

Two tungsten wires (0.25 mm diameter) were spot-welded directly onto the rear of the sample. In turn, these wires were spot-welded to the tops of the nickel support bars. Between these bars and the oxygen-free copper support were thin slivers of mica that ensured thermal conductivity while electrically isolating the sample. A K-type thermocouple was spot-welded directly onto the back of the sample allowing accurate temperature measurements to be made.

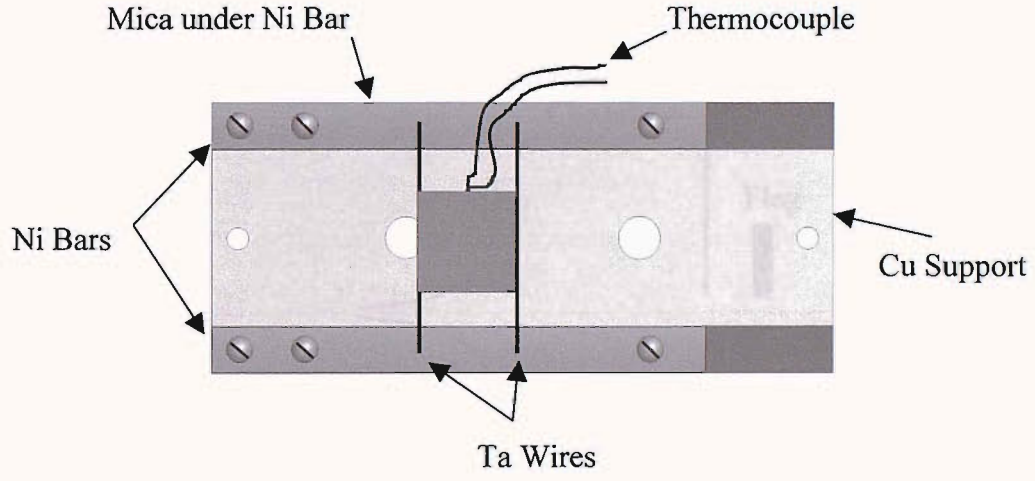

Figure 2.2 - Schematic of the uranium sample holder

The copper support was mounted on the end of a standard xyzθ-shift rotatable manipulator, which had a cold finger running down its centre that allowed the sample to be cooled with liquid nitrogen. This arrangement allowed the sample temperature to be varied from approximately 160 K – 900 K. Higher temperatures were obtainable but were not reached due to the irreversible uranium α to β phase change that occurs at 935 K.

2.1.2 Sample Cleaning

Uranium has an extremely high affinity for oxygen. Even under UHV conditions the surface will become oxidised within several hours. Therefore, intensive cleaning procedures were necessary in order to produce an oxygen-free surface. The procedure used involved alternate hot (600 K) and cold (293 K) argon ion

bombardment cycles, with 3 - 4 keV ions. The cleanliness of the surface was followed by XPS of the U $4f_{7/2}$ region. Extensive thermal vacuum annealing was not used as a cleaning procedure due to the observed oxide redistribution that can occur; see section 4.3.1 for further details. However, flash annealing to 810 K was used to reorder and test the stability of the surface formed.

2.1.3 Supersonic Molecular Beam Source

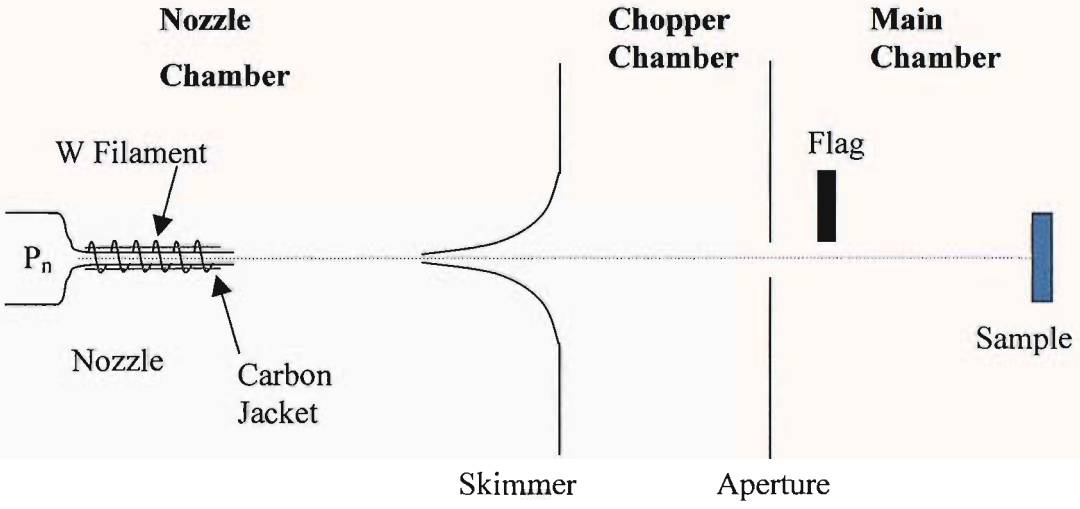

Figure 2.3 - Schematic of the supersonic molecular beam source.

Shown in Figure 2.3 is a schematic of the supersonic molecular beam source used throughout Chapter 4. The nozzle consisted of a quartz tube, which terminated in a 30 μm hole. Around this, thin sheets of carbon were wound to form a jacket about 3 mm thick that ensured even heating over the whole length of the nozzle. Fixed between the nozzle and the carbon jacket was a K-type thermocouple, which was used for all the nozzle temperatures. It was mounted on a manipulator with xyz translations and xy tilt capabilities, allowing accurate alignment with the skimmer, a stainless steel cone with a 300 μm aperture. The cone was designed to allow only the central line of the beam through and to deflect away any background gas without creation of shockwaves around it, see Section 3.1 for more details. The skimmer also had xy translations for alignment purposes. Between the chopper chamber and the main chamber was a variable collimating aperture, constructed from a stainless steal plate. The diameter of the aperture could be varied between 0.5, 1.3, 3 or 4

mm by moving the plate to the corresponding hole. Thus, allowing the diameter of the beam spot on the sample surface to be varied. All the experiments in Chapter 4 used the 1.3 mm aperture, which produced a beam spot of ca. 3 mm on the sample's surface. Also shown is the position of the flag. The flag comprised of a sheet of mica mounted on an arm that could be lowered to block the beam path.

2.2 Permeation Ultra-High Vacuum System

The experiments in Chapter 5 were performed in a UHV system that had been specifically designed and constructed for this investigation. It had been specifically designed to have a fast pumping speed and contain a differentially pumped QMS, with direct line of sight from the sample to the detector. A schematic of the system that was built is shown in Figure 2.4. It consisted of two chambers that were pumped by two Pfeiffer turbo molecular pumps, a 170 ls^{-1} beneath the QMS chamber and a 450 ls^{-1} beneath the reaction chamber. An Edwards E2M8 rotary pump provided backing for both of the turbo pumps. The reaction chamber also contained a TSP, which helped to increase the effective pumping speed. The system was not baked due to reoccurring problems that manifested themselves during bake-out. Nevertheless, the base pressure of the system was $<1x10^{-9}$ mbar. During a typical experiment the background pressure in the QMS chamber rose to approximately $5x10^{-9}$ mbar. This can be attributed to the degassing of the support and also to a possible build up in gas, within the UHV system, due to the relatively poor hydrogen compressibility of the turbo pumps. This change in the background pressure could have obscured any increase in pressure due to the flux of permeating molecules. However, this was not found to be the case with the permeating gas being easily distinguishable from the background. In all calculations it has been assumed that the background pressure was constant during the experiments.

The QMS chamber had a reinsertion arm, which protruded approximately 120 mm into the reaction chamber. Attached to the end of this arm was a 20 mm diameter tube that extended a further 60 mm into the chamber. At the end of this tube was a removable plate that had a 3 mm collimating aperture in its centre. The purpose of

the extension tube was to move the aperture, into the QMS chamber, closer to the centre of the reaction chamber and the sample, without interfering with the rotation of the sample holder. Thus, increasing the sensitivity of the QMS to the detection of desorbing molecules, by reducing the amount of background gas detected during experiments. The windows around the chamber allowed the sample to be lined up with the instrumentation within. The gas dosers were connected to a 3 mm diameter stainless steel capillary within the chamber, which had been angled towards the front face of the sample to allow gases to be dosed directly onto the surface. The ion gun allowed surface cleaning by argon ion bombardment to be performed, not used within this thesis.

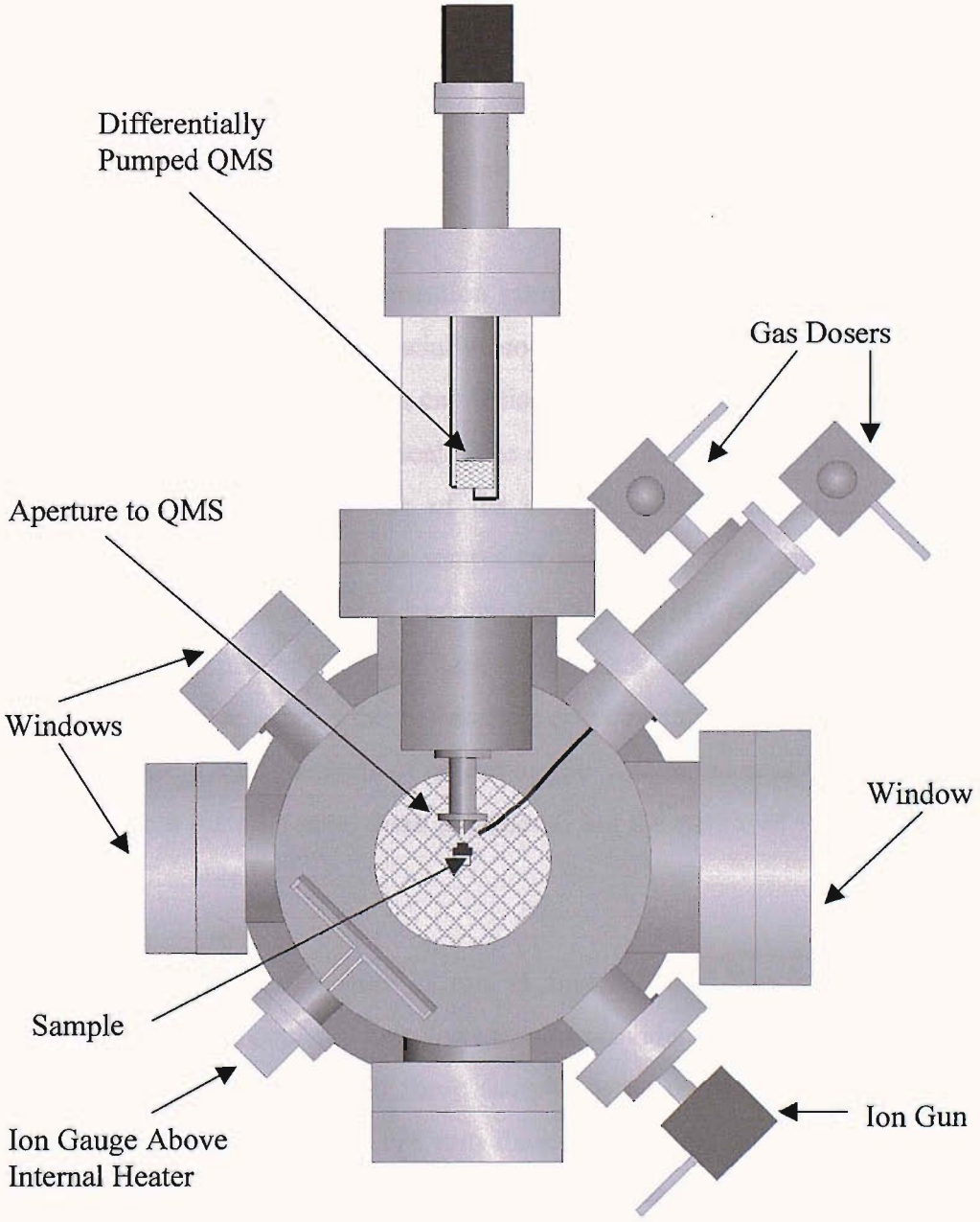

Figure 2.4 - Schematic of the permeation UHV system

2.2.1 Permeation Sample Holder and Gas Dosing

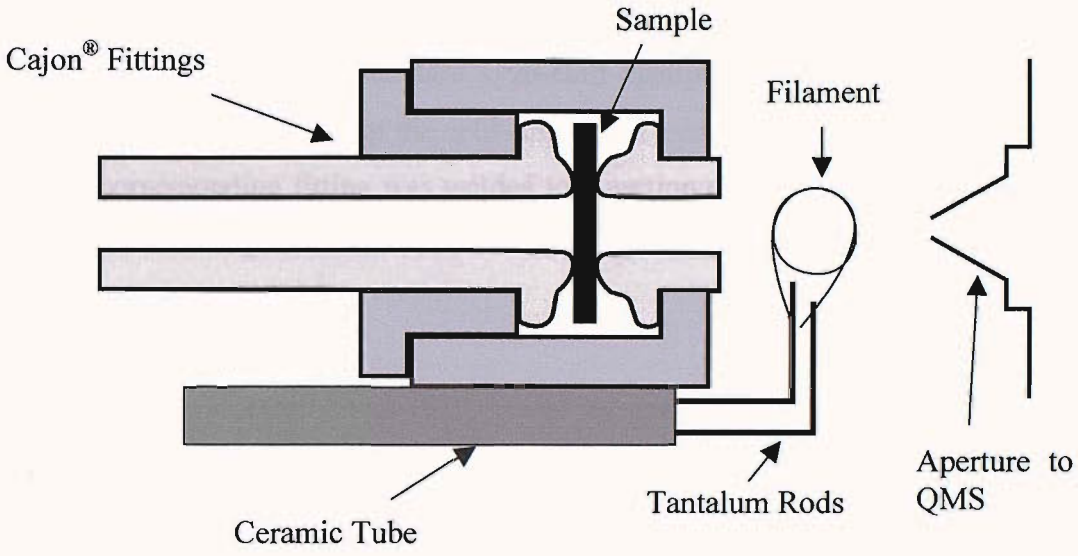

Figure 2.5 - Schematic of uranium sample holder used during the permeation experiments.

A schematic of the uranium permeation sample holder is shown in Figure 2.5. The holder was constructed from specially modified Cajon® fittings. The sample was clipped in place, not shown, and a cap fitting screwed down to provide the necessary pressure to maintain a leak tight seal. The centre of the cap had a 6 mm hole drilled though to expose the front face of the sample. This arrangement enabled the exposure of the back face of the sample to gas pressures ranging from 1 to 1000 mbar, while the front face was maintained in the UHV pressure region, ca. 10^{-9} mbar. The sample holder was positioned such that the sample holder was approximately 25 mm from the collimating aperture into the differentially pumped QMS chamber. Other methods of mounting the sample, such as welding or brazing the sample to a metallic tube, were considered but the nature of uranium meant that this was not feasible.

Both sets of samples used were 12 mm diameter disks. The first set were 1 mm thick polycrystalline depleted uranium samples provided by AWE plc. Aldermaston. Prior to delivery, both sides of these samples were polished with 1 μm diamond paste. The second set were 0.178 mm thick natural uranium samples provided by Goodfellow. The pressure of gas dosed onto the rear of the sample was controlled

by a series of leak valves and measured by a Baratron gauge with a 0 - 1000 mbar range. Between experiments the gas line was maintained at $3x10^{-4}$ mbar, by a dedicated Edwards E2M5 rotary pump. The gas dosing line extended through the base of the cold-finger on a standard xyzθ-shift manipulator that had been adapted for this purpose. At the base of the cold-finger was a conflat vacuum fitting (34 mm OD). A corresponding fitting was welded to a section of stainless steel tubing that was shaped to bring the front face of the sample holder into the centre of the manipulator's axis of rotation.

The sample was electron-beam (EB) heated by a negatively biased tungsten coil (0.25 mm thick). The coil was positioned approximately 5 mm from the front of the sample holder, any closer and there was a risk of the filament shorting to earth. The coil was spot-welded to two tantalum rods that were held in place by a ceramic tube, which was attached to the sample holder by a nickel strip that was wrapped around it and spot-welded to the holder. The temperature of the sample was measured by a K-type thermocouple spot-welded to the front of the sample holder. The sample was heated to the desired temperature over the course of several hours. Thus, allowing the temperature of the entire sample holder assembly to equilibrate before experiments were performed. After the completion of each experiment the heating was maintained for several hours to ensure that all of the permeating gas had been completely removed before the sample was allowed to cool, thus negating the possibility of any hydride formation.

2.2.2 Quadrupole Mass Spectrometer

A VG SXP 300 pulse counting QMS was housed in the smaller of the two UHV chambers on the permeation system. The differential pumping, reinsertion arm and collimating aperture meant that the background gas detected was kept to a minimum, whilst keeping the signal from the sample at a maximum. The QMS was used for residual gas analysis, leaks detection and permeation related experiments.

The QMS contains an ion source, mass filter and detector. The mass filter consists of four parallel conducting rods, to which combinations of DC and AC electric fields

are applied. Opposite rods are paired and each pair has an equal but opposite voltage applied. By switching the field back and forth only ions of a certain mass-to-charge ratio (m/z) have a stable trajectory and can pass to the detector.

2.2.3 Sample Preparation

The samples used within Chapter 5 were composed of two different metal membrane thicknesses. The thicker of the two membranes were 1 mm thick depleted uranium disks, denoted Set A. No sample preparation was performed on these samples, apart from the polishing that was carried out prior to delivery. Therefore, all of the samples were completely covered in a black air formed oxide overlayer that had formed during their months in storage.

The second group of membranes were 0.178 mm thick natural uranium disks. These samples were split into three Sets. The samples of Set B were left exposed to air and no cleaning or sample preparation was carried out upon them apart from that performed by the manufacturing before delivery. On insertion into the UHV system they were completely covered in an air formed oxide overlayer and were therefore comparable to Set A.

The remaining two 0.178 mm thick samples were intensively cleaned using a concentrated nitric acid solution. The solution was composed of 5 cm^3 nitric acid (80 % w/w) and 20 cm^3 ultra-pure water (18 Ω). Each sample was immersed in the solution for approximately 60 seconds before being removed with tweezers. It was then washed with water and patted dry with tissue. The colour of the samples was observed to change from black to grey as the level of surface contamination decreased. The first of these samples, Set C, was quickly transferred to a molecular beam epitaxy (MBE) UHV system, where a thin film of palladium was deposited onto one face of the sample at 373 K. During deposition, the sample was continuously mechanically rotated to ensure that a flat deposition surface was achieved. From comparison with previous MBE experiments, it was estimated that a film of approximately 200 nm had been deposited. Set C was then quickly transferred to the permeation UHV system, with the palladium surface acting as the

inlet surface for the purpose of the experiments. The second of the pre-cleaned samples, Set D, was directly mounted in the permeation UHV system.

Chapter 3: Experimental Techniques

3.1 Supersonic Molecular Beam Generation

Molecular beam experiments are used to investigate the adsorption and desorption dynamics of a gas interacting with a surface. The first beam experiments, developed by Gerlach and Stern [1], used an effusive stream of gas from an oven as the beam source. The beams generated had a wide Maxwellian energy distribution and a poor signal to noise ratio, thus in 1951 Kantrowitz and Grey [2] proposed that a supersonic jet could replace the conventional oven source. This had the main advantages that the molecular beams produced have narrower distributions, higher fluxes and better collimation.

The beam is generated when a gas at high pressure (P_n) expands through a nozzle into a low pressure region (P_b). The gas will expand isentropically along the central beam axis until the flow changes from continuum to free molecular, with virtually no molecular collisions. As the nozzle diameter (d) decreases the gas will accelerate from its stagnation state towards the sample due to the pressure difference. As this occurs, the temperature of the gas will decrease due to the enthalpy of the gas being converted into translational energy according to the first law of thermodynamics:

$$H_1 - H_0 = -\frac{1}{2}mv^2 \qquad \text{Equation 3.1}$$

where H_0 is the stagnation enthalpy per unit mass in the source, m and v are the mass and velocity of the gas molecules respectively. The result is a beam of gas molecules that are increasing in velocity but decreasing in temperature. The distribution of velocities can be characterised by a Maxwellian distribution of low gas temperature and is consequently very narrow. The effect of temperature on the Maxwellian distribution and the Mach number (M) can be seen in Figure 3.1. The Mach number is defined as the ratio of the molecule speed to the speed of sound.

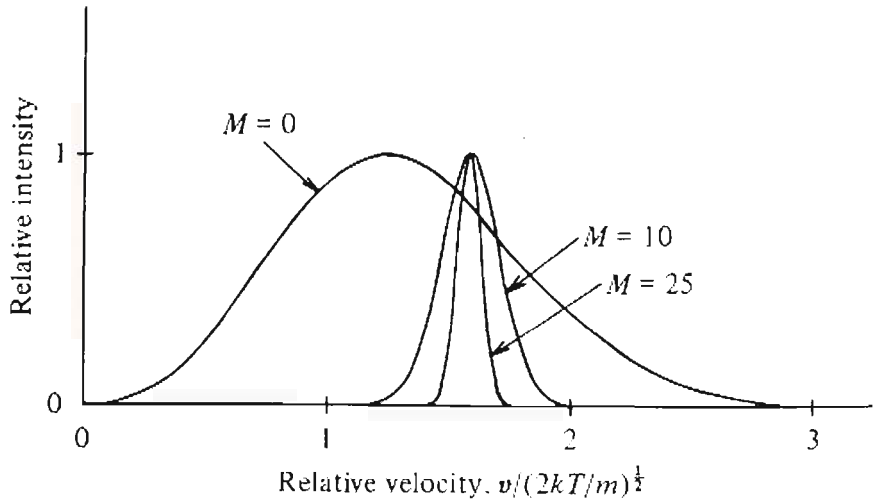

Figure 3.1 – Normalised supersonic nozzle and effusive beam velocity distributions.

Figure 3.2 shows the supersonic beam expansion [3]. In the zone of silence the gas molecules are travelling at supersonic speeds (M>>1). Within this region there is adiabatic molecular flow, which is independent of the boundary conditions. However, the speed of the gas cannot continue to increase indefinitely. At the boundary with the background pressure the gas will over-expand and become compressed by a series of shock waves. Shock waves are regions, which contain large temperature, pressure, density and velocity gradients. They enable the direction of a supersonic flow to be changed and, if necessary, the Mach number can also be reduced in order meet the appropriate boundary conditions. At the Mach disk the flow has slowed from supersonic (M>1) to subsonic speeds (M<1).

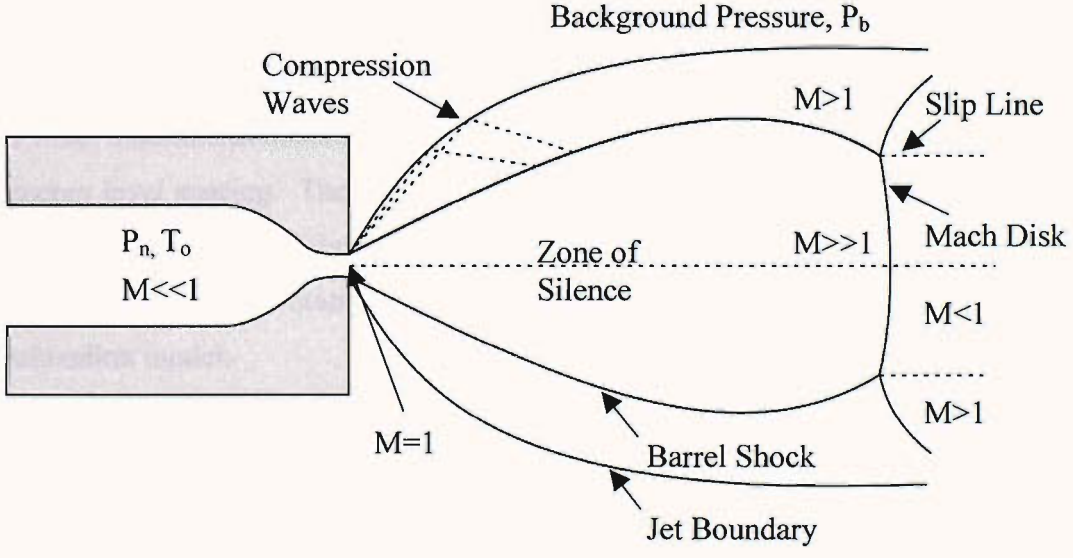

Figure 3.2 - Supersonic beam expansion

The position of the Mach disk (x_M) relative to the nozzle is determined by:

$$x_M = \frac{2}{3} d \left(\frac{P_n}{P_b} \right)^{\frac{1}{2}}$$ Equation 3.2

In order to sustain the supersonic molecular flow over large distances, a skimmer is placed within the zone of silence at ~100d from the nozzle to ensure that the centre of the beam is extracted before the Mach disk is reached. The skimmer extracts the central flow while defecting away the majority of the gas and is shaped to avoid the creation of shock waves in front of, or within, the skimmer itself. The selected gas flow will pass through the second stage chamber before passing through a further collimating aperture into the main chamber. Within the main chamber, the mean free path is long and the majority of the beam will continue without many significant collisions towards the sample. The pressure rise observed in the main chamber is comprised of two components. The effusive component is due to the diffusion of molecules from the beam, while the beam component is due to the proportion of molecules that collide with the surface.

Vibrational and rotational relaxations can occur as a result of the falling gas temperature as the beam expands. The degree of relaxation that occurs is dependant upon the number of collisions between molecules during expansion and the energy difference between the vibrational and rotational states. The typical number of collisions experienced by a molecule during expansion is between 100 and 1000, which is sufficient to cool its rotational states. The vibrational relaxation period for a small diatomic molecule, such as hydrogen, is about 10^4 collisions due to the large energy level spacing. Therefore, the amount of vibrational cooling experienced will be small. Rotational relaxation is generally much faster due to the smaller energy level spacing. The rotational relaxation period can be evaluated using the linear relaxation model:

$$\frac{dT_r}{dt} = \frac{(T - T_r)}{\tau}$$ Equation 3.3

where τ is the ratio of the number of required collisions (Z) to the collision frequency (ν).

The terminal velocity of the gas molecules impinging on the sample surface can be estimated by relating the change in enthalpy (dH) to the molar heat capacity at constant pressure (C_p):

$$dH = C_p dT \qquad \text{Equation 3.4}$$

where dT is the temperature difference before and after expansion. Combining Equations 3.1 and 3.4 gives:

$$-\frac{1}{2}mv^2 = C_p dT \qquad \text{Equation 3.5}$$

In most cases $T_0 >> T$ and C_p is considered to be independent of T. Using this, Equation 3.5 becomes:

$$v = \left(\frac{2}{m} C_p T_o\right)^{\frac{1}{2}} \qquad \text{Equation 3.6}$$

For an ideal gas:

$$C_p = \left(\frac{\gamma}{\gamma - 1}\right) R \qquad \text{Equation 3.7}$$

where γ is the ratio C_p/C_v and C_v is the molar heat capacity at constant volume. The terminal velocity (v_∞) of a gas after expansion can be expressed as:

$$v_\infty = \left(2\left(\frac{RT_0}{m}\right)\left(\frac{\gamma}{\gamma - 1}\right)\right)^{\frac{1}{2}} \qquad \text{Equation 3.8}$$

If the gas is a mixture of x_i components then the terminal velocity of the beam becomes:

$$v_\infty = \left(2(RT_0) \frac{\sum x_i \left(\frac{\gamma}{\gamma - 1} \right)}{\sum x_i m_i} \right)^{\frac{1}{2}} \qquad \text{Equation 3.9}$$

This velocity will only be observed if the number of collisions at the nozzle is large enough to equilibrate the velocities of both gases. This approximation is found to be reasonable for small gas molecules that constitute less than 1% of a seeded beam. Deviation from the ideal gas behaviour occurs when there is a significant mass difference. The lighter molecules will have a high velocity perpendicular to the beam axis, leading to increased divergence.

Within a seeded beam the seed gas molecules are used to control the velocity of the reactant gas. In many cases, a monoatomic ideal gas, such as He or Ar, is used as the seeding gas. Thus, the kinetic energy of the seed gas in this beam is:

$$E_{i(seed)} = \frac{1}{2} m_{(seed)} v_{(seed)}^2 \qquad \text{Equation 3.10}$$

The molar enthalpy of an ideal gas is defined as:

$$H = U + PV \qquad \text{Equation 3.11}$$

A monoatomic gas has no vibrational or rotational degrees of freedom. Therefore, the internal energy (U) is equal to the translational energy, which has three degrees of freedom. Using this and the ideal gas law, Equation 3.11 becomes:

$$H = \frac{3}{2} k_B T_n + k_B T_n = \frac{5}{2} k_B T_n \qquad \text{Equation 3.12}$$

In the present case the enthalpy is transferred to the kinetic energy of the gas, $H = E_i$. Therefore,

$$\frac{5}{2}k_B T_n = \frac{1}{2}m_{(seed)}v^2_{(seed)} \qquad \text{Equation 3.13}$$

$$v^2_{(seed)} = \frac{5k_B T_n}{m_{(seed)}} \qquad \text{Equation 3.14}$$

At low seeding ratios, i.e. less than 5%, the velocity of the seed gas can be assumed to be approximately the velocity of the reactant gas. From this assumption the kinetic energy of the reactant gas within the beam can be calculated.

$$E_{i(react)} = \frac{1}{2}m_{(react)}v^2_{(seed)} \qquad \text{Equation 3.15}$$

Hence,

$$E_{i(react)} = \frac{5}{2}\frac{m_{(react)}}{m_{(seed)}}k_b T_n \qquad \text{Equation 3.16}$$

This formula was used throughout Chapter 4 to calculate the beam energies.

3.2 King and Wells Method

3.2.1 Sticking Probability Measurements

The absolute sticking probability can be calculated using the King and Wells method [4]. This is a relatively fast, simple reflection-detection technique, which samples only a small area of the surface, in the order of a few millimetres. However, it is limited to measurement of sticking probabilities higher than 5%.

At the beginning of all these experiments (t_0) a beam was generated, as described in Section 3.1. An example of the QMS spectra observed is shown in Figure 3.3 [5]. The path of the beam was blocked by closure of the aperture, between the second stage and the main chamber, and the flag. The base pressure (P_0) in the main chamber at this time, as recorded by the QMS, can be described by:

$$P_0 = c(F_0 - S_P P_0) \qquad \text{Equation 3.17}$$

where c is a constant specific to the chamber, F_0 is the flux due to the background and S_P is the pumping speed of the main chamber.

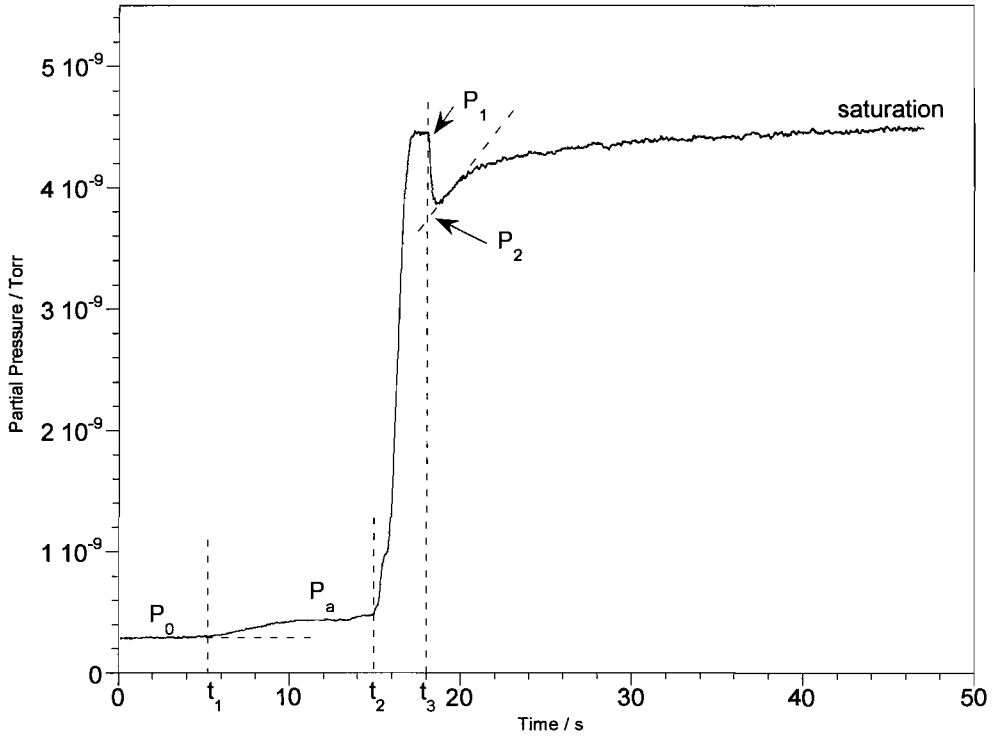

Figure 3.3 – Typical QMS trace taken during a King and Wells experiment.

At time t_1 the aperture was opened and the pressure in the main chamber was seen to increase slightly (P_a). The nozzle was then moved into position, in line with the skimmer (t_2) and the pressure increased in the main chamber to P_1. The flag was then opened at time t_3 and the pressure was seen to decrease to P_2. The initial sudden decrease in pressure is due to a fraction of molecules adsorbing onto the

surface and is equal to initial sticking probability (S_0). Pressures P_1 and P_2 can be described by the following equations:

$$P_1 = c(F_0 + F_b - S_P P_1) \qquad \text{Equation 3.18}$$

$$P_2 = c(F_0 + F_b(1 - S_0) - S_P P_2) \qquad \text{Equation 3.19}$$

where F_b is the additional flux due to the beam. The pressure changes (P_1-P_2) and (P_1-P_0) can be calculated from Equations 3.18 and 3.19. A ratio of these changes can be used to directly calculate S_0:

$$S_0 = \frac{(P_1 - P_2)}{(P_1 - P_a)} \qquad \text{Equation 3.20}$$

This relationship is based on the assumption that the pumping rate and the parameter c of the chamber are constant over the pressure range change from P_0 to P_1. For these experiments the pressure rise was less than 10^{-8} mbar and therefore this assumption is valid. It is also assumed that all the beam molecules that enter the main chamber will impinge on the surface, which is less reasonable because a fraction of these molecules (F_d) will be diffusely scattered by the aperture adding to the background intensity. For this system F_d has been estimated to be ca. 21% by Butler [6] and from this Equation 3.20 becomes:

$$S_0 = \frac{(P_1 - P_2)}{(P_1 - P_0)(1 - F_d)} \qquad \text{Equation 3.21}$$

The sticking probability varies as a function of coverage and will become zero upon saturation. Substitution of the pressure at any given time (P_t) into Equation 3.21 will yield the instantaneous sticking probability. The coverage (θ) can also be calculated at any given time using a ratio of the area beneath the uptake curve at time (t) and the saturation area and multiplying by θ_{sat}, the known saturation coverage for the system, see Equation 3.22.

$$\theta = \frac{\int_{t_1}^{t}(P_1 - P_t)}{\int_{t_1}^{\infty}(P_1 - P_t)} * \theta_{sat} \qquad \text{Equation 3.22}$$

3.3 X-Ray Photoelectron Spectroscopy

X-ray photoelectron spectroscopy (XPS) is an extremely useful technique not only for elemental analysis, but also for determining the composition of a surface quantitatively [7; 8]. Electromagnetic radiation from the X-ray region (100 – 2000 eV) is used to eject electrons from the core and valence levels of an atom, see Figure 3.4. A monochromatic beam of photons, of energy hν, impinges on a surface and is absorbed by electrons with a binding energy (E_{BE}) with respect to the Fermi level. The emitted electrons must also overcome the work function (ϕ) of the solid, which is the minimum energy necessary to remove an electron from the highest occupied level in the solid to the vacuum level. The electrons are then ejected from the surface with a kinetic energy (E_{KE}).

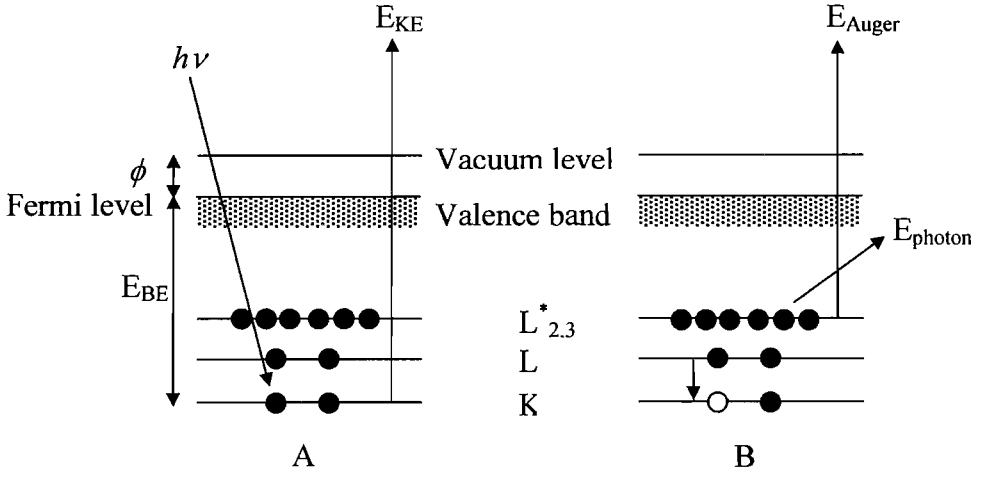

Figure 3.4 - Energy level diagram showing, A - an electron ejection by X-ray radiation and B - the secondary processes that may occur.

If it is assumed that all the electrons in the system are in the same state before and after the photoionisation event. Then it is said to obey Koopman's theorem and $(E_{BE} + \phi)$ is Koopman's energy. If this is the case then Equation 3.23 gives the kinetic energy of the ejected electron:

$$E_{KE} = h\nu - E_{BE} - \phi \qquad \text{Equation 3.23}$$

However, this is not a realistic view of the photoionisation process. The system experiences relaxation shifts, whereby the hole created by photoionisation is partially screened by electrons of higher states shifting to lower levels. This relaxation makes more energy available to the outgoing electron and is an intra-atomic relaxation shift (E_a). Inter-atomic relaxation shifts (E_r) also have to taken into account, whereby the mobile valence electrons of a free atom on, or in, a solid can screen the hole created. The intra- and inter-atomic relaxation shifts are referred to as final state effects. Hence, Equation 3.23 can be rewritten to give:

$$E_{KE} = h\nu - E_{BE} - \phi + E_a + E_r \qquad \text{Equation 3.24}$$

The photoemission process is further complicated by shake-up and shake-off effects, which lead to a reduction of the energy of the emitted photoelectron and structure on the low kinetic energy side of the photoelectron peak. Photoelectrons that have lost energy through promotion of valence electrons from occupied levels to unoccupied levels result in shake-up peaks. Photoelectrons that are excited from the valence level into the continuum of unbound states above the vacuum level are associated with shake-off peaks.

Initial state, or chemical shift, effects can also affect the energy of a photoelectron. If an atom is charged then the binding energy of the electrons in that atom is different to that in the uncharged atom. The charge potential model can describe the difference in energies:

$$E_{Bi} = E_i^0 + k_q + \sum_{i \neq j} \frac{q_i}{r_{ij}} \qquad \text{Equation 3.25}$$

where, E_{Bi} = binding energy of a given core level of atom i

E_i^0 = energy reference

q_i = valence charge of atom i

k_q = constant

$\sum_{r \neq j} \frac{q_i}{r_{ij}}$ = sum of potentials from point charges on surrounding atoms, j, at atom i

The chemical shift effect can be related to differences in the oxidation state and molecular environment of an atom. Hence, an increase in the oxidation state of an atom will lead to an increase in the binding energy due to a decrease in valence electron density. Particle size will also affect the binding energy of a species. Isolated atoms will have a higher binding energy than large clusters. The shifts observed in experiments will be a combination of initial and final state effects, which may counter each other.

Figure 3.4, also shows the secondary processes that may occur during X-ray radiation. An electron from a level with lower binding energy can relax to fill the hole created by photoionisation. The energy released can either be lost in the form of a photon (E_{photon}) or with the ejection of another electron from the atom, known as the Auger electron (E_{Auger}). These electrons will appear in the XPS spectra. However, the Auger electrons are not affected by changes in the initial X-ray excitation energy.

3.3.1 Coverage Analysis

XPS spectra peak areas are directly proportional to the amount of material present within the sampling area, typically of the order of $5x10^{-2}$ cm^2. However, the detected volume is limited to a region near the surface due to the inelastic mean free path (IMFP) of the photoelectrons [9]. The IMFP is only weakly dependent on the

material but it is strongly dependent on the electron kinetic energy, described by the "universal curve" [7]. The data is fitted by the curve:

$$\lambda_m = \frac{538}{E_{KE}^2} + 0.41(aE_{KE})^{1/2} \qquad \text{Equation 3.26}$$

where, the IMFP (λ_m) is in monolayers, E_{KE} is the electron kinetic energy and a is the monolayers thickness, given by:

$$a^3 = \frac{A}{\rho n N} x10^{24} \qquad \text{Equation 3.27}$$

where, A is the atomic, or molecular, weight, n is the number of atoms in the molecule, N is Avogadro's number and ρ is the bulk density, in kgm^{-3}. The conversion of the IMFP from monolayers to nanometres is:

$$\lambda_n = a\lambda_m \qquad \text{Equation 3.28}$$

The detected sampling depth (d) is dependent on the orientation of the sample to the detector:

$$d = \lambda_n \cos\theta \qquad \text{Equation 3.29}$$

where, θ is the angle of the detector from the surface normal. In the molecular beam UHV system θ is approximately ~54°. Therefore, it is possible to calculate the effective sampling depth of the XPS system for the U $4f_{7/2}$ electrons of uranium and uranium dioxide, using Equation 3.29. Uranium has λ = 1.97 nm and a U-U bond length of 0.28 nm, this gives an effective sampling depth of approximately 12 atomic layers. Uranium dioxide has λ = 1.96 nm, a U-U bond length of 0.27 nm and an effective sampling depth of approximately 6 molecular layers

The coverage of a thin overlayer of absorbate A on substrate B can be calculated from the ratio of respective XPS signal intensities. The signal peak intensity of a substrate with monolayers coverage (ϕ_A) of an absorbate is given by:

$$I_B = I_B^{\infty}\left(1-\phi_A+\phi_A \exp\left[-a_A/\lambda_A(E_B)\cos\theta\right]\right) \qquad \text{Equation 3.30}$$

where, I_B^{∞} is either the signal from a clean substrate or the relative sensitivity factor. The overlayer signal is given by:

$$I_A = \phi_A I_A^{\infty}\left(1-\exp\left[-a_A/\lambda_A(E_A)\cos\theta\right]\right) \qquad \text{Equation 3.31}$$

The ratio of these equations is:

$$\frac{I_A I_B^{\infty}}{I_B I_A^{\infty}} = \frac{\phi_A\left(1-\exp\left[-a_A/\lambda_A(E_A)\cos\theta\right]\right)}{1-\phi_A\left(1-\exp\left[-a_A/\lambda_A(E_B)\cos\theta\right]\right)} \qquad \text{Equation 3.32}$$

If $a_A << \lambda_A$ and the coverage of A is low then:

$$\phi_A = Q\frac{I_A}{I_A^{\infty}}\frac{I_B^{\infty}}{I_B} \qquad \text{Equation 3.33}$$

where,

$$Q = \frac{\lambda_A \cos\theta}{a_A} = 0.41(a_A E_A)^{1/2}\cos\theta \qquad \text{Equation 3.34}$$

3.4 Temperature Programmed Desorption

When a species adsorbs reversibly onto a surface it bonds with a specific amount of energy. Temperature programmed desorption (TPD) allows the adsorbed species, the surface coverage and the binding energies to be investigated provided the adsorbed species does not chemically alter during desorption. This technique relies upon there being an exponential relationship between the surface temperature (T_S) and the residence time (τ) of the adsorbed species:

$$\tau = \tau_0 \exp\left(-\frac{E_{des}}{RT_s}\right) \qquad \text{Equation 3.35}$$

where τ_0 is correlated with the surface atom vibration time, in the order of 10^{-12} seconds and E_{des} is the activation energy of desorption.

During a typical TPD experiment the sample is resistively heated to break the surface-adsorbate bonds. This allows the adsorbed species to desorb and become detected by a mass spectrometer. If the adsorbate is not resupplied then the surface concentration will decrease, until the sample is clean. Figure 3.5, shows the pressure-time trace of a TPD experiment in which the pumping speed of the system is greater than that of the desorption rate. Therefore, the pressure within the chamber is proportional to the desorption rate, with the maximum pressure corresponding to the maximum rate of desorption.

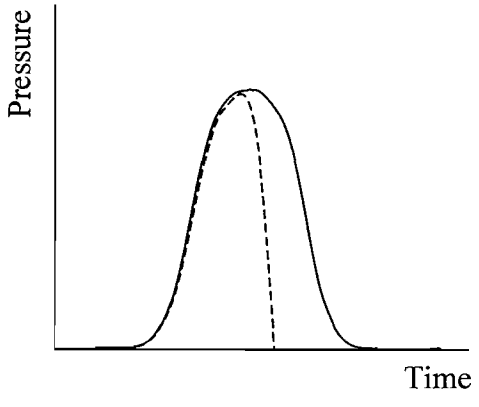

Figure 3.5 - Pressure-Time trace during a TPD experiment showing first (-) and second (---) order desorption

Assuming a linear heating rate, the surface temperature is:

$$T_s = T_0 + \left(\frac{dT_s}{dt}\right)t \qquad \text{Equation 3.36}$$

where T_0 is the initial surface temperature and dT_s/dt is the heating rate. Combining Equation 3.36 with an Arrhenius type equation gives:

$$R_{des} = -\frac{d\theta}{dT} = n\theta^{n-1}\frac{\nu}{A}\exp\left(-\frac{E_{des}}{RT_s}\right) \qquad \text{Equation 3.37}$$

where $A = dT_s/dt$, the heating rate, θ is the surface coverage and n is the kinetic order of the reaction. The frequency factor (v) is of the order of the bond being broken in the reaction coordinate, taken to be approximately $10^{-13}s^{-1}$ in all calculation in this thesis. At the maximum desorption rate $T = T_p$ and $d^2\theta/dT^2 = 0$. Differentiating Equation 3.37 with respect to T gives:

$$-\frac{d^2\theta}{dT^2} = \frac{\nu}{A}\left(n\theta^{n-1}\frac{d\theta}{dT}\exp\left(-\frac{E_{des}}{RT}\right) + \frac{\theta E_{des}}{RT^2}\exp\left(-\frac{E_{des}}{RT}\right)\right) = 0 \qquad \text{Equation 3.38}$$

Rearranging Equation 3.38 gives:

$$n\theta^{n-1}\frac{d\theta}{dT} = -\frac{\theta^n E_{des}}{RT^2} \qquad \text{Equation 3.39}$$

Substituting in Equation 3.37 allows E_{des} to be iteratively calculated from:

$$\frac{E_{des}}{RT_p^2} = n\theta^{n-1}\frac{\nu}{A}\exp\left(-\frac{E_{des}}{RT_p}\right) \qquad \text{Equation 3.40}$$

Therefore, for first and second order desorption processes the associated Equation are 3.41 and 3.42 respectively.

$$\frac{E_{des}}{RT_p^2} = \frac{\nu}{A}\exp\left(-\frac{E_{des}}{RT_p}\right) \qquad \text{Equation 3.41}$$

$$\frac{E_{des}}{RT_p^2} = \frac{2\nu\theta}{A}\exp\left(-\frac{E_{des}}{RT_p}\right) \qquad \text{Equation 3.42}$$

It can be seen that first-order desorption is independent of coverage. Therefore, the maximum peak position will not change with coverage. In contrast, second-order desorption processes are coverage sensitive. If it assumed that E_{des} and ν are independent of coverage then the peak position will be expected to shift to lower temperatures as the coverage increases. However, there are many other factors that have to be considered. The presence of pre-cursor states, a coverage dependent E_{des} or thermal conversion between adsorbed species all lead to complications in TPD analysis. There are also experimental factors that have to be considered such as the uniformity of the sample heating and the sensitivity of the mass spectrometer.

3.5 Permeation of Gas through a Membrane

The permeation of a gas through a metal membrane involves several steps in series, moving from the high pressure side to the low pressure side:

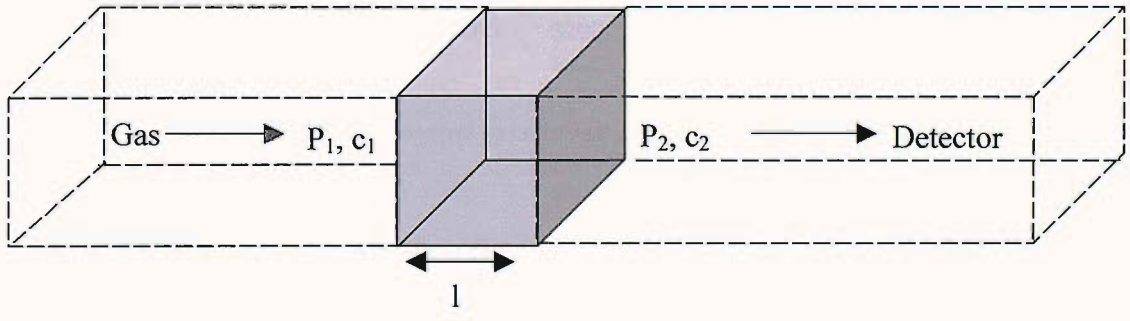

Figure 3.6 – Permeation of a gas through a metal membrane.

1 - Adsorption of the gas onto the metal entrance surface.

2 - Dissolution of the adsorbed gas into the bulk.

3 - Diffusion of the gas through the bulk.

4 - Transition of the gas from the bulk to the exit surface.

5 - Desorption of the gas.

One or more of the above steps may limit the overall rate of permeation. In many cases step 3 is rate limiting, therefore the permeation of a gas through a membrane is commonly used to determine the diffusion coefficient of a gas in the membrane material.

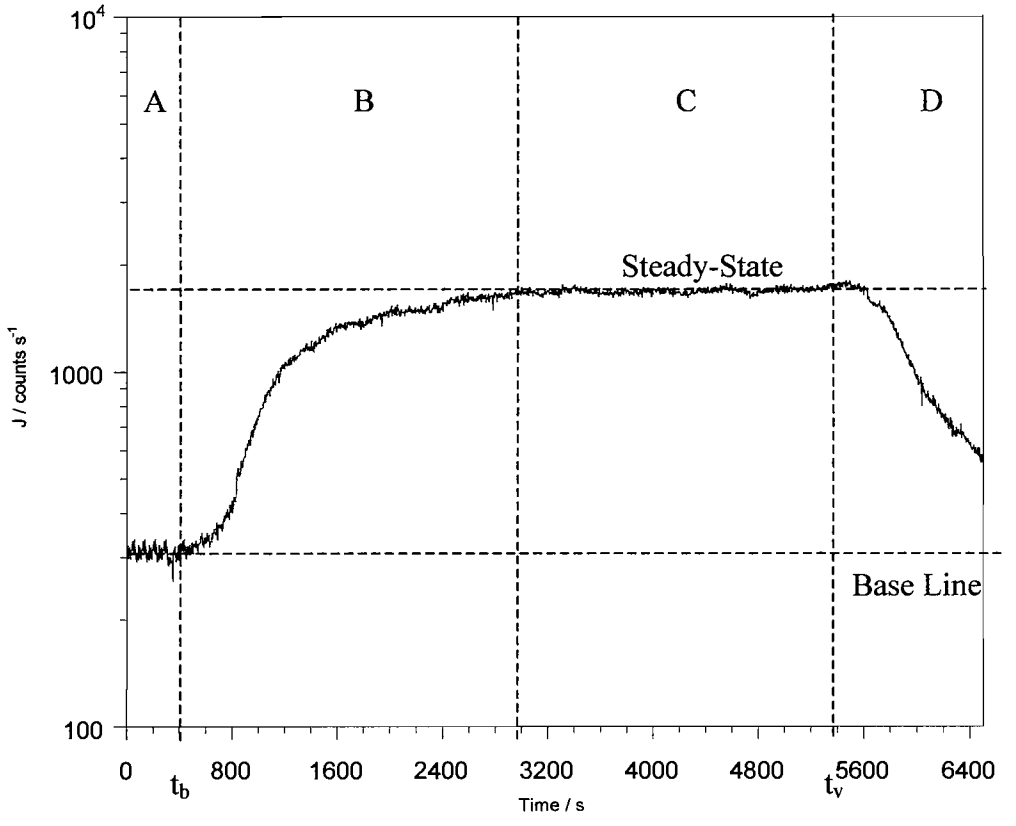

Figure 3.7 - Pressure-time plot of detected permeation gas, for a continuously pumped system.

One possible method for calculating the diffusion coefficient experimentally is the Time Lag method [10]. Typically, the membrane is mounted between two chambers both of which are initially evacuated. The inlet chamber is isolated from the pumping system prior to the permeating gas being introduced. The amount of gas used (P_1, torr) is sufficiently high that the pressure drop due to permeation is negligible, therefore the concentration at the entry surface (c_1, $cm^3_{gas}cm^{-3}_{metal}$), is assumed to be constant. The pressure in the outlet chamber (P_2) is kept small and

the exit surface concentration (c_2) is considered to be zero. Also, the concentration within the membrane is so small in comparison to c_1 that it is considered to be zero.

A pressure-time curve of permeating gas detected in the outlet chamber is shown in Figure 3.7. Note that the outlet chamber is constantly being pumped. At t=0 the desired pressure of gas is placed behind the sample. There follows a length of time in which no gas is detected, Region A. After the breakthrough time (t_b) there is a non-linear pressure increase, Region B, until a steady-state is reached and the gas diffuses at a constant rate, Region C. At time t_v, the inlet chamber is evacuated and after a short delay the pressure begins to decrease back to the original background level, Region D.

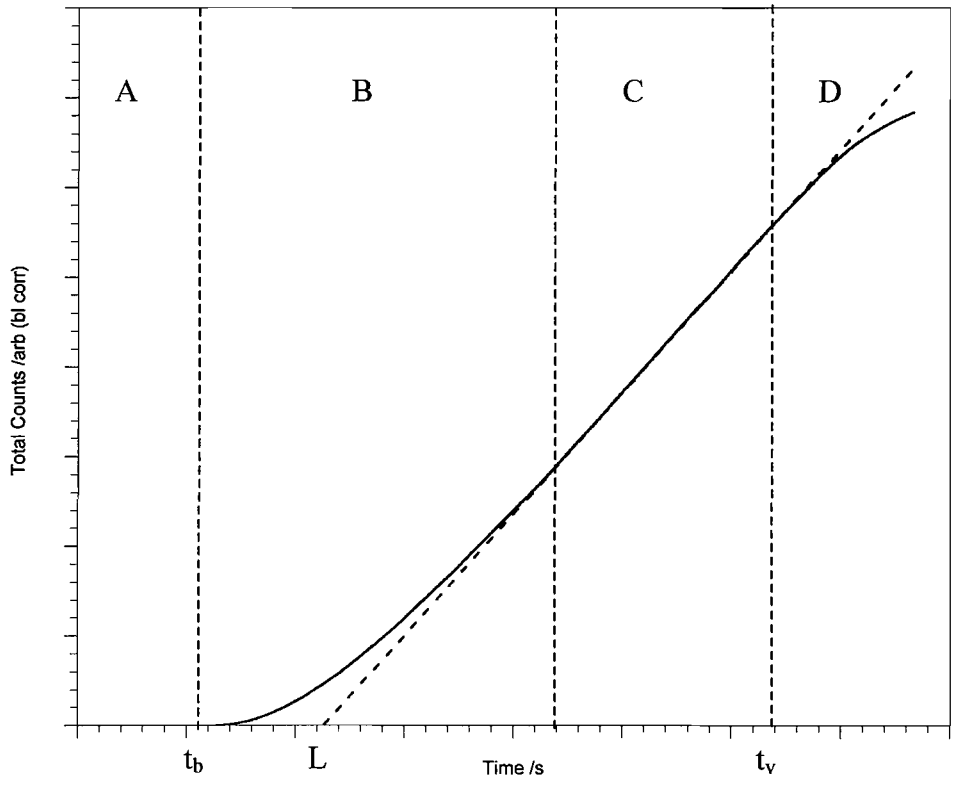

Figure 3.8 – Integral of the pressure-time plot shown in Figure 3.7, base line corrected (bl corr).

An integral of the pressure-time curve is shown in Figure 3.8, regions A, B, C and D are explained above. The curve can be described by integrating Fick's second law,

Equation 1.14, with appropriate boundary conditions [11-13]. As $t \rightarrow \infty$ the steady-state region (C) approaches the line:

$$Q_t = \frac{Dc_1}{l}\left(t - \frac{l^2}{6D}\right) \qquad \text{Equation 3.43}$$

where Q_t is the total amount of gas permeating through the membrane in time t (cm^3), l is the thickness of the membrane (cm) and D is the diffusion coefficient (cm^2s^{-1}). This has an intercept of L with the time axis given by:

$$L = \frac{l^2}{6D} \qquad \text{Equation 3.44}$$

Hence, the diffusion coefficient can be calculated directly from the permeation measurements. The flux of gas in the steady-state can be expressed by the following equation [14]:

$$J = \frac{AD}{l}(c_1 - c_2) \qquad \text{Equation 3.45}$$

where A is the area of the membrane (cm^2). If it is assumed that the concentration of gas at the metal-gas interface is constant then according to Sievert's law the equilibrium membrane concentration is proportional to the square root of the external vapour pressure:

$$c = SP^{\frac{1}{2}} \qquad \text{Equation 3.46}$$

where S is the solubility ($cm^3_{gas}cm^{-3}_{metal}atm^{-1/2}$). If the surface reactions were rate limiting and the diffusion process was fast then the equilibrium concentration would be directly proportional to the inlet pressure. Using Equation 3.46 the flux becomes:

$$J = \frac{AD}{l}S\left(P_1^{\frac{1}{2}} - P_2^{\frac{1}{2}}\right) \qquad \text{Equation 3.47}$$

Assuming that $P_1 >> P_2$, then Equation 3.47 can be rearranged to:

$$DS = \frac{Jl}{AP^{\frac{1}{2}}} = J_0 \qquad \text{Equation 3.48}$$

where J_0 is the specific permeability ($cm^3_{gas}s^{-1}cm^{-1}atm^{-1/2}$). Hence, measurements of the flux at steady-state and the diffusion coefficient, calculated by the Time Lag method, will yield the solubility of the gas in the material corresponding to the temperature of the membrane and the pressure of gas at the inlet surface. Both the diffusion coefficient and the solubility depend on the membrane temperature. Hence, an Arrhenius type relationship can be applied:

$$D = D_0 \exp\left(-\frac{E_D}{RT}\right) \qquad \text{Equation 3.49}$$

$$S = S_0 \exp\left(-\frac{E_S}{RT}\right) \qquad \text{Equation 3.50}$$

where E_D and E_S are the activation energies and D_0 and S_0 are the pre-exponential factors. Thus, the specific permeability will also have Arrhenius type temperature dependence:

$$J_0 = J_{0,0} \exp\left(-\frac{E_{J_0}}{RT}\right) \qquad \text{Equation 3.51}$$

where,

$$J_{0,0} = D_0 S_0 \qquad \text{Equation 3.52}$$

and,

$$E_{J_0} = E_D + E_S \qquad \text{Equation 3.53}$$

In all cases R is the gas constant and T is the absolute membrane temperature.

3.6 References

[1] Gerlach, W., O. Stern, Z. Phys. 8 (1921) 110.

[2] Kantrowitz, A., J. Grey, Rev. Sci. Instr. 22 (1951) 328.

[3] Miller, D.R., Atom.Mol.Beam.Meth. 1 (1985) 14-53.

[4] King, D.A., M.G. Wells, Surf. Sci. 29 (1972) 454-482.

[5] Mormiche, C., PhD. Thesis, University of Southampton, Southampton, (2002)

[6] Butler, D.A., PhD. Thesis, University of Southampton, Southampton, (1994)

[7] Seah, M.P., W.A. Dench, Surf. Int. Anal. 1 (1979) 2.

[8] Seah, M.P., Surf. Interface Anal. 2 (1980) 222.

[9] Briggs, D., M. Seah, Practical Surface Analysis by Auger and X-ray Photoelectron Spectroscopy, Chichester, John Wiley & Sons Ltd., 1983.

[10] Barrer, R.M., Trans. Faraday Soc. 35 (1939) 628-643.

[11] Doremus, R.H., Diffusion of Reactive Molecules in Solids and Melts, New York, Wiley, 2002.

[12] Crank, J., The Mathematics of Diffusion, Oxford, Oxford University Press, 1975.

[13] Jost, W., Diffusion in Solids, Liquids, Gases, New York, Academic Press, 1952.

[14] Davis, W.D., GEC, Knolls Atomic Power Laboratory, New York, KAPL-1548, (1956)

Chapter 4: Adsorption Of Hydrogen On Polycrystalline Uranium Surfaces With Modified Uranium Oxide Overlayers

4.1 Introduction

Uranium is the last, and heaviest, of the naturally forming elements in the periodic table. Martin Kalproth [1] believed that he had isolated the metal from a specimen of pitchblende in 1789. However, in 1841 Eugene-Melchoir Peligot showed that the black metallic-looking substance was in fact the oxide, UO_2, and he then went on to isolate the metal by reducing the anhydrous chloride with potassium [2; 3]. Henri Becquerel [4] discovered that uranium undergoes radioactive decay in 1896, by exposing photographic paper to a number of uranium salts.

It was not until the discovery of nuclear fission by Hahn and Strassman in 1938 that the true importance of uranium was established. Nuclear fission is the process whereby ^{235}U atoms are bombarded with neutrons, which cause the atom to split into two fissible products, with the release of two or three additional neutrons and a large amount of energy in the form of heat. If the extra neutrons released lead to the splitting of other ^{235}U atoms then a chain reaction can be achieved. Natural uranium is composed of 99.27% ^{238}U, 0.72% ^{235}U and 0.0055% ^{234}U with a total of 16 isotopes possible, all of which are radioactive [5]. The radioactive nature of uranium means that it also has numerous uses for medical, industrial and defence applications.

The discovery of fission has lead to many studies being carried out to understand the solid-state properties of uranium [6]. The initial focus of these studies was to increase the understanding of uranium and ultimately to increase its efficiency as a fuel. Many of these early studies concentrated on the high temperature properties that were of importance to the performance of uranium as a nuclear fuel. However, uranium is known to have three phases. The high temperature γ-phase is stable from

1045 K to 1405 K, the intermediate β-phase is stable from 935 K to 1045 K and the low temperature phase, the phase of interest in this investigation, is the α-phase.

The properties of α-uranium have been intensively studied and there exists an abundance of data concerning reaction kinetics. In spite of this, there is relatively little data on the dynamics of uranium reactions. Early studies by Winer *et al* [7] used TPD, XPS and secondary ion mass spectrometry (SIMS) to examine the interaction of water with both clean and oxidised uranium surfaces. The O 1s XPS spectra for both oxygen and water adsorption exhibited small satellite peaks, approximately 2 eV higher in binding energy than the main characteristic peaks. These were attributed to strongly chemisorbed O_2^- or O^- and strongly chemisorbed OH^- species respectively. TPD measurements of water on clean and pre-oxidised uranium, dosed at 100 K, showed a single desorption peak at 200 K. The peak was attributed to weakly bound water molecules that could adsorb on top of both clean and oxidised uranium. These results are contrary to the latter TPD work of Danon *et al* [8]. In the temperature range 293 - 923 K, they observed four water desorption features from heavily oxidised samples. A broad large peak around 573 K was assigned to weakly bound water molecules desorbing. On its high temperature side this peak exhibited a shoulder that was attributed to either more strongly bound water or the decomposition of hydroxyl clusters. A second less intense hydroxyl decomposition peak was observed at approximately 560 K. A prominent peak at 623 K was only observed on samples that contained high levels of carbo-oxy species, due to contamination from CO_2 in air during oxidation. The presence of these contaminants was thought to lead to the formation of H_2O-CO_x surface groups. This was supported by CO and CO_2 TPD spectra, which both had a single desorption feature at 623 K. Hydrogen TPD spectra showed three distinct features. A low temperature peak, centred around 523 K, was related to the surface decomposition of water to form uranium oxide and adsorbed hydrogen atoms. The intense peak at 650 K was shown to be due to decomposition of surface hydride species formed at the oxide-metal interface. A broad feature around 773 K was attributed to desorption of hydrogen impurities from the bulk.

Swissa *et al* [9] used direct recoil spectroscopy (DRS), Auger electron spectroscopy (AES) and XPS to study the adsorption of hydrogen and oxygen on clean and oxidised polycrystalline U-0.1 wt.% Cr alloy surfaces. At room temperature, the sticking probability of hydrogen on sputter-cleaned samples was calculated to be 0.1 and the chemisorption was said to progress via a cluster mechanism. The sticking probability decreased to 0.06 when oxygen was pre-dosed onto the surface and in this case the adsorption was postulated to follow a two-site Langmuir chemisorption model. Pre-dosing of hydrogen was shown to have a significant effect on the oxygen chemisorption process. Instead of forming an oxide overlayer, as is the case of a sputter-cleaned surface, the oxygen formed a protective layer of chemisorbed oxygen atoms. Investigations into the adsorption of hydrogen on both clean and oxidised surfaces were continued by Balooch and Hamza [10]. Hydrogen dosed onto Ar^+ sputtered and vacuum annealed surfaces, produced TPD spectra with a single desorption peak in the range 370 – 520 K centred at 450 – 410 K, with increasing coverage. The peak was determined to be second order with an activation energy of 79 ± 12 kJ mol^{-1}. The absolute hydrogen sticking probability was estimated from the TPD spectra as 0.04, with a saturation coverage of 0.15 ML. The absolute sticking probability of hydrogen on oxidised uranium was found to be $6x10^{-4}$, significantly lower than on the clean surfaces. A single peak at 500 K dominated the TPD spectra of hydrogen desorption from the oxidised surface. This peak is ~70 K higher than the observed desorption temperature of hydrogen from the clean surfaces. Therefore, the authors assigned this to the decomposition of OH_{ads} species, due to the differences in the relative strengths of the OH and UH bonds. The validity of this argument was increased by the hydrogen TPD spectra of water dosed onto clean surfaces. The two desorption peaks, at 360 K and 495 K, were assigned to hydrogen from the metal and OH decomposition respectively. However, this assignment was cast into doubt by the work of Manner and Paffett [11]. They carried out similar experiments using TPD and ultraviolet photoelectron spectroscopy (UPS) surface analysis techniques. Low coverages of water were dosed onto clean uranium, at 85 K. A single desorption peak was seen at ~155 K, which was associated with weakly bound D_2O molecules interacting with more strongly bound D_2O/OD/O species. This is 45 K lower than the peak Winer observed using larger water exposures. Manner *et al* claim that this higher desorption temperature is indicative of a state that is directly interacting with the

metal surface. However, an extensive oxygen/oxide overlayer would have clearly covered the surface investigated by Winer, due to the large amount of oxygen pre-dosing and also due to the dissociation of the adsorbed water molecules. Therefore, it is the conclusion of the author that both Winer and Manner observed weak physisorbed water molecules interacting with more strongly bound oxygen or water species and the difference in temperature is due to experimental errors. Deuterium TPD spectra for D_2O dosed at 85 K showed a broad peak at 185 K attributed to the dissociation of D_2O and/or OD. The higher desorption peaks at 395 K and 435 K were associated with D_2 desorption from an essentially clean surface and one that was essentially covered in oxygen. Low exposures of D_2O at 300 K showed only one peak at 395 K, assigned to D_2 desorbing from clean surfaces. At coverages above 3 L this peak was replaced by a peak at ~340 K, decomposition of hydroxyl groups, and a peak at 490 K, surface-bound D_2 desorbing. This assignment is contradictory to that of Balooch and Hamza, see above. However, the use of UPS and the inclusion of low coverage data by Manner adds strength to the peak assignments, which they postulate. A more thorough comparison of data was promised by Manner but never came to publication.

This work will investigate the adsorption of hydrogen on clean and oxidised uranium surfaces using TPD, XPS and supersonic molecular beam techniques in an attempt to further elucidate the mechanism for hydrogen adsorption on clean and oxygen modified uranium surfaces.

4.2 Experimental

All the experiments reported in this chapter were performed in a UHV system, with a base pressure of $<1x10^{-10}$ mbar, described in detail in Section 2.1.

The polycrystalline depleted uranium (AWE plc.) sample was cleaned by repeated cycles of hot (600 K) and cold (293 K) argon ion bombardment. The cleanliness of the sample was followed by XPS analysis of the U $4f_{7/2}$ region.

The initial sticking probability measurements were calculated using the King and Wells reflection-detection method, Section 3.2. The molecular beam gas mixtures used were 1% hydrogen in helium and 4% hydrogen in argon or neon. Two mass flow controllers (Bronkhurst Hi-Tec) were used to maintain the gas mixtures. All the gases used were 99.9995% purity (BOC gases). The nozzle temperature was varied from 293 to 900 K depending on the incident energy of interest. The molecular beam was used to dose hydrogen normal to the surface in all of the TPD experiments. In all cases the 1.3 mm aperture was used, which produced a beam that was ca. 3 mm in diameter at the sample surface. Oxygen (99.998%, Messer) was dosed using a stainless steel capillary positioned a few centimetres from the front face of the sample.

4.3 Results and Discussion

4.3.1 XPS Analysis

The uranium sample was entirely coated in an air formed oxide overlayer, which was formed during its several months in storage. After its introduction into the UHV system the uranium sample was cleaned using repeated cycles of vacuum annealing at 810 K for ten minutes. This minimal cleaning procedure was intended to remove any adsorbed hydroxyl or carbonyl compounds, and any other surface contaminants, whilst leaving the oxide overlayer relatively intact. Five days after the samples introduction to the UHV system the "initial" surface TPD spectra were collected, see Section 4.3.4. Unfortunately, the XPS system was unavailable until after the "initial" surface series of TPD experiments had been completed. However, the consistency of the TPD spectra indicated that the composition of the surface altered very little during experiments. Shown in Figure 4.1 is an XPS spectrum of the U $4f_{7/2}$ region taken after this series of TPD experiments had been completed. The consistency of this surface was checked by several hydrogen exposures and flash anneals. Using Equations 3.38 – 3.46 from Section 3.51 the sampling depth of the XPS system for both uranium metal and uranium dioxide can be calculated, approximately 12 and 6 layers respectively. Therefore, it can clearly be seen that

there was a significant amount of uranium metal present within the top few surface layers. There are a few possibilities for the significant metallic nature of the surface. Using Auger depth profiling, Swissa *et al* [12] observed a redistribution of oxygen and uranium at the metal-oxide interface due to vacuum annealing at temperatures in excess of 723 K. The metal became segregated out through the oxide and at the same time the oxide was found to become redistributed into the metal in a diffusion like process, E_D = 64.43 $kJmol^{-1}$ and $D_o = 1.1x10^{-9}$ cm^2s^{-1}. However, the effect of diffusion on the oxide was expected to be minimal due to the relatively short anneal times and the large thickness of the air formed oxide that would have been present. There is also the possibility that the low oxide coverage is due to a combination of subsurface regions of uranium metal and surface regions, which have become exposed due to cracks forming in the oxide. There is a significant mismatch between the crystal structures of uranium (orthorhombic) and uranium oxide (face centred cubic for UO_2). If it is assumed that the oxide will grow with preference to the underlying metal then defects and discontinuities in the highly polycrystalline metal will cause misfits in the oxide that will destabilise its growth mode. This leads to the formation of cracks and the establishment of a critical oxide thickness. Another possibility is the reaction of the oxide with adsorbed hydrogen. Using theromgravimetry Pijolat *et al* [13] followed the reduction of U_3O_8 to UO_2 by hydrogen at 783 K, at partial pressures ranging from 1 – 40 kPa, with the desorption of water being the rate limiting step. The reduction of hyperstoichiometric UO_2 by atomic hydrogen has also been observed by Abrefah *et al* [14]. Using a modulated molecular beam technique a collisionless mixed beam of H/H_2 was dosed, from which the atomic portion chemisorbed with a sticking probability of 0.7 ± 0.1. The majority of the chemisorbed atoms recombined, while a small proportion was seen to react with interstitial oxygen to produce water. They also found that atomic hydrogen was unable to further reduce stoichiometric UO_2. In Figure 4.1, the position of the U^{4+} peak at 380.1 eV is indicative of near stoichiometric UO_2 being present on the surface [15; 16]. However, during our own experiments no water was seen to desorb from the surface during hydrogen exposure. Therefore, the appearance of a significant amount of metal on the "initial" surface can be attributed to a combination of oxide reduction, oxide defect formation and the oxide diffusing into the bulk

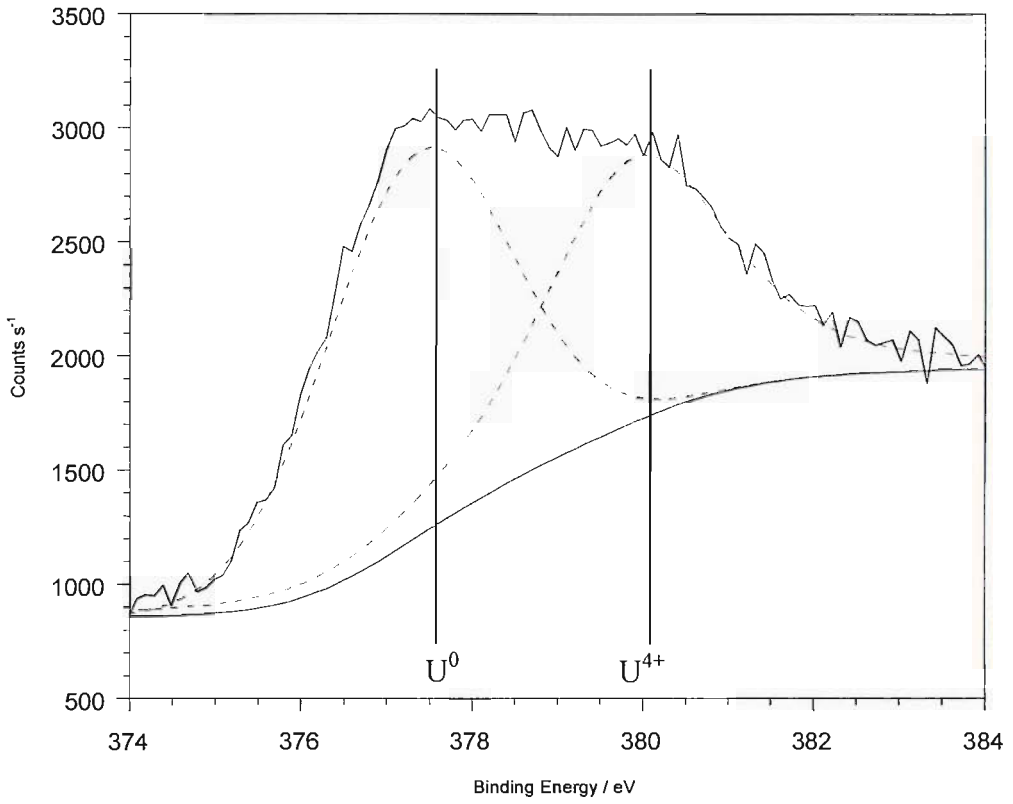

Figure 4.1 - XPS spectra of the U $4f_{7/2}$ region for the "initial" surface, with curve fitting data.

In order to control the growth of the oxide overlayer, oxygen (99.998%, Messer) was progressively dosed onto a clean surface, produced by several sputter / anneal cycles. The formation of this overlayer was monitored by XPS analysis of the U $4f_{7/2}$ region. A cumulative dose of approximately 300 L was necessary to form a near saturated oxide overlayer, Figure 4.2. Even after the surface was exposed to this large amount of oxygen there was there was still a metal peak observed in the U $4f_{7/2}$ region. We attribute this to subsurface regions of metal within the top few atomic layers of the sample, see above for sampling depths. The stability of the oxide formed was determined by flash annealing to 810 K, with XPS spectra taken both before and after annealing, see Figure 4.3. The consistency between spectra was an indication of a stable surface structure. This enabled experiments to be performed with a confident knowledge of the surface composition.

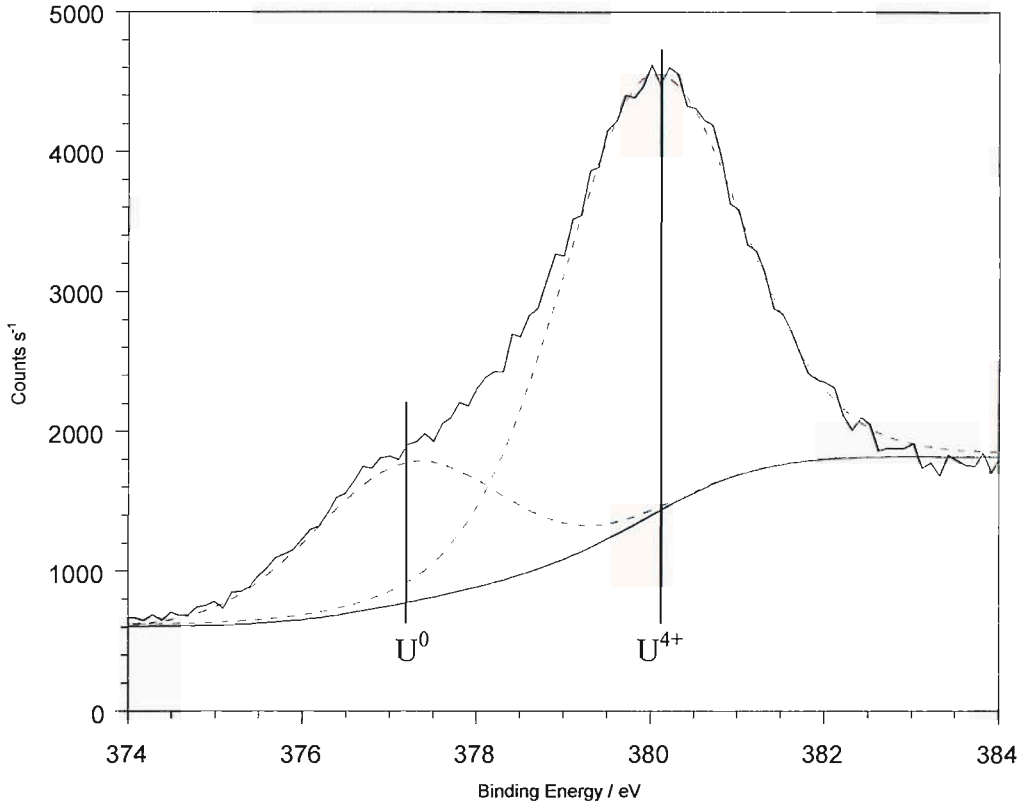

Figure 4.2 – XPS spectra of the U $4f_{7/2}$ region of the predominantly oxidised uranium surface, with curve fitting data.

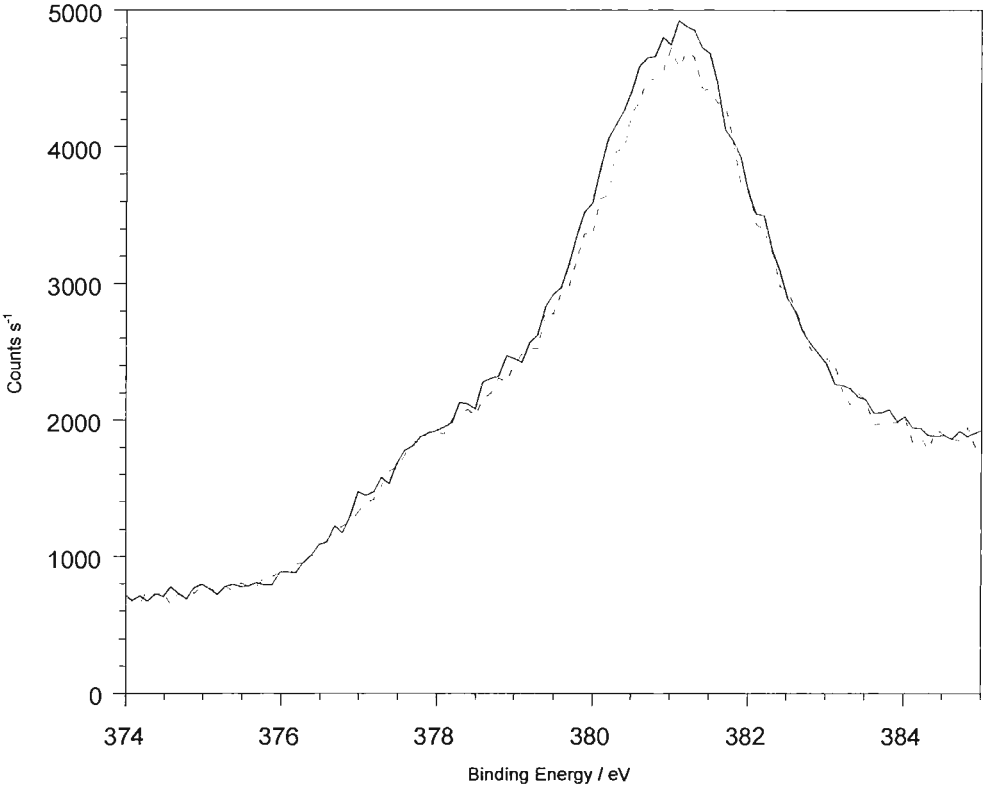

Figure 4.3 – XPS spectra of the U $4f_{7/2}$ region of the predominantly oxidised uranium surface taken before (—) and after (- -) a series of TPD experiments

The oxide overlayer created for the previous series of experiments was removed by repeated cycles of hot (600 K) and cold (293 K) ion bombardment, followed by flash annealing to 810 K. Figure 4.4 shows the progress of the cleaning process. The U $4f_{7/2}$ peak position relating to the metal is reasonably consistent at 377.3 eV. However, as the sample was progressively cleaned the position of the oxide peak is observed to shift by 0.5 eV, from 380.8 to 380.3 eV. XPS studies by Allen *et al* [15-17] observed a similar shift during the reduction of a hyperstoichiometric UO_{2+x} sample. They also observed a satellite peak positioned at 8.2 eV to the high binding energy side of the U 4f peaks, which was attributed to the presence of anion defect clusters within the UO_{2+x} species. However, the U $4f_{7/2}$ spectra range used in this study was not sufficiently wide enough to include direct observations of this satellite peak. Even after intensive cleaning there was still a peak within the U $4f_{7/2}$ region corresponding to the presence of UO_x species, Figure 4.5. The presence of the oxide can, in part, be explained by the nature of the uranium sample and the orientation of the XPS system. The edges of the uranium sample had become slightly curved due to the intensity of the cleaning procedure, this coupled with the large angle between the XPS gun and the detector (~120°) meant that it was highly probable that a small proportion of the rear of the sample was being analysed. No cleaning procedure had been performed on this surface and therefore there would have been a significant level of oxide present. The presence of sub-surface regions of uranium dioxide was also considered to be a possibility. As with the predominantly oxidised surface flash annealing (810 K) was used to test the stability of the surface formed. Therefore, the surface of the sample was considered to be almost completely oxide free for the TPD measurements of Section 4.3.2.

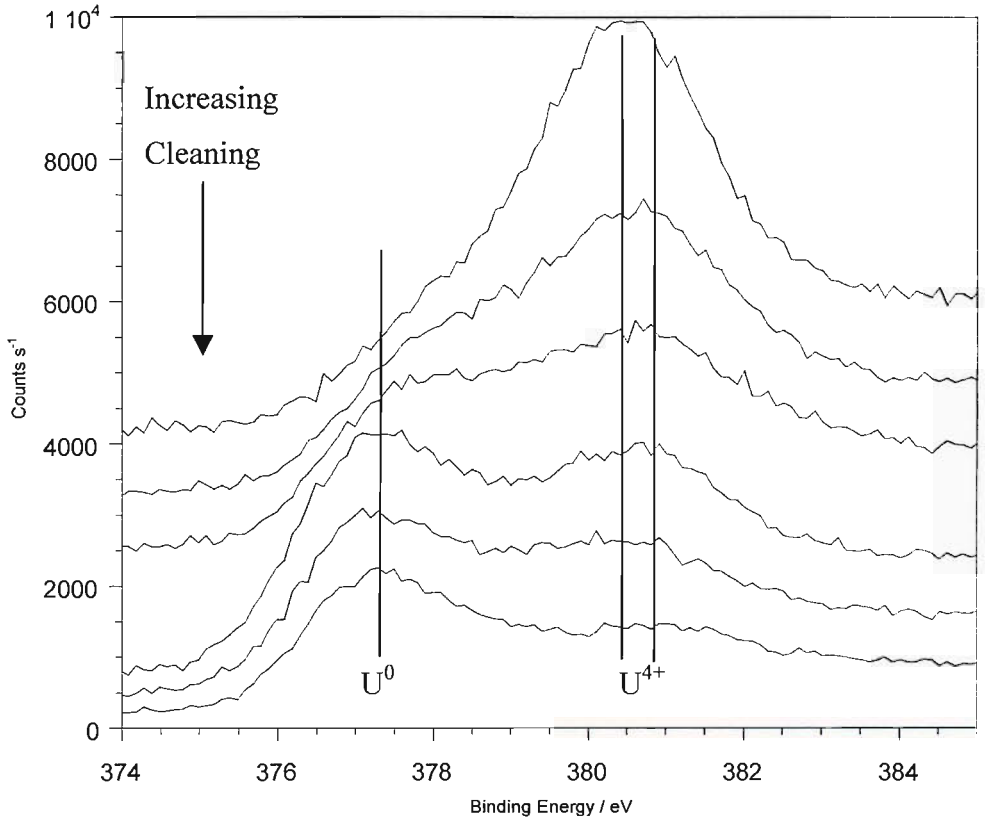

Figure 4.4 – XPS spectra of the U $4f_{7/2}$ region during the cleaning process.

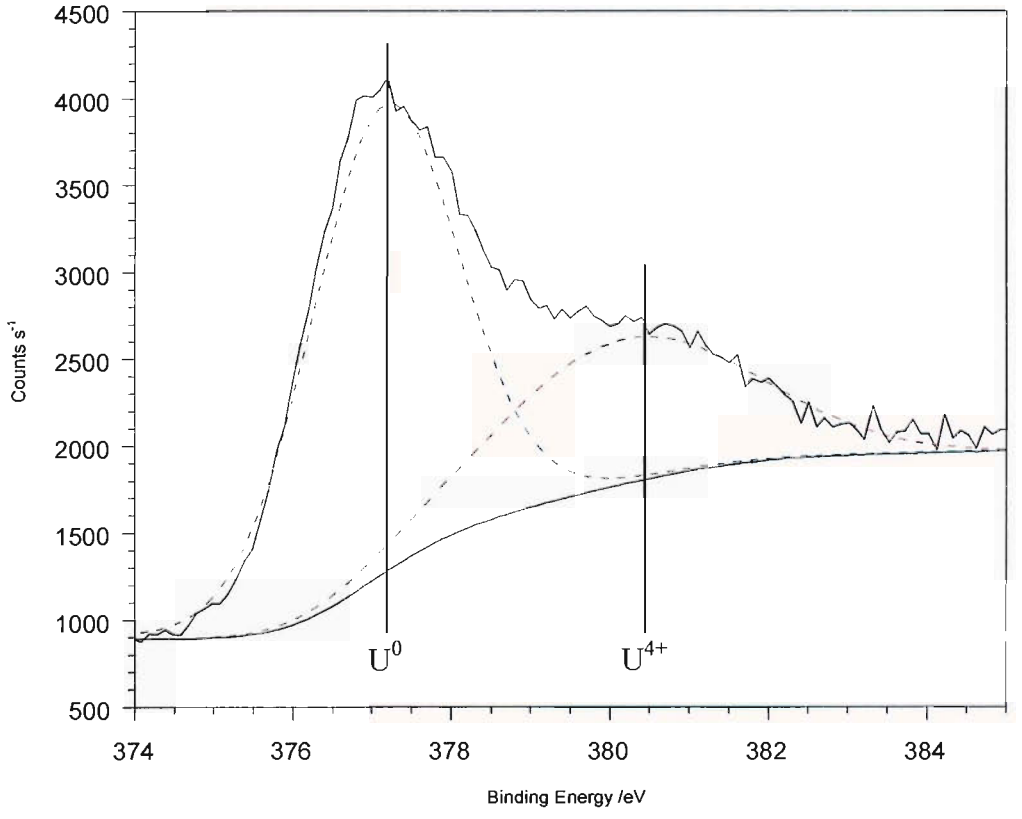

Figure 4.5 – XPS spectra of the U $4f_{7/2}$ region of the clean uranium surface, with curve fitting data.

4.3.2 Hydrogen TPD On Clean Uranium Surfaces

The uranium surface was cleaned using several sputter anneal cycles, detailed in Section 2.2.2. This procedure was repeated until XPS analysis showed a consistent and stable surface composition, Figure 4.5. Exposures of the surface to hydrogen were made using a pure beam, 63 meV, with the surface temperature kept at 160 K throughout. Hydrogen was seen to desorb in the temperature range of 320 to 580 K, with the peak position (α_1) decreasing from 450 to 410 K with increasing coverage, see Figure 4.6. The single desorption peak was also corroboration for the earlier assumption from the XPS spectra that the surface was clean. The insert in Figure 4.6 shows the dependence of the surface coverage upon hydrogen exposure. The coverage was calculated by the ratio of the number of adsorbed atoms to an estimate of the number of possible adsorption sites. From this, the saturation coverage was estimated to be 0.22 ± 0.05 ML. This is in good agreement with Balooch's value of 0.15 ML, with a surface temperature of 300 K [10].

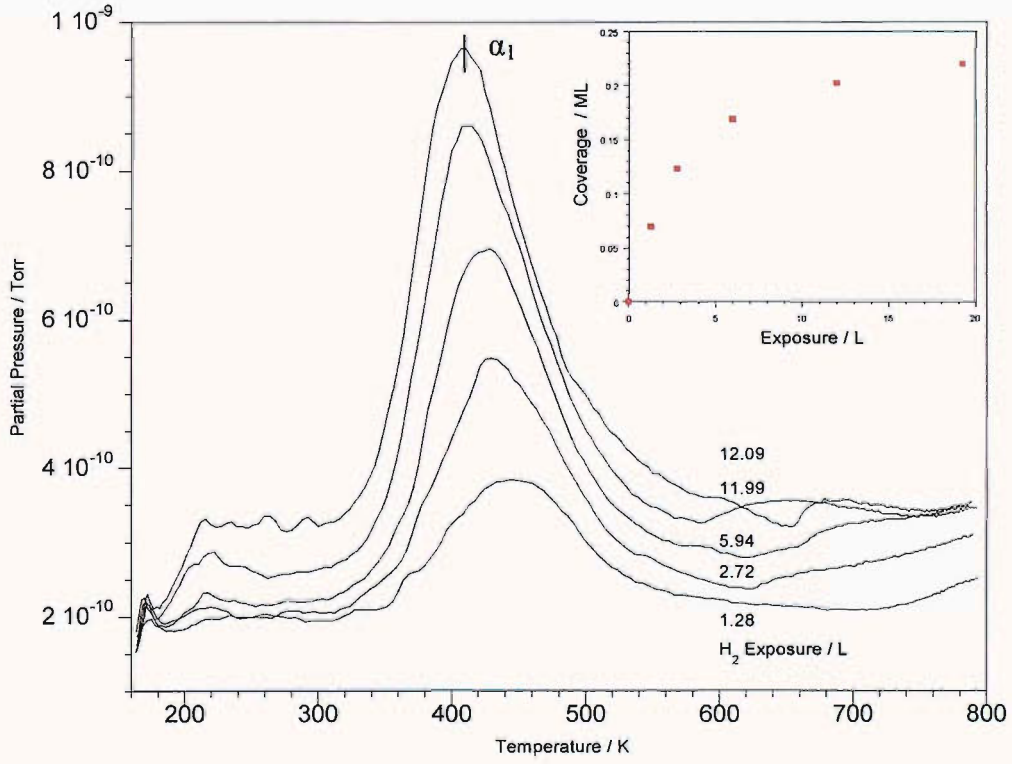

Figure 4.6 – TPD of H_2 dosed onto a clean surface using a pure beam. E_i = 63 meV, T_s = 160 K and heating rate = 5 Ks^{-1}. The insert shows the dependence of the coverage upon hydrogen exposure.

The symmetrical peak position and the shift in position to lower temperatures, with increasing coverage, are both characteristics of a second order desorption process. However, it is highly probable that the desorption process has a non-integer reaction order, in which case the equations given in Section 3.4 will not be applicable. Therefore, in order to calculate the activation energy of desorption, leading edge analysis must be used, utilising the Polanyi-Wigner equation:

$$\ln\left(\frac{d\theta}{dT}\right) = \ln v + n\ln\theta - \frac{E_{des}}{RT} \qquad \text{Equation 4.1}$$

This method has the advantage that the minimum of assumptions are made. A small section of the leading edge of the TPD spectrum is analysed, where the coverage does not change appreciably. A plot of $\ln(d\theta/dt)$ versus 1/T will yield a straight line with a gradient of $-E_{des}/R$ and intercept $\ln v + n\ln\vartheta$.

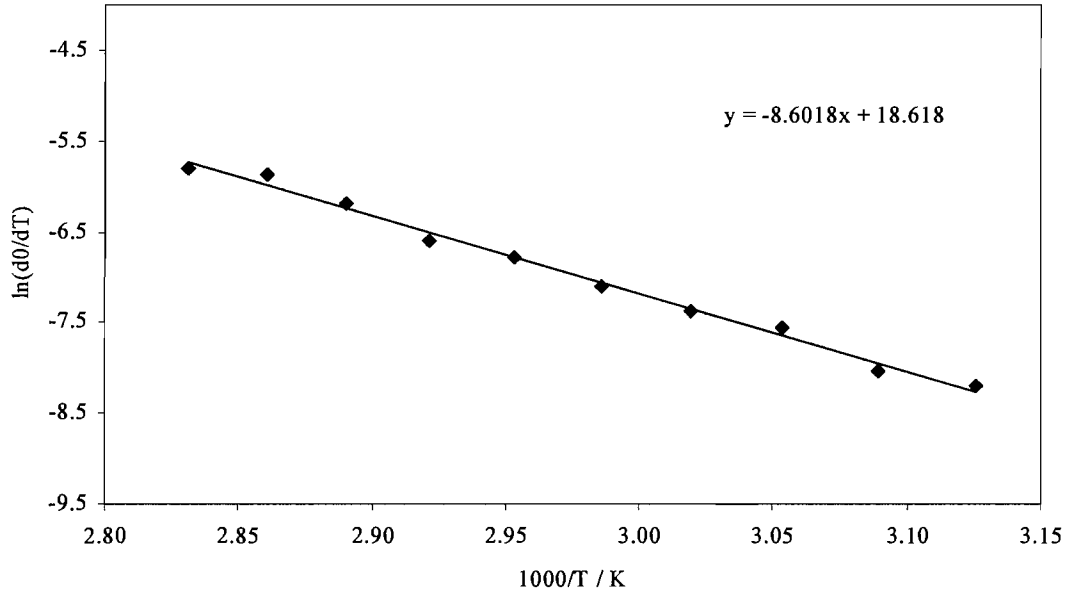

Figure 4.7 – Leading edge analysis $\ln(d\theta/dt)$ versus 1/T for the 12.09 L H_2 exposure TPD spectra from Figure 4.6.

For each of the spectra in Figure 4.6, leading edge analysis was performed, an example plot is shown in Figure 4.7. The average activation energy of desorption was calculated to be 72 ± 10 $kJmol^{-1}$, the uncertainty of the reaction order precludes any estimation of the frequency factor from being made. This compares favourably to the results of Balooch, who determined the activation energy of hydrogen desorption from clean uranium to be 79 ± 12 $kJmol^{-1}$.

4.3.3 Hydrogen TPD On Predominantly Oxidised Uranium Surfaces

The oxide overlayer was prepared by progressive oxygen doses onto an initially clean surface. The formation and stability of the oxide was followed by XPS, see Figures 4.2 and 4.3. Hydrogen was dosed directly onto the oxygen prepared surface using seeded beams over a range of energies, with the surface temperature kept at 160 K throughout, see Figures 4.8 - 4.11. Hydrogen desorption occurs over the temperature range 180 to 780 K. The dominant β_1 peak at 470 K is seen to increase in intensity with increasing exposure and beam energy. The peak temperature appears to be independent of exposure, which suggest a first order process is taking place. Using Equation 1.15, the activation energy of desorption is calculated to be approximately 121 $kJmol^{-1}$. Balooch *et al* [10] observed a single hydrogen desorption peak when hydrogen was dosed onto a prepared oxide surface. The peak was centred around 500 K and was attributed to the decomposition of two adsorbed OH molecules to oxygen and hydrogen. There is also a previously unreported high temperature β_3 peak at 640 - 680 K that is present at all the beam energies used. Danon *et al* [8] observed a peak at 650 K but this was only after a thin surface hydride layer was formed, no such layer would have been present during these experiments due to the low hydrogen exposures used. The α_1 peak observed for the clean surface, at 410 - 450 K, was not observed in any of the spectra shown below, which suggests that there was either no exposed metal or that the peak was quickly saturated and masked by the appearance of the β_1 peak at 470 K. The latter argument can be discarded due to the lack of any shoulder formation on any of the TPD spectra, even at low exposures. The former explanation is also substantiated by the justification made in Section 4.3.1 concerning the appearance of the U^0 peak in the U $4f_{7/2}$ region of the XPS spectra.

Figure 4.12 shows a comparison of beam energies for similar hydrogen exposures of 0.03 L. There are several distinct features that should be noted. The most interesting of which is the appearance of the low temperature β_2 peak, ca. 250 K. At low energies this peak is almost non-existent, however, as the beam energy is increased, as does its significance. At high beam energies there is also the suggestion that a second low temperature peak would become resolved if the sample temperature were lowered further. Another feature to note is that as the beam energy is increased there is a substantial increase in the amount of gas that can be accommodated on the surface at this exposure. This suggests that the increase in beam energy allows a direct dissociation channel to be more easily accessed by adsorbing molecules, see Section 4.3.5 for further explanation. This mainly affects the β_1 and β_2 peaks at 460 K and 250 K respectively.

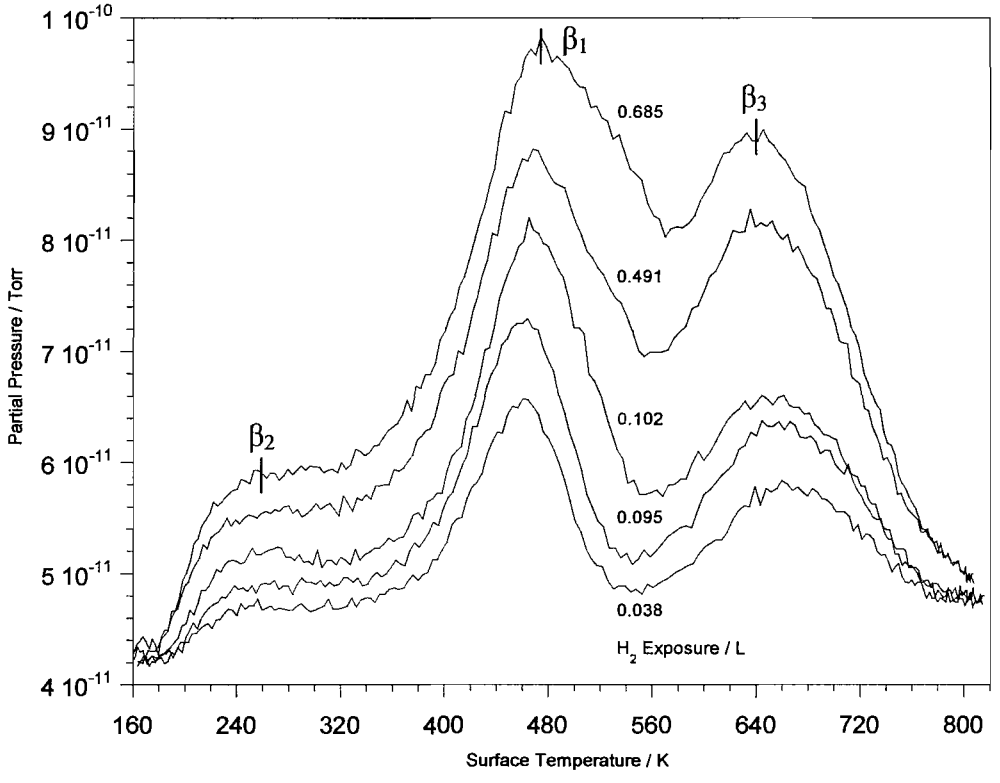

Figure 4.8 – TPD of H_2 dosed onto a predominantly oxidised surface using an Ar seeded beam. $E_i = 3$ meV, $T_s = 160$ K and heating rate = 5 Ks^{-1}.

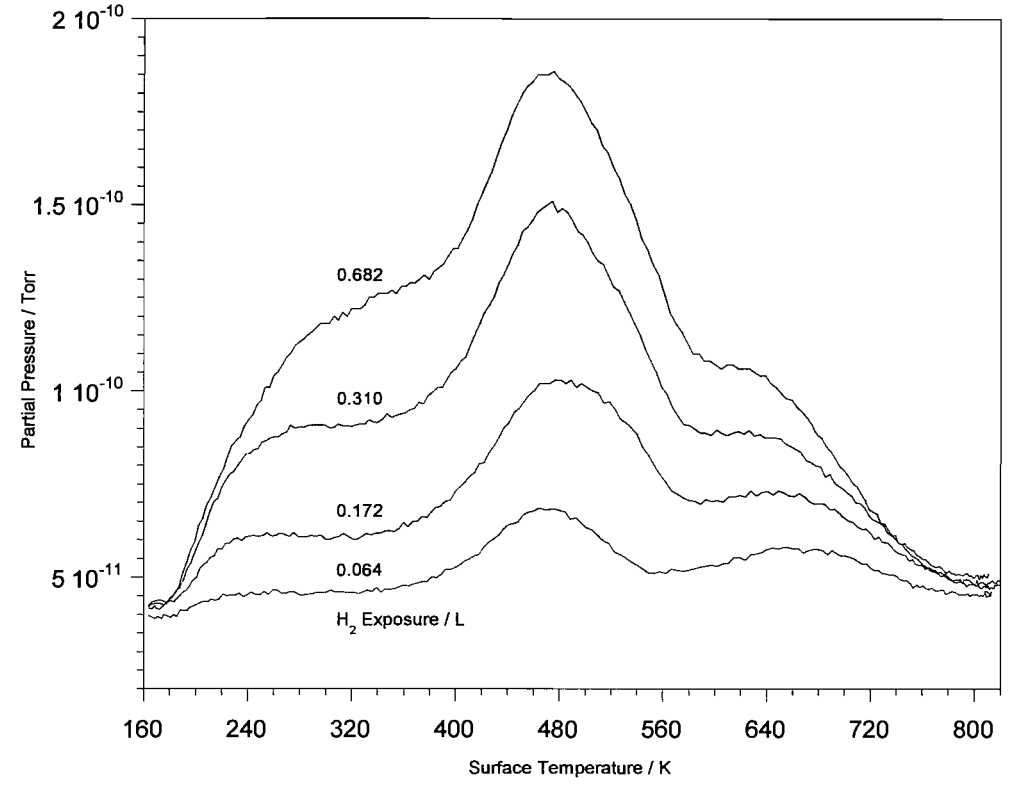

Figure 4.9 – TPD of H_2 dosed onto a predominantly oxidised surface using an He seeded beam. E_i = 63 meV, T_s = 160 K and heating rate = 5 Ks^{-1}.

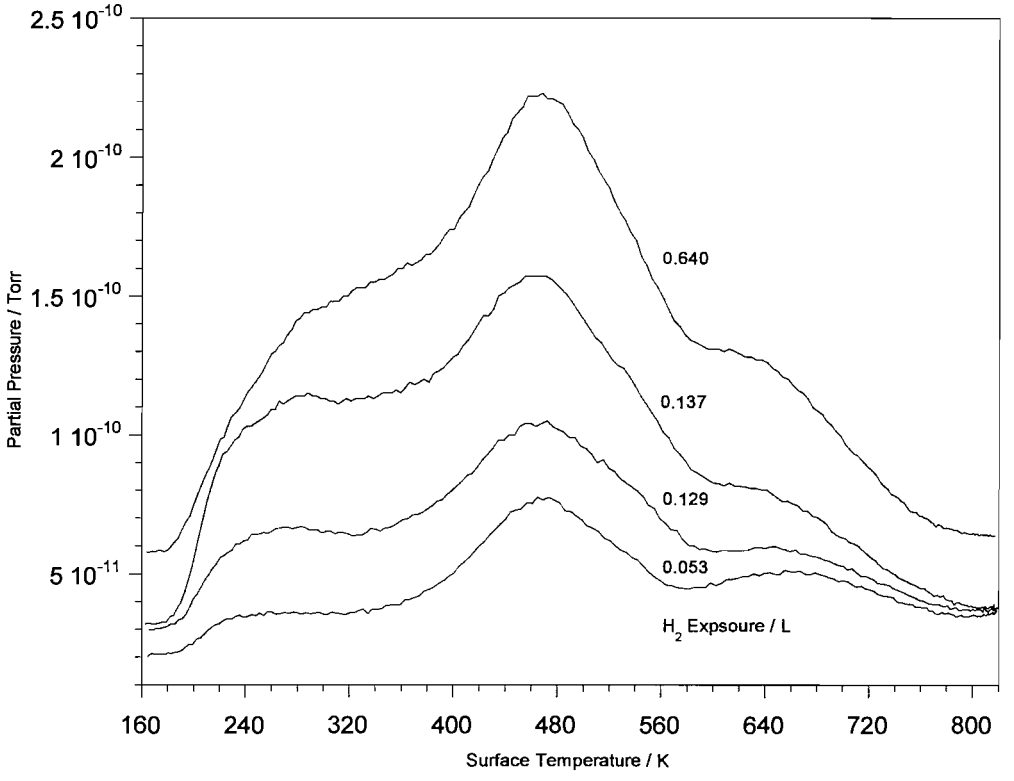

Figure 4.10 – TPD of H_2 dosed onto a predominantly oxidised surface using a He seeded beam. E_i = 149 meV, T_s = 160 K and heating rate = 5 Ks^{-1}.

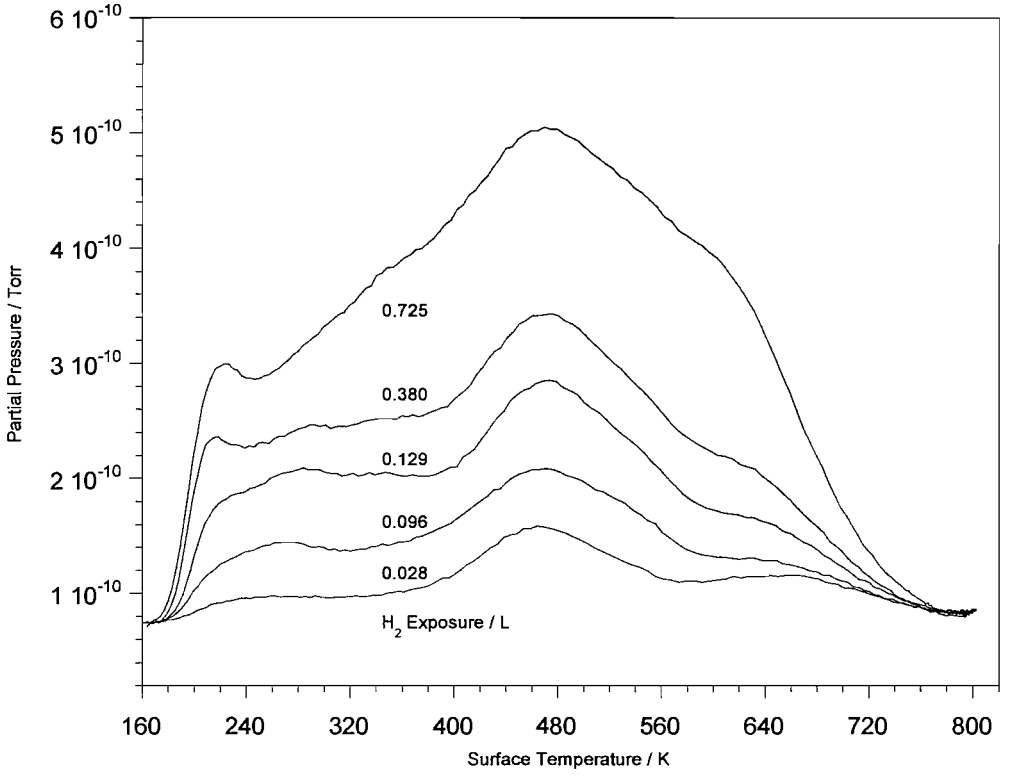

Figure 4.11 – TPD of H_2 dosed onto a predominantly oxidised surface using a He seeded beam. E_i = 189 meV, T_s = 160 K and heating rate = 5 Ks^{-1}.

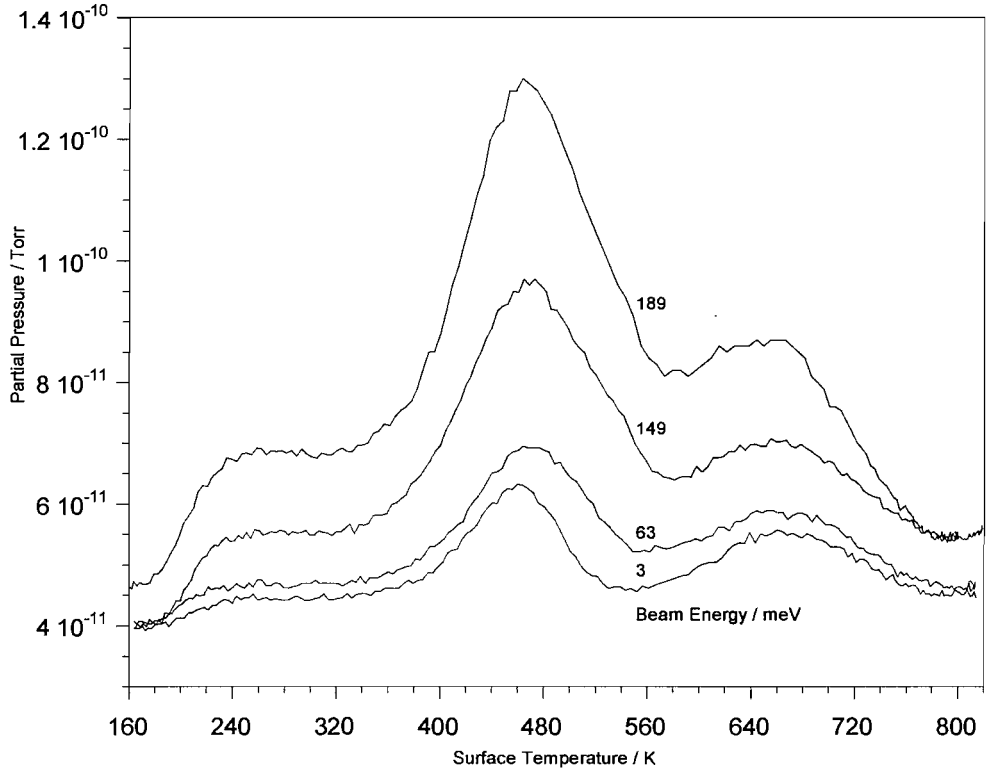

Figure 4.12 – TPD of the predominantly oxidised surface exposed to 0.03 L of H_2 using seeded beams at a number of incident energies. T_s = 160 K and heating rate = 5 Ks^{-1}.

4.3.4 Hydrogen TPD On "Initial" Uranium Surfaces

Prior to this series of TPD experiments, the sample was repeatedly annealed at 810 K for ten minutes. Hydrogen was dosed normal to the surface using seeded beams, at 3 and 63 meV, shown in Figures 4.14 and 4.15 respectively. There are several interesting points to notice when comparing the "initial" series of TPD spectra to those of the clean and predominantly oxidised surfaces. At low energy, 3 meV, the dominant peak is the high temperature β_3 peak at ca. 650 K. The symmetrical peak position and the fact that the peak temperature is seen to shift to lower temperatures with increasing exposure, from 665 K to 650 K, both indicate a second order desorption process. The β_3 peak was only ever observed in the presence of a surface oxide species. It can therefore be postulated that this peak is related to the presence of surface oxides, which lead to hydrogen being strongly bound to the surface. The polycrystalline nature of the surface and the high binding energy of this hydroxyl species suggest that the β_3 peak is related to desorption from edges or other defect sites that would be present on the oxide. XPS of this surface showed that there would have been a significant amount of exposed metal inferring that the oxide would have been present as clusters, or islands, which would increase the importance of edge effects and therefore the dominance of the β_3 peak. The appearance of the β_3 hydroxyl species on the predominantly oxidised surfaces can also be attributed to the polycrystalline nature of the surface leading to a number of edge and defect sites being present.

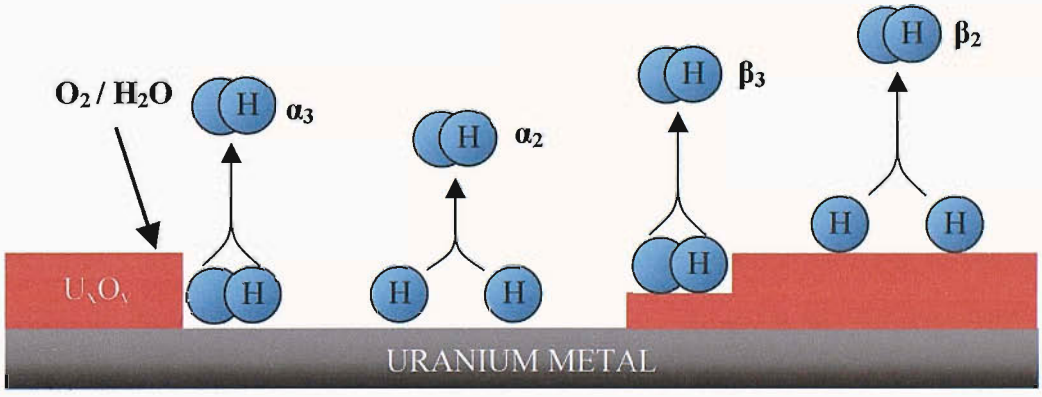

Figure 4.13 – Schematic of the hydrogen desorption species from the "initial" uranium surface.

At 63 meV, the most distinct difference is that the low temperature β_2 peak, ca. 250 K, is now the dominant feature. The β_2 peak was only seen when there was some form of oxide present. Therefore, it is proposed that the β_2 species is due to hydrogen weakly bound as a hydroxyl species. The low peak temperature suggests that the metal has a significant influence on the oxide, which decreases the relative strength of the O-H bond.

At both beam energies studied there is a weak peak (α_2) at 450 K. The peak position is reminiscent of the α_1 desorption species observed for hydrogen desorbing from the clean surface, Section 4.3.2. The XPS spectrum, Figure 4.1, of the "initial" surface also indicates that there were possibly large regions of exposed metal that would have been available for hydrogen adsorption. At 63 meV, the α_2 peak quickly becomes saturated as the hydrogen exposure is increased, whereas at lower beam energies, 3 meV, this α_2 peak steadily increases with exposure. This is concomitant with the indirect dissociation channel associated with hydrogen adsorption on clean uranium; see Section 4.3.5. The α_2 species can therefore be attributed to hydrogen desorption from the metal, which is in the presence of a partial oxide overlayer. On the high temperature side of the β_2 peak at 63 meV there appears to be a shoulder (α_3) at ca. 350 K that appears to grow in intensity with increased exposure. However, at lower beam energies the α_3 shoulder feature does not appear. The oxide present on the surface would have been highly defected due to the polycrystalline nature of the sample and that the oxide was air formed. Therefore this peak could be the result of either edge effects or the population of unfavourable bonding sites located near to the interface of the metal and oxide regions that can only be accessed when the approaching molecules have sufficient incident translational energy. Figure 4.13 shows a schematic of the assignments for the hydrogen desorption species from the "initial" uranium surface. It should also be noted that neither TPD spectra exhibit a peak at 470 K, which dominated the predominantly oxidised TPD spectra of Section 4.3.3 and was associated with hydrogen desorption from the oxygen formed oxide. The absence of this peak could, in part, be explained by the nature of the surface oxide, where there would be a significant number of defects and discontinuities present that would provide preferential channels for the hydrogen to pass to the underlying metal. Moreno *et al* [18] found that there was good correlation between these discontinuities and the preferential sites for hydride

formation. This work was also substantiated by that of Arkush *et al* [19] who observed four different families of hydride nuclei, which were dependent on the thickness of the oxide present and the type of defect present. There will also be a difference in the stoichiometry of the oxide overlayer present due to the "initial" oxide being air formed, while dosing pure oxygen formed the predominantly oxidised uranium surface.

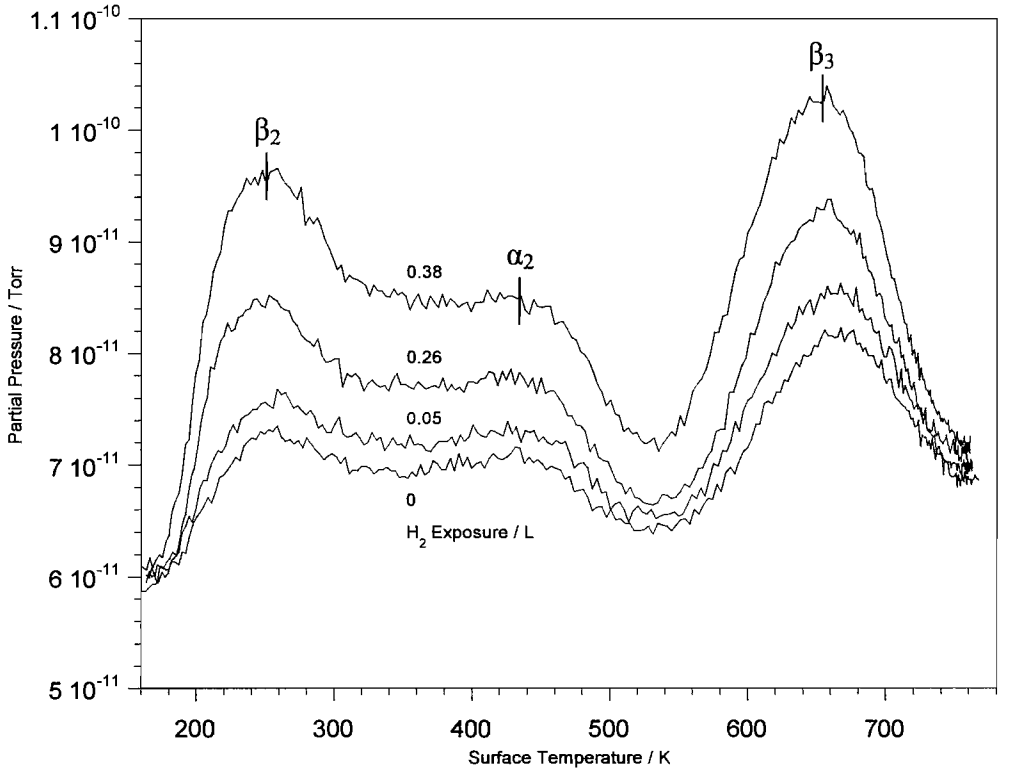

Figure 4.14 - TPD of H_2 dosed onto the "initial" surface using an Ar seeded beam. E_i = 3 meV, T_s = 160 K and heating rate = 5 Ks^{-1}.

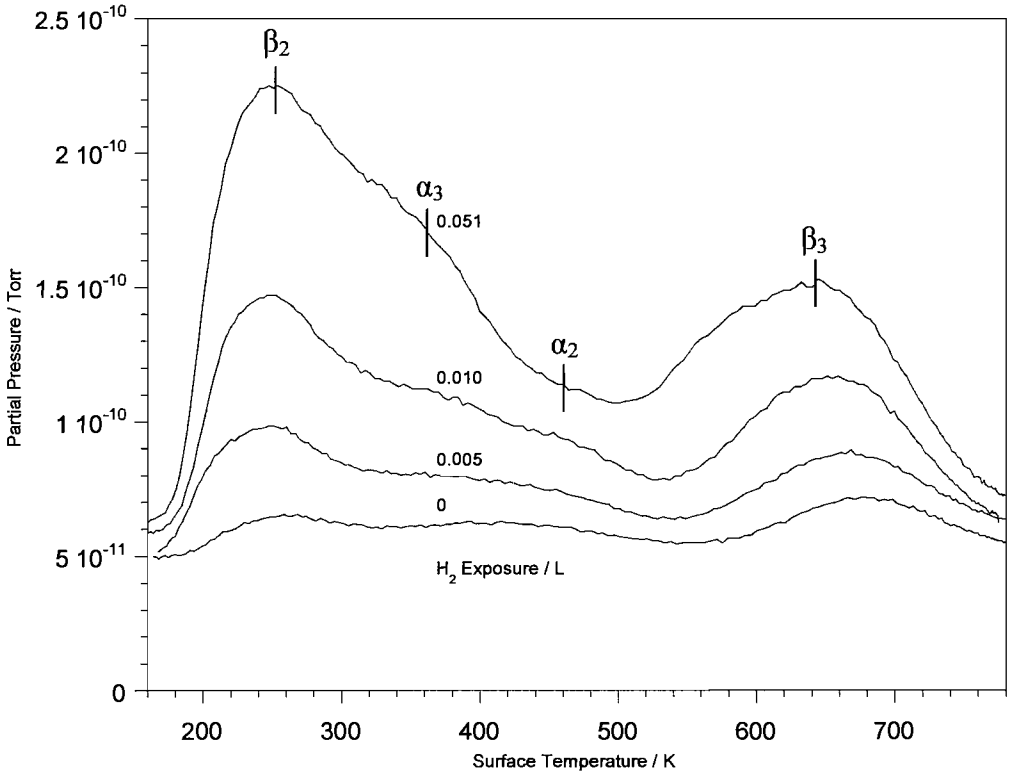

Figure 4.15 - TPD of H_2 dosed onto the "initial" surface using a He seeded beam. E_i = 63 meV, T_s = 160 K and heating rate = 5 Ks^{-1}.

4.3.5 Hydrogen Sticking Probabilities On Clean And Oxidised Uranium Surfaces

The initial sticking probability of hydrogen on a clean uranium surface was measured using the King and Wells reflection-detection method, see Section 3.4 for details. The sticking probabilities observed on the clean surface are at the limit of the King and Wells technique, however there was no doubt that the pressure drop seen was due to hydrogen sticking. The hydrogen was dosed using a combination of seeded and pure beams with the surface temperature kept at 160 K throughout, see Figure 4.16. The hard-cube model is also shown in Figure 4.16, it assumes that that a hydrogen gas molecule is a rigid elastic sphere that interacts with a single cube of uranium atoms, for more information see Appendix A. From 0 – 65 meV there is a dramatic decrease in the sticking probability as the translational energy is increased. The simple physisorption trapping process of the hard cube model cannot explain this behaviour. However, such a trend has been observed on a number of other metals, including Pt (533) [20], where it was attributed to an indirect dissociation channel. In this situation the molecule weakly chemisorbs on the surface with

sufficiently long lifetime that it can diffuse to an appropriate dissociation site. For example, on the Pt (533) surface hydrogen was found to preferentially dissociate at step defects in this manner. The polycrystalline nature of the sample negates any specific surface site from being attributed to this dissociation channel, however the surface would have been rich in such defects and discontinuities. The indirect channel continues to be active over a very large energy range and does not "switch off" until ca. 250 meV, shown in Figure 4.16. Above 65 meV the sticking probability appears to rise slightly with increasing incident energy. This can be assigned to the increasing dominance of a direct dissociation channel, whereby the molecules dissociate on impact upon the surface. Assuming that the process is non-activated an estimation of the contribution made by this channel can be made, Figure 4.16.

The absolute sticking probability of hydrogen on predominantly oxidised surfaces was estimated by the ratio of the coverage, measured by TPD, to the hydrogen exposure for each of the beam energies presented in Section 4.3.3. From the lowest exposures used the initial sticking probabilities were estimated by extrapolation to zero exposure. Figure 4.17 shows a comparison of the sticking probabilities for both the clean and the predominantly oxidised surfaces. In contrast to the clean surface the sticking probabilities on the oxidised surface appears be dominated by a direct channel, with there being a steady increase in the sticking probability as the incident energy increases. This dissociation channel is broad and appears to be activated with the onset of a barrier at 100 ± 20 meV. Below this point there is still a small amount of sticking apparent, which remains constant over the range $0 - 100$ meV. This indicates that there is a weak indirect channel still present for this surface.

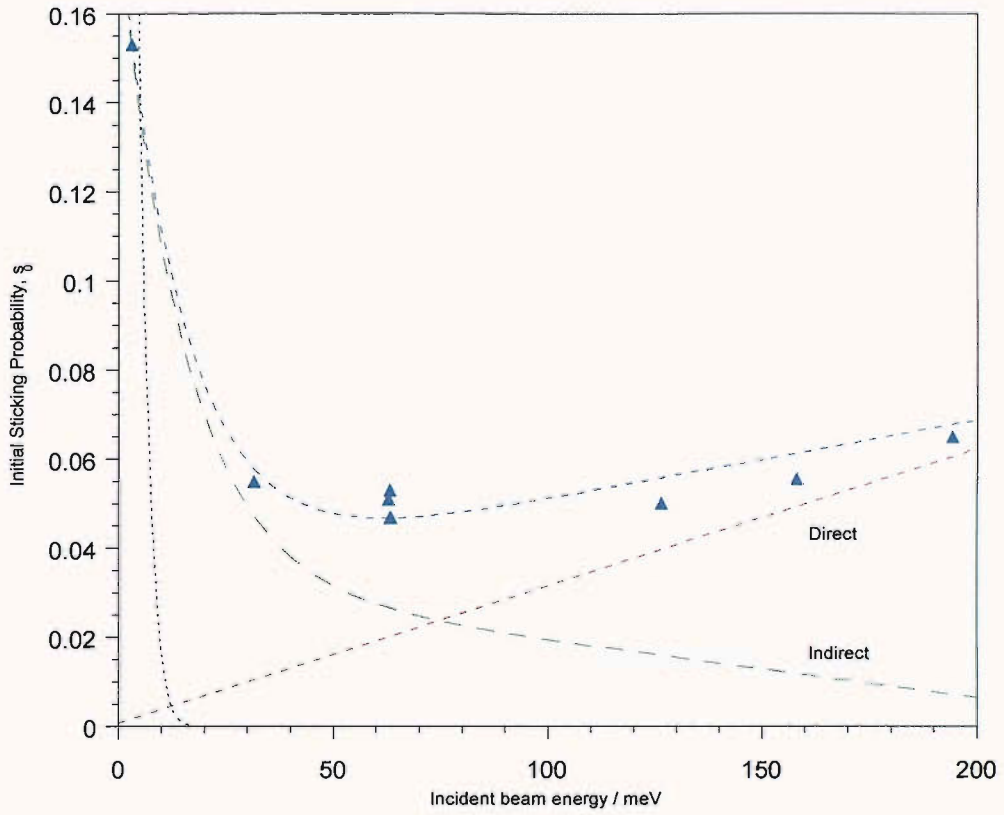

Figure 4.16 – The initial sticking probabilities of H_2 adsorption on clean uranium surfaces, with the direct and indirect channels shown. T_s = 160 K

The absolute sticking probability of hydrogen on clean uranium was calculated to be 8.6×10^{-2}, using the data from Figure 4.6 and a normalised Maxwell-Boltzmann distribution for a gas at 300 K, see Section 3.3. This value is in good agreement with the 0.1 sticking probability measured by Swissa *et al* [9] but it is double the 4×10^{-2} figure published by Balooch for clean uranium surfaces [10]. Using the same method the absolute sticking probability of hydrogen on oxidised uranium was calculated to be 1×10^{-2}. This is significantly greater than the 6×10^{-4} value of Balooch, but this value is also considerably lower than the 6×10^{-2} measured by Swissa. However, if only the direct channel of the oxidised surface is taken into consideration then a value of 7.6×10^{-4} is calculated, which is in good agreement with the work of Balooch. The trend between absolute sticking probabilities on the clean and oxidised surfaces is consistent with the view that oxygen adsorption significantly reduces the amount of hydrogen that can be accommodated on the surface by blocking the dissociation sites used within the indirect channel at low energies.

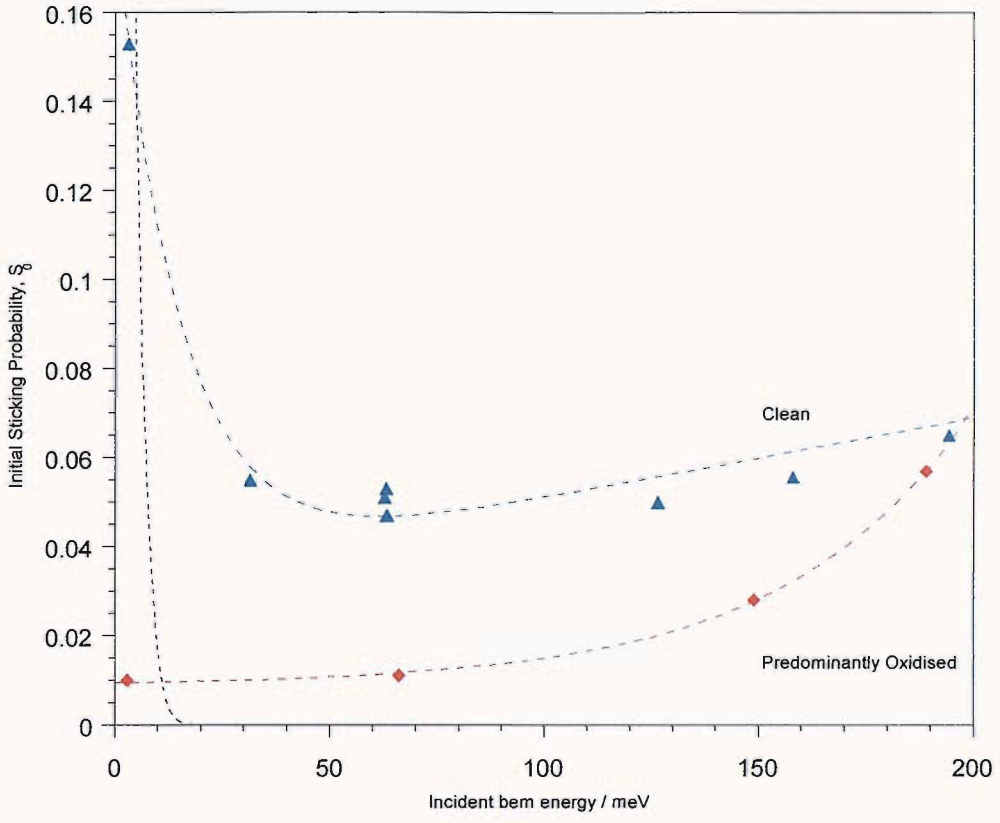

Figure 4.17 – The initial sticking probabilities of H_2 adsorption on clean and oxidised uranium surfaces. $T_s = 160$ K

4.3.6 Effect Of Progressive Oxygen Doses On Hydrogen Adsorption

In order to further investigate the effect of oxygen on the adsorption of hydrogen, oxygen was progressive dosed onto an initially clean surface. Figures 4.18 and 4.19 show a typical series of TPD and XPS result. In all cases, the surface was dosed with 0.6 L of hydrogen from a pure supersonic molecular beam, with an incident beam energy of 63 meV. The oxygen was dosed through a stainless steel capillary positioned a few centimetres from the front face of the sample. In both cases the surface was kept at 160 K throughout.

The initial surface was considered to be clean even though XPS (a) showed a small amount of oxide present, see Section 4.3.1 for further explanation. The single desorption peak (α_1) at 430 K in TPD (a) was also concomitant with the assumption that the surface was clean.

The next stage was to dose a small amount of oxygen, 0.05 L. XPS spectrum (b) showed that the amount of oxide present had increased substantially, however there was still a significant amount of metal within the sampling area, possibly due to subsurface regions, see Section 4.3.1 for details of the XPS sampling depth. TPD (b) taken on this surface shows a considerable decrease in the amount of adsorbed hydrogen. The low coverage and the polycrystalline nature of the surface meant that a detailed analysis of this spectrum, and TPD (d), could not be confidently made.

Immediately after the TPD experiment, the sample was flash annealed to 800 K and XPS spectrum (c) was taken. The oxide peak has almost returned to the same intensity as on the initial surface. In contrast to the initial surface the oxide peak position has now shifted from 380.3 to 380.8 eV. Such a shift is concurrent with a change in the oxide stoichiometry as evidenced by Allen *et al* [16]. They observed a similar shift when a $UO_{2.00}$ sample was oxidised to either U_4O_9 or U_3O_7. It is therefore suggested that the annealing allows more oxygen to be accommodated within the uranium oxide lattice, thus increasing the oxide stoichiometry. Hydrogen TPD (c) taken on this surface showed a significant recovery of the single desorption peak observed in the initial TPD spectrum. However, the recovery is not complete and the peak is now shifted to 436 K, suggesting that the hydrogen coverage has now decreased. This decrease in coverage is possibly due there being some oxygen remaining on the surface, even after annealing, that blocks hydrogen adsorption. However, the TPD spectrum did not show any significant adsorption that has previously been related to the presence of an oxide, i.e. at either 250 K or 600 K.

There followed a further 0.1 L dose of oxygen. XPS spectrum (d) showed a significant increase in the oxide peak intensity in comparison to spectrum (b), which was due to the larger oxygen exposure used. The peak had also shifted back to the position associated with near stoichiometric UO_2. Hydrogen TPD (d) on this surface showed a similar reduction in the amount of adsorbed hydrogen as previously seen in TPD (b). XPS spectrum (e) taken immediately after TPD (d) was comparable to XPS spectrum (c). This was subsequently followed by TPD (e), which once more showed a single α_1 desorption peak, whose position could be related to a decrease in the expected hydrogen coverage. XPS (f) was taken shortly after this and was

equivalent to XPS (e), indicating the stability of the surface throughout the TPD experiments.

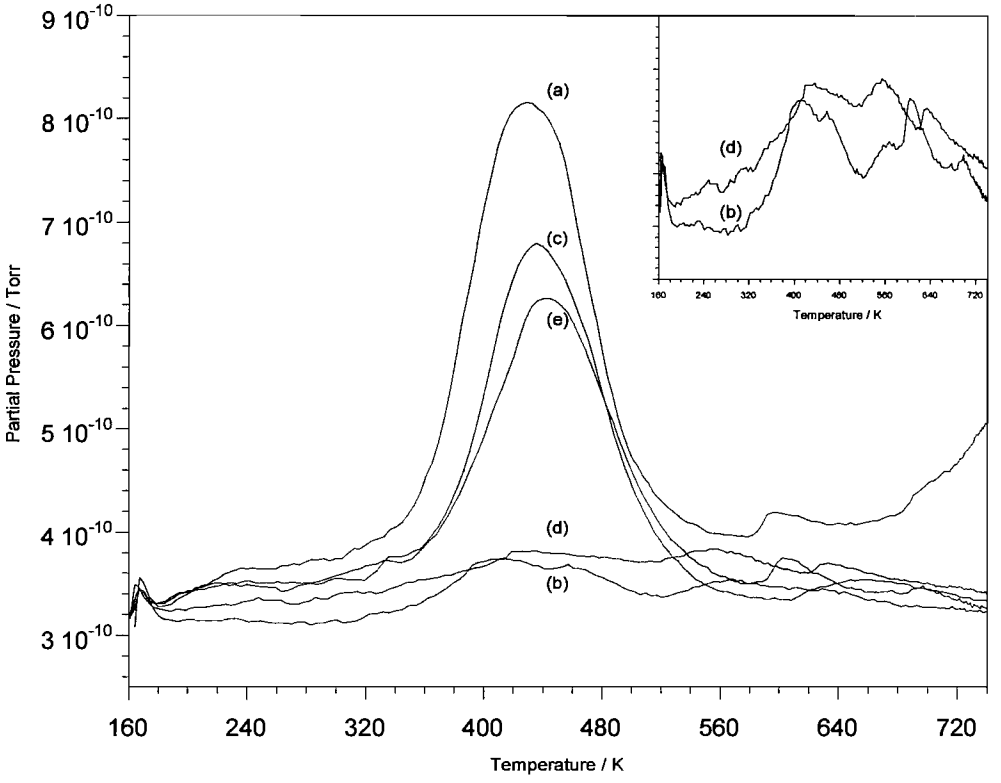

Figure 4.18 – TPD spectra after exposure to 0.6 L of hydrogen, dosed using a pure beam. E_i = 63 meV, T_s = 160 K and heating rate = 5 Ks^{-1}. The insert shows a magnification of spectra (b) and (d).

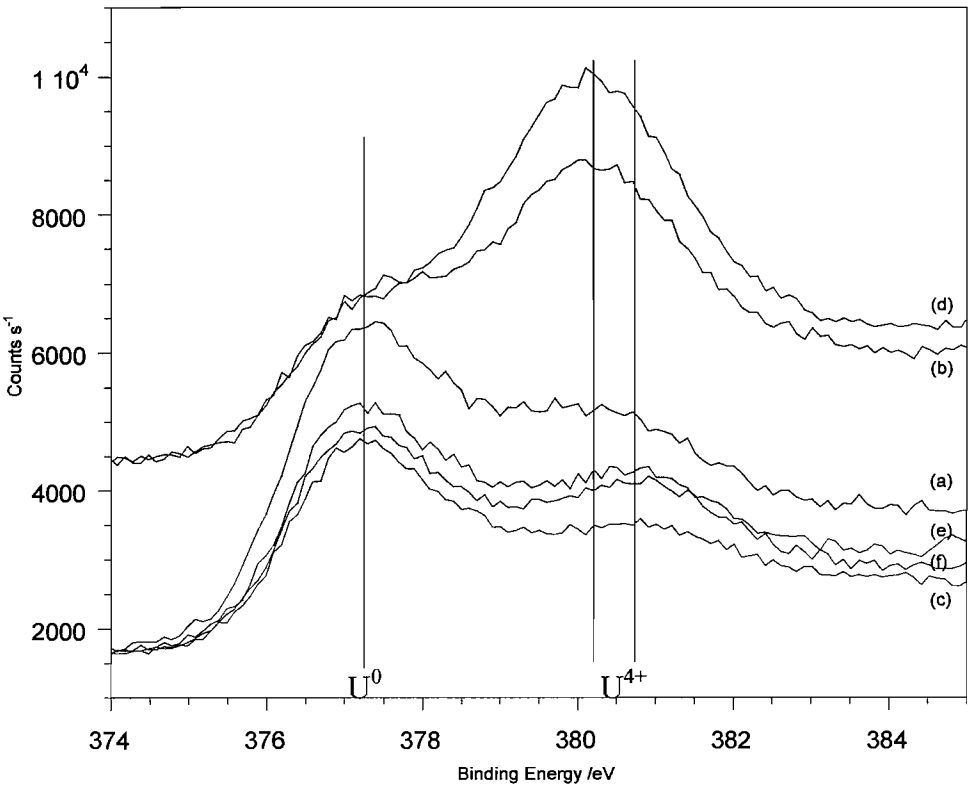

Figure 4.19 – XPS spectra of the U $4f_{7/2}$ region showing the composition of the surface during a series of oxygen doses, hydrogen TPD spectra and flash anneals.

From these observations a number of conclusions can be made about the effect of oxygen pre-dosing on hydrogen adsorption, summarised in Figure 4.20. Initially, oxygen adsorption has a detrimental affect on the amount of hydrogen that can adsorb. This is possibly due to the blocking of defect and other favourable sites that allow molecularly adsorbed hydrogen to dissociate within the dominant indirect channel at 63 meV. Therefore, the only pathway available for dissociation is the direct channel, which is weak until high beam energies are reached, Section 4.3.5. Flash annealing the surface changes both the stoichiometry and coverage of the oxide, as evidenced by a reduction in intensity and a shift in binding energy of the oxide peak in the XPS spectra. Previous experiments have shown that neither oxygen nor water desorbs when the sample is flash annealed, therefore it is highly likely that the oxygen diffuses into the bulk of the sample but in doing so it leaves regions where the oxidation state of the metal has increased. Swissa *et al* [12] also observed surface oxide migration by vacuum annealing. The new surface formed does not fully recover the number of active sites that were previously available for hydrogen dissociation, possible due to the presence of the subsurface oxide. This is

evident by the cumulative decrease in hydrogen coverage that can be correlated to increasing oxygen exposure and flash annealing.

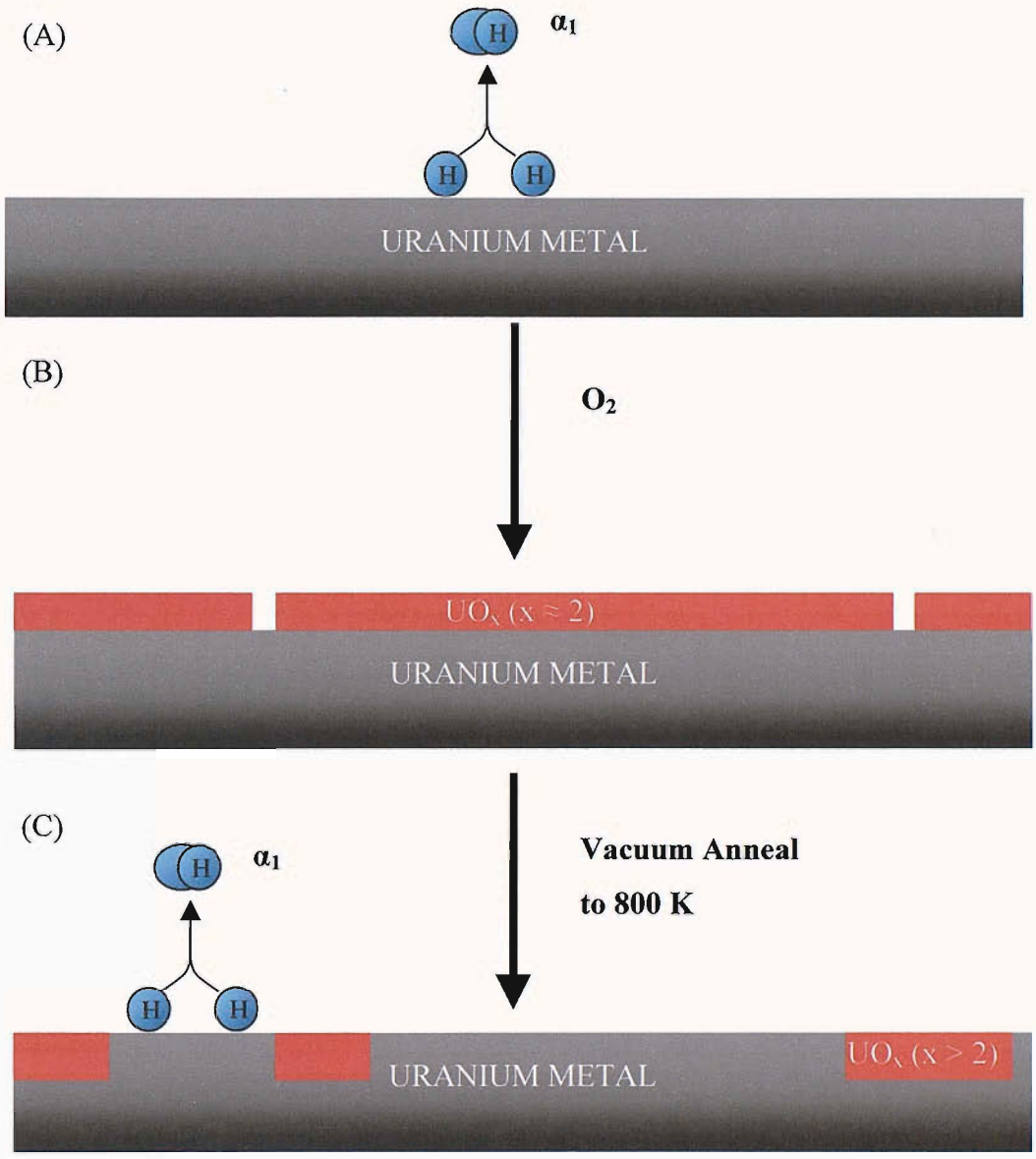

Figure 4.20 – Summary of the effect of oxygen pre-dosing on hydrogen adsorption. (A) Hydrogen adsorbs onto a clean surface. (B) Oxygen is dosed onto the surface forming a near stoichiometric layer. (C) Vacuum annealing to 800 K enables the oxide to increase in stoichiometry and diffuse into the bulk.

4.4 Conclusions

Using a combination of XPS, TPD and supersonic molecular beam experiments the adsorption of hydrogen on clean and oxidised uranium surfaces has been investigated. There is some agreement between these results and the work presented in previous studies [9-11].

An indirect channel dominated hydrogen adsorption on clean uranium with an absolute sticking probability of 8.6×10^{-2}. This produced a single second order desorption peak (α_1) in the TPD spectrum at 450 - 410 K that had a saturation coverage of 0.22 ML. The activation energy of desorption was calculated to be 74.58 ± 7 kJmol^{-1}, which is in good agreement with the literature [10].

In contrast, an activated direct channel dominated the adsorption of hydrogen on predominantly oxidised uranium surfaces with an absolute sticking probability of 1×10^{-2}, although this value was reduced to 7.6×10^{-4} when only the direct channel was considered. The TPD spectra exhibited three desorption peaks in the range 160 - 800 K. The dominant β_1 peak, arising from hydrogen desorption from the oxide, was centred around 470 K and was first order with an activation energy of 121.30 kJmol^{-1}. A low temperature β_2 peak at 250 K became populated, as the incident beam energy was increased. This was associated with weakly bonded hydroxyl groups that were affected by the presence of subsurface metal regions. The high temperature β_3 peak at 650 - 610 K was attributed to the presence of defects or edges on the oxide that increased the strength of the hydrogen bonding to the surface.

The "initial" surface also exhibited three desorption peaks, with a fourth being observed at 63 meV. Unlike the predominantly oxidised surface the β_2 species now dominates. As with the oxidised surface, this was associated with the formation of weakly bonded hydroxyl groups. At 63 meV, an additional peak (α_3) was seen to grow in as a shoulder on the β_2 peak at 350 K. This was attributed to either edge effects or the population of unfavourable sites near the interface of the oxide and the metal. The high temperature β_3 peak was also of greater importance on the "initial" surface, than on the predominantly oxidised surface. This was also assigned to the

presence defects and edges on the oxide as on the oxidised surface. The most significant difference is that there is a weak α_2 peak at 450 K that quickly becomes saturated. This is reminiscent of the α_1 desorption species seen on clean uranium surfaces. There was no definitive peak that could be identified as the β_1 species, which suggests that the oxide present was heavily cracked and defected. Thus, increasing the importance of the β_3 species and providing diffusion channels through which hydrogen can pass to the underlying metal.

Desorption Species	T_{des} / K
α_1	400 – 450
α_2	450
α_3	350
β_1	470
β_2	230 – 300
β_3	600 – 700

Table 4.1 – A summary of the desorption temperatures for the various hydrogen species.

By progressively dosing a small exposure of oxygen onto an initially clean surface, it was shown that surface oxygen species had a significant blocking affect on the adsorption of hydrogen. The adsorbed oxygen dissociates and populates defect sites, and other favourable surface sites; this blocks the indirect channel, leaving only the weaker direct channel available for hydrogen dissociation. Upon flash annealing to 800 K the adsorbed oxygen migrates into the bulk. In doing so it alters the stoichiometry of the oxide by increasing the oxidation state of the metal. Subsequent exposure to hydrogen showed a significant decrease in the expected coverage. This can be explained by a reduction in the number of active dissociation sites that can be used within the indirect channel, possibly due to the presence of subsurface oxide species. These results show that while surface oxide species cause a significant decrease in the amount of hydrogen that will adsorb, some will adsorb whereby it can migrate to the underlying metal and react.

4.5 References

[1] Klaproth, M.H., Chem. Ann. II (1789) 387-403.

[2] Peligot, E., C. R. Acad. Sci. 13 (1841) 417.

[3] Peligot, E., J. Prakat. Chem. 1 (1841) 442-51.

[4] Becquerel, A.H., C. R. Acad. Sci. 128 (1896) 771-7.

[5] Weigel, F., in: J.J. Katz, G.T. Seaborg, L.R. Morss (Eds.), The Chemistry of the Actinide Elements, London, New York, 1986, pp. 169-442.

[6] Lander, G.H., E.S. Fisher, S.D. Bader, Advances in Physics 43 (1994) 1-111.

[7] Winer, K., C.A. Colmenares, R.L. Smith, F. Wooten, Surf. Sci. 183 (1987) 67-99.

[8] Danon, A., J.E. Koresh, M.H. Mintz, Langmuir 15 (1999) 5913-5920.

[9] Swissa, E., I. Jacob, U. Atzmony, N. Shamir, M.H. Mintz, Surf.Sci. 223 (1989) 607-620.

[10] Balooch, M., A.V. Hamza, J. Nuc. Mat. 230 (1996) 259-270.

[11] Manner, W., J.A. Lloyd, M.T. Paffett, J. Nuc. Mat 275 (1999) 37-46.

[12] Swissa, E., N. Shamir, M.H. Mintz, J. Bloch, J. Nuc. Mat. 173 (1990) 87-97.

[13] Pijolat, M., C. Brun, F. Valdivieso, M. Soustelle, Solid State Ionics 101-103 (1997) 931-935.

[14] Abrefah, J.D., D.F. Orlander, D.R., J. Phys. Chem. 94 (1990) 1937-1944.

[15] Allen, G.C., I.R. Trickle, P.M. Tucker, Philos.Mag.B 43 (1981) 689-703.

[16] Allen, G.C., P.M. Tucker, J.W. Tyler, J. Phys. Chem. 86 (1982) 224-228.

[17] Allen, G.C., P.A. Tempest, Proc. R. Soc. London Ser. A-Math. Phys. Eng. Sci. 406 (1986) 325-344.

[18] Moreno, D., R. Arkush, S. Zalkind, N. Shamir, J. Nuc. Mat. 230 (1996) 181-186.

[19] Arkush, R., A. Venkert, M. Aizenshtein, S. Zalkind, D. Moreno, M. Brill, M.H. Mintz, N. Shamir, J. Alloy. Compd. 244 (1996) 197-205.

[20] Gee, A.T., B.E. Hayden, C. Mormiche, T.S. Nunney, J. Chem. Phys. 112 (2000) 7660-7668.

Chapter 5: The Permeation of Deuterium Through Uranium with Uranium Oxide Overlayers

5.1 Introduction

The corrosion of uranium metal is of great interest to the nuclear industry regarding its safe storage and its performance in a variety of applications. The corrosion reaction is also of environmental concern due to the formation of fine dispersible radioactive particles. The corrosion of uranium metal is slow in dry air, or oxygen, but the rate of reaction increases by more than 10^2 times in the presence of water vapour [1; 2]. In an enclosed environment, this reaction could lead to a build up of free hydrogen gas that can diffuse through the product oxide overlayer to the underlying metal and form the pyrophoric uranium hydride, Reaction 5.1.

$$U_{(s)} + xH_2O_{(g)} \rightarrow UO_{x(s)} + xH_{2(g)} \xrightarrow{U_{(s)}} UH_{3(s)} \qquad \text{Reaction 5.1}$$

The single hydride formed is almost stoichiometric with a hydride-to-metal density ratio of 0.57. The large difference in densities induces strain, cracking and spallation of the hydride such that it is obtained in the form of a powder [3]. Therefore, the hydride reaction front velocity is independent of time, with an apparent activation energy of 30 - 40 $kJmol^{-1}$. The initiation of hydride nuclei at the surface of uranium samples has been extensively studied using hot-stage microscopy (HSM), atomic force microscopy (AFM), scanning electron microscope (SEM) and scanning tunnelling microscopy (STM) [4-7]. Balooch [7] used STM to study flat well-ordered surfaces of uranium, which were created by deposition upon highly ordered pyrolytic graphite (HOPG). The hydriding probability of uranium was found to be extremely low ($\leq 10^{-6}$), even when exposed to high pressures of hydrogen. Arkush *et al* [5] observed the formation of four different "families" of hydride nuclei, differing in nuclei density, size and growth rates. The class of family observed was found to be dependent upon sample preparation and therefore on the thickness of the oxide overlayer, the impurities and the defects present. The smallest

and densest of the families were submicron blisters that formed underneath irregularities in the oxide, caused by mechanical polishing scratches. The second family appeared as larger (1-10μm) blister-like nuclei that developed under the oxide at point defects, but not discontinuities. The growth rate and the final size of the nuclei was found to be controlled by the thickness of the oxide overlayer above the blisters, possibly by the pressure exerted on the hydride beneath. As uranium is transformed to uranium hydride, the volume increases by a factor of 1.8. A third family of fast growing nuclei, developed at the carbide/uranium interface of the carbide inclusion. It was argued that thermal pre-treatment of the sample resulted in the formation of cracks in the oxide overlayer around the carbide/uranium interface because of a difference in the thermal expansion coefficients. These discontinuities in the oxide are easily fractured and lifted and therefore do not inhibit the growth of the hydride. Above a critical oxide thickness, the preferential hydride growth location switched from the carbide/uranium interface to other defects in the oxide, which forms the fourth family. This family consists of fast growing nuclei that were only found on samples with thick oxide overlayers. As the oxide is formed discontinuities, develop due to the mismatch between the metal and the oxide unit cells, which allow hydrogen to pass to the underlying metal. As the hydride nuclei grow, the oxide is easily cracked and lifted and, as a result, the growth of the hydride is uninhibited. These results of the site-related nucleation of uranium hydride give a consistent view that there will always be channels available for hydrogen to attack the underlying metal. The amount of impurities and discontinuities in the oxide overlayer controls the number of nuclei and their growth rate. Hence, for an air-formed oxide overlayer, such as would be found in many technical situations, there would always be a large number of discontinuities present, which provide a low energy pathway for hydrogen to the metal beneath.

Uranium metal has a high affinity for oxygen and will quickly become oxidised. The metal's affinity is so acute that even a sample prepared under UHV conditions will rapidly develop a thin oxide overlayer at room temperature. Ab initio calculations indicate that there is little to no potential energy barrier for the interaction of U and O_2 to form stable UO_2 [8]. Between UO_2 and UO_3 there are 16 known nonstoichiometric oxides [9]. Consequently, it is necessary to understand the influence of the oxide overlayer on the reactivity of the underlying uranium metal.

Swissa *et al* [10] observed a redistribution of the oxide at the metal-oxide interface due to vacuum thermal annealing above 723 K. The authors proposed a process of oxidative diffusion, with oxygen diffusing from the oxide overlayer to the metal–oxide interface. It dissolves in the metal before forming an oxide of lower stoichiometry. The overall diffusion process had Arrhenius behaviour with an activation energy of 64.4 $kJmol^{-1}$ and a pre-exponential factor of $1.1x10^{-8}$ cm^2s^{-1}. Therefore, for the temperature range studied in this chapter (573 – 673 K) the diffusion coefficients of oxygen redistribution into the uranium bulk are in the order of 10^{-14} - 10^{-13} cm^2s^{-1} respectively. Vacuum annealing U-0.1 wt.% Cr alloy samples below 423 K was also shown to have little effect on the oxide layer but an activation effect on the incubation times of hydride formation [11]. This was attributed to the degassing of H_2O or hydroxyl groups from the oxide overlayer. It was proposed that the desorbing species occupied H_2 dissociation sites, which then become available. Using a molecular beam technique, Abrefah *et al* [12] reduced hyperstoichiometric uranium dioxide samples to almost exact uranium dioxide with atomic hydrogen. A sticking probability of 0.7 was calculated for atomic hydrogen chemisorption, with the majority desorbing as molecular hydrogen. A minor reaction channel leading to water desorption was observed, in which the adsorbed hydrogen reacted with interstitial oxygen, thus reducing the stoichiometry of the oxide. Using XPS Wang *et al* [13] followed the reduction of UO_{2+x} to UO_2 through to UO_{2-x} by large exposures of CO, in excess of $1x10^9$ L, at both 293 and 573 K. The U $4f_{7/2}$ peak was found to shift by 0.2 - 0.3 eV to lower binding energies depending on the oxidation state of the metal ion.

A number of workers have studied the solubility and diffusivity of hydrogen, and its isotopes, in uranium dioxide. However, the results vary and are often contradictory. The first of these was by Wheeler [14], who studied the solubility and diffusivity of hydrogen in single crystal UO_2. The crystal was heated in a stream of hydrogen gas before being rapidly cooled and then transferred to a furnace tube, which was under low vacuum. The evolution of gas was measured with the progression of time and from this the hydrogen diffusion coefficient could be evaluated. The data showed rapid hydrogen diffusion with a D_0 value of 0.037 cm^2s^{-1} and an activation energy of approximately 60 $kJmol^{-1}$. Wheeler's solubility data showed low reproducibility between samples, varying from 0.03 to 0.4 μg H_2/g UO_2. It was suggested that the

hydrogen absorbed as molecules, occupying defect sites or vacant interstitial anion sites within the lattice and that the variation in solubility could be accounted for by only very small changes in the stoichiometry of the crystal, from $UO_{1.9998}$ to $UO_{1.99994}$, which was beyond the limits of analysis. The low solubility of hydrogen coupled with a fast diffusion coefficient suggests that the mobility of hydrogen in the oxide is fast between relatively few solubility sites. Aratono *et al* [15] used a thermal-doping technique to calculate the activation energy of tritium diffusion in UO_2 and it was found to be 76 $kJmol^{-1}$, with a D_0 value of 0.15 cm^2s^{-1}. This is comparable to Wheeler's results in spite of the fact that Aratono used a polycrystalline sample, which may suggest that the preferred site for hydrogen to dissolve is within interstitial sites, not grain boundaries. However, this conclusion is not endorsed by the work of Sherman and Orlander [16]. Their work studied the solubility and release kinetics of deuterium at high pressures and temperatures in single crystal and polycrystalline UO_2. They observed well-defined deuterium desorption peaks for all the samples studied that were attributed to a number of differently bound states that desorbed by a "de-trapping" process and whereby each "trap" releases its hydrogen into the bulk from which it rapidly desorbs. For single crystals, the activation energy of deuterium diffusion was found to be substantially higher than that of Wheeler, 235 $kJmol^{-1}$ compared to 60 $kJmol^{-1}$. The solubility of deuterium in single crystal UO_2 was also observed to obey Sievert's law indicating therefore that hydrogen solution in the atomic form rather than molecular. Both the hyperstoichiometric and the nominally stoichiometric polycrystalline UO_2 samples had deuterium solubilities approximately ten times that of the single crystal, whereas the deuterium solubility in the hypostoichiometric oxide was measured at one hundred times that of the single crystal UO_2. The authors explained this difference in solubility as being due to the difference in the number of vacant anion sites that are available for hydrogen dissolution.

In spite of its importance, the permeability of hydrogen through uranium has received little attention. Mallett and Trzeciak [17] investigated both the solubility and diffusion of hydrogen in uranium metal. The solubility of hydrogen was calculated using a manometric technique that involved measuring the amount of gas absorbed by the metal in a system into which a known volume of hydrogen was introduced. The pressure dependence was found to follow Sievert's law, which

states that the solubility of a diatomic gas in a metal is directly proportional to the square root of its pressure. For each of the allotropic forms of uranium, an equation for the solubility of hydrogen was calculated. These values agree reasonably well with the reported values of Davis [18].

(α-phase) $$\log\left(\frac{S}{\sqrt{P}}\right) = -\frac{388}{T} - 0.688$$ Equation 5.1

(β-phase) $$\log\left(\frac{S}{\sqrt{P}}\right) = -\frac{892}{T} + 0.408$$ Equation 5.2

(γ-phase) $$\log\left(\frac{S}{\sqrt{P}}\right) = -\frac{227}{T} - 0.052$$ Equation 5.3

where S is the solubility in ppm, P is the pressure of gas in mmHg and the T is in K. The limiting value for the pressure in Equations 5.1 – 5.3 was the variation of the dissociation pressure of uranium hydride with temperature, Equation 5.4.

$$\log P = -\frac{4590}{T} + 9.39$$ Equation 5.4

The pressures and temperatures chosen for the experimental studies reported in Section 5.4 were chosen such that there was no possibility of uranium hydride formation, i.e. the chosen pressure was always significantly lower than the dissociation pressures determined from Equation 5.4. The diffusion coefficients for hydrogen diffusion in uranium were investigated by Mallett and Trezeciak using degassing rate data and were fitted to an Arrhenius type equation:

$$D = D_0 \exp\left(-\frac{E_D}{RT}\right)$$ Equation 5.5

where, D_0 was 1.95×10^{-2} cm^2s^{-1} and the activation energy (E_D) was calculated to be 46.33 $kJmol^{-1}$. The validity of this result was brought into question by Davis, who determined the hydrogen diffusion coefficients by both diffusion out of spherical samples and through metal membranes [18]. In both cases, it was noted that surface

cleanliness had a significant effect on diffusion, with high levels of contamination causing a significant reduction in the observed values. The activation energy of hydrogen diffusion was calculated as 26.01 $kJmol^{-1}$, with a D_0 value of $1.4x10^{-3}$, which is significantly lower than that calculated by Mallett. There is good agreement between the diffusion coefficients of the two authors at 873 K, but at lower temperature those predicted by Davis are significantly higher. This is probably due to Davis's experiments being unaffected by surface contributions. There was also the possibility of hydride formation during the degassing experiments of Mallett. Both of theses factors would be of more significance at lower temperatures. It was for these reasons that Powell and Condon [19] considered the results of Davis to be a good representation of interstitial hydrogen mobility in α-phase uranium. They also suggested that the observed diffusion coefficients might depend on the metallurgical history of the metal, resulting from differences in the defect structure and crystallographic orientation. Dislocations in the metal can provide effective transport pathways, due to their high affinity for interstitial hydrogen.

It seems clear from the above that there is great uncertainty as to the nature and extent of hydrogen transport through UO_2 (single crystal or polycrystalline). However, published data relating to the permeation of hydrogen through uranium metal is more consistent. Therefore, it was thought that a greater understanding of hydrogen transport through UO_2 might be obtained by studying the permeation of hydrogen through uranium membranes bearing varying degrees of oxide thickness. The effect of the oxide overlayer on the temperature and pressure dependence of deuterium diffusion was also studied.

5.2 Experimental

All the experiments reported in this chapter were carried out in a purpose built UHV system, discussed in more detail in Section 2.2. The system was designed to have direct line of sight from the front face of the sample to the detector of a pulse counting QMS (VG). Between the sample and the QMS chamber was a 3 mm collimating aperture, which improved the signal to noise ratio.

The samples used in these experiments were of two different metal thicknesses. The first samples, denoted Set A, were 1 mm thick depleted uranium disks, provided by AWE plc. The other samples were 0.178 mm thick natural uranium disks, provided by Goodfellow. In all cases, the samples were 12 mm in diameter. The uranium samples were mounted in a sample holder constructed from specially modified Cajon® fittings and attached to the base of a standard xyzθ-shift manipulator. The sample was slowly heated over several hours to ensure that both the sample and the sample holder had equilibrated at the desired temperature prior to any gas permeation experiment. The required pressure of deuterium (99.7%, Messer) was quickly established by a series of valves and measured by a Baratron gauge with a 1 – 1000 mbar range. The heating was continued for several hours after the completion of each experiment to remove any residual gas from the sample. Cooling the sample before all dissolved hydrogen had been outgassed would have resulted in UH_3 being precipitated within the sample.

The 0.178 mm thick samples were split into three Sets. The first, Set B, were left exposed to air and no cleaning or sample preparation was carried out on them, apart from that performed by the manufacturing before delivery. The inlet surface of Set C was coated with approximately 200 nm of palladium using MBE at 373 K. Prior to deposition, the sample was cleaned using a nitric acid solution, see Section 2.2.3 for the experimental procedure. The third, Set D, was pre-cleaned using the nitric acid cleaning procedure prior to insertion into the UHV system.

5.3 Models of the Uranium/Uranium Oxide System

One of the main aims of this work was to investigate the effect of the oxide overlayer on the permeation of deuterium through uranium. Unfortunately, the UHV system used was not equipped with any surface analysis techniques, nor were any external analysis techniques used to quantify the oxide present on each of the samples. Thus, a number of possible models of the uranium/uranium oxide system under investigation have been produced in an attempt to explain the observed permeation data. For each of the models, a number of predictions may be made for the expected behaviour of deuterium permeation.

In order to make these predictions, the permeability of hydrogen through both uranium and uranium oxide need to be considered. The literature concerning this is scarce with only a few studies having been performed using either the metal or the oxide [14; 15; 17; 18]. These results are summarised in Table 5.1:

	U/UO_2	**D_0 / cm^2s^{-1}**	**E_D / $kJmol^{-1}$**	**D / cm^2s^{-1} @ 623 K**	**Reaction Gas**
Mallett and Trzeciak [17]	$U_{(metal)}$	$1.95x10^{-2}$	46.33	$2.53x10^{-6}$	H_2
Davis [18]	$U_{(metal)}$	$1.4x10^{-3}$	26.01	$7.96x10^{-6}$	H_2
Wheeler [14]	UO_2	$3.7x10^{-2}$	59.83	$3.56x10^{-7}$	H_2
Aratono [15]	UO_2	$1.5x10^{-1}$	76	$6.36x10^{-8}$	T_2

Table 5.1 – Summary of the D_0 and E_D values calculated from the literature, with an example of the associated diffusion coefficients at 623 K.

As we discussed in Section 5.1, there have been doubts raised concerning the validity of the results of Mallett [17; 19]. Also, the results of Aratono [15] have been included as additional evidence of the small diffusion coefficients of hydrogen isotopes through uranium dioxide and the associated high activation energies. Therefore, for the purpose of these models, the results of Davis [18] will be taken as a proper representation of the behaviour of hydrogen in uranium metal and the results of Wheeler [14] as indicative of the oxide. A comparison of the respective

diffusion coefficients at 623 K indicates that hydrogen diffusion through uranium metal is greater than an order of magnitude higher than diffusion through the oxide.

T_s = 623 K	U/UO_2	Reaction Gas	Estimated Time Lag / s		
			1 mm	0.178 mm	2x10^{-3} mm
Davis [18]	$U_{(metal)}$	H_2	209	6.73	N/a
Wheeler [14]	UO_2	H_2	N/a	N/a	0.02

Table 5.2 – Estimation of the time lags for the two metal membranes and a possible oxide thickness calculated from the published diffusion coefficients of the metal and the oxide, with T_s = 623 K.

The significance of the difference in the diffusion coefficients becomes more apparent when Equation 3.44 is used to estimate the time lags for the two metal membranes thickness used in this study, Table 5.2. Also included is a possible oxide overlayer thickness of a few micrometers, above this thickness and the oxide begins to flake off [20]. Thus, assuming that the reported diffusion coefficient data of Davis and Wheeler are accurate then it is expected that the metal membrane will dominate the observed values of the diffusion coefficient regardless of the oxide overlayer present. Also, Balooch observed that grain boundaries in the oxide overlayer were the preferred site for hydrogen attack on the metal surface [21]. Thus, oxide defects will provide channels through which hydrogen can travel to the underlying metal surface. This was also substantiated by the earlier results presented in Chapter 4.

In order to establish any contribution to the overall permeation kinetics resulting from the interface between the uranium metal and the vacuum, as a result of the presence of an oxide overlayer, we must ascertain the relationship between the inlet pressure (P_{inlet}) and the steady-state flux (J). If we consider the passage of a diatomic molecule though a clean metal surface, the reactions at the boundaries can be considered to be very fast, in comparison to the diffusion process through the bulk. Then one expects the steady-state flux to be given by Sievert's law:

$$J \propto P_{inlet}^{1/2} \qquad \text{Equation 5.6}$$

If the overall diffusion process is limited by the surface, then one may expect:

$$J \propto P_{inlet} \qquad \text{Equation 5.7}$$

In the case of hydrogen permeation through a number of other metals (Fe , Ni and Pd [22]), the steady-state flux has conformed to that expected from Sievert's law, with a plot of log (J) against log (P_{inlet}) yielding a straight line with a gradient of approximately 0.5. Yamakawa *et al* observed deviations from half-power dependence for hydrogen permeation through a Pd membrane [22; 23]. The exponent of Equation 5.6 was found to be 1.1 for an "as received" sample, which was reduced to approximately 0.5 by annealing the sample in air to remove surface contaminants. Using Auger electron spectroscopy (AES), carbon was found to be the major surface contamination and this was likely to have been removed as CO_2 during annealing in air. Therefore, it was postulated that it was the contamination by surface carbon atoms that was responsible for supressing the permeation of hydrogen through palladium.

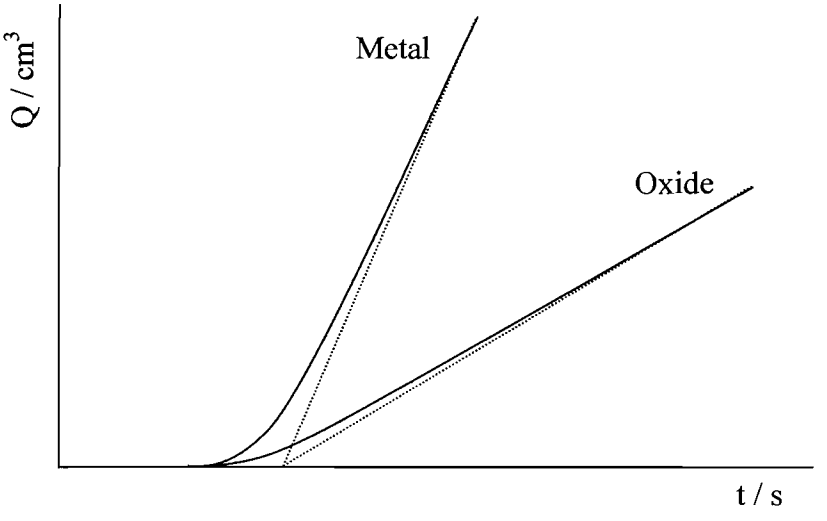

Figure 5.1 – Q vs. t graph showing the predicted relationship between the clean metal and an oxide-coated metal.

The pressure dependence of hydrogen permeating through metals with oxide overlayers has also been studied by Strehlow and Savage [24]. The presence of a near-complete oxide overlayer was shown to exhibit nearly first-power pressure

dependence at low pressures and a square-root dependence at high pressures, where the metal was limiting. At very low pressures, the presence of defects in the oxide was thought to limit the permeation and this exhibited a second region of square-root dependence. Intermediate pressure dependences with exponent values between 1 and 0.5 were attributed to the presence of an oxide overlayer that was defective and not too thick, thus providing parallel channels for permeation through the oxide.

Both Yamakawa and Strehlow observed significant reductions in the flux of permeating gas when the inlet pressure dependence was found to be greater than half-power. Up to a thousand-fold reduction in the permeation rate was observed by the introduction of an oxide overlayer onto a metal membrane [24]. Figure 5.1 shows a graphical representation of the expected total desorbing flux (Q) against time (t) for the clean metal (metal) and an oxide-coated metal membrane (oxide). Transitional curves would be expected for intermediate inlet pressure dependences, such as would be expected for defective oxide coverage. Therefore, at a given inlet pressure range, the observed desorption flux will be dependent upon the level of surface contamination and the characteristics of the oxide overlayer present.

From these observations, one can now propose some models in an attempt to identify the type of uranium/uranium oxide system under investigation. Schematics of the three models are shown above in Figure 5.2.

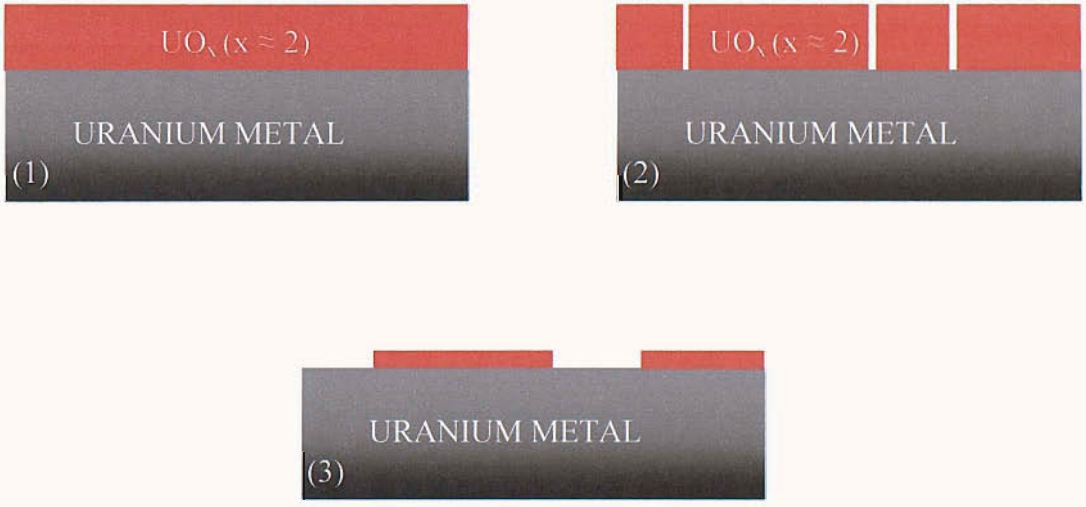

Figure 5.2 – Schematics of the models used to predict the behaviour of the uranium/uranium oxide system. (1) – Complete oxide overlayer. (2) – Defective oxide overlayer present. (3) – Thin oxide with areas of bare metal exposed.

Model (1) shows the uranium metal completely covered by an oxide overlayer that is defect free and continuous across the surface. The inlet pressure dependence of the permeation flux would be expected to be approximately first power and the equilibrium flux of desorbing molecules would be expected to be relatively low.

The oxide overlayer of Model (2) has grain boundaries and other line defects present, which will provide low-energy pathways to the underlying metal. The inlet pressure dependence of the permeation flux would be expected to be in the range 0.5 to 1 depending on the degree of influence that the oxide has upon the permeation process. The flux of desorbing molecules would be expected to be higher than for Model (1) but still significantly lower than for the case of a clean metal membrane because there will be a lowering of the effective surface area.

Model (3) has only a thin layer of oxide present and it is assumed that there are large areas of metal exposed. Therefore, the inlet pressure dependence of the permeation flux would be expected to be approximately half-power, with the highest permeation flux of all the models. The presence of a small amount of oxide has been included in this model because of the severe technical difficulties in removing all traces of the oxide from uranium samples, even under UHV conditions, as experienced in Chapter 4. This is therefore considered to be a better representation of a "clean" sample.

Model	Expected Inlet Pressure Dependence	Steady-State Flux
1	~1	Low
↑ 2	$0.5 < n < 1$	
3	~0.5	High

Table 5.3 – Summary of the expected inlet pressure dependence and relative level of the permeation flux for each of the models.

Table 5.3 contains a summary of the permeation flux characteristics for each of the above models, as predicted from the observations of Yamakawa and Savage. It should be noted that only one surface is shown for each of the models in Figure 5.2; however, when the oxide dominates the overall permeation flux then both surfaces would have to be considered. In all cases, it has been assumed that the diffusion coefficient, and hence the time lag, that is expected to be observed will be related to diffusion through the metal membrane. Also, it has been assumed that the surface processes, dissociation (dissociative adsorption) and desorption, are very fast in comparison to the overall permeation process, see Chapter 4.

5.4 Results and Discussion

5.4.1 Inlet Pressure Dependence

Figure 5.3 shows that at 623, 653 and 673 K there is a linear relationship between log (J) and log (P_{inlet}) for sample Set A. The gradients of the best-fit lines to the data were 0.67, 0.67 and 0.65 ± 0.03 respectively. The data were collected from two different uranium samples, labelled A1 and A2. The data at 623 and 653 K were collected from sample A2, while the data at 673 K were collected from sample A1. It can clearly be seen that there is excellent agreement between the pressure dependence of the steady-state flux for the two samples. Both samples were polished with 1 μm diamond paste prior to delivery, but were completely covered in an air formed oxide that had developed over the several months of storage preceding their introduction into the UHV system. Sample A1 was contained within the UHV system for approximately two months before the data presented was collected. During this time no specific surface cleaning was carried out but the sample was periodically heated (573 – 673 K) and exposed to helium, to test for leaks within the sample mounting. Sample A2 was under vacuum for approximately five days before permeation experiments were performed, during which time no surface cleaning was performed.

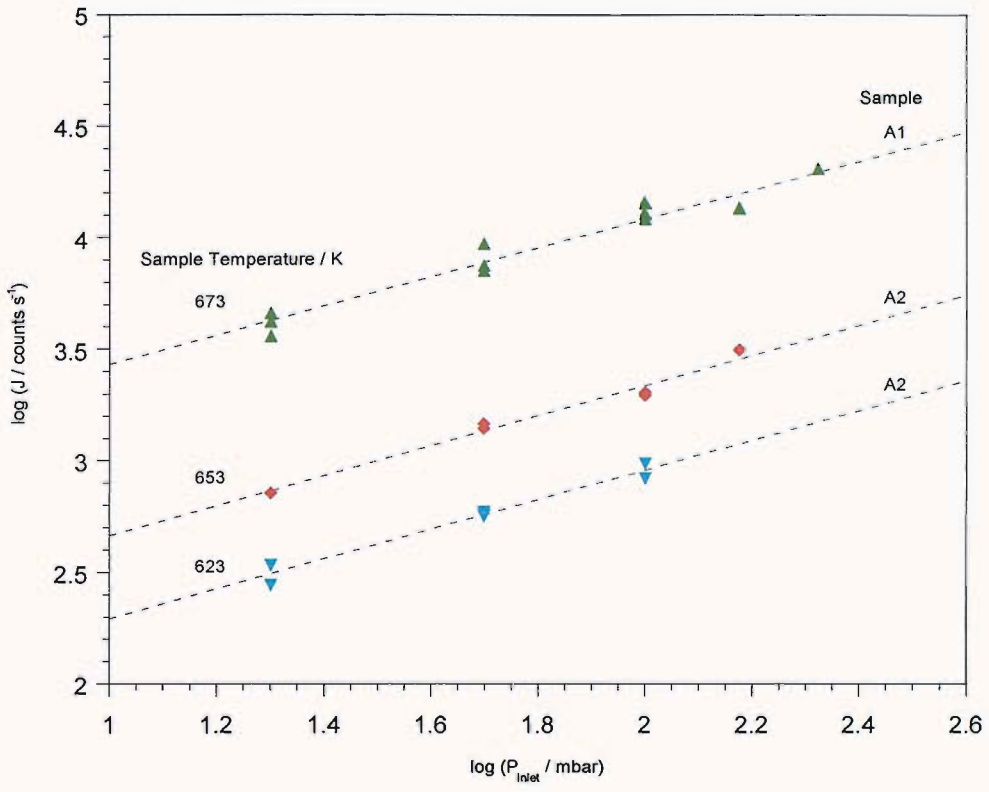

Figure 5.3 - Log-log plot of the relationship between the steady-state flux of desorbing molecules and the initial gas pressure, at 623 (▼), 653 (♦) and 673 (▲) K for samples A1 and A2 of Set A.

Figure 5.4 shows the linear log (J) versus log (P_{inlet}) relationship for sample Set B at 598 and 648 K. The gradients of the best-fit lines are 0.67 and 0.68 ± 0.02 respectively. The data for both temperatures were collected from two samples, labelled B1 and B2. Both samples were covered in an air-formed oxide overlayer that was produced during their time in storage and they were under vacuum for only a few days before experiments commenced. During this time, no surface cleaning was performed.

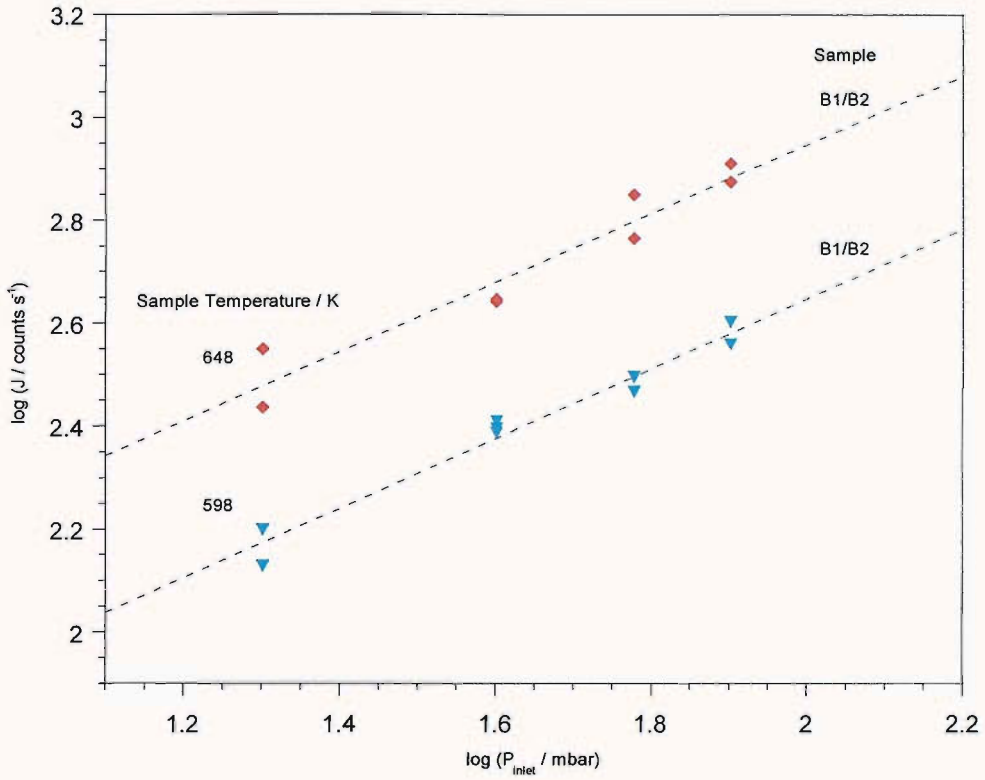

Figure 5.4 - Log-log plot of the relationship between the steady-state flux of desorbing molecules and the initial gas pressure at 598 (♦) and 648 (▼) K for samples B1 and B2 of Set B.

Set	Sample Thickness / mm	Sample Temperature / K	Sievert's Exponent	Error
A	1	623	0.67	± 0.03
	1	653	0.67	± 0.03
	1	673	0.65	± 0.03
B	0.178	598	0.67	± 0.02
	0.178	648	0.68	± 0.02

Table 5.4 - Summary of the calculated inlet pressure dependence of the steady-state flux for Sets A and B at various sample temperatures.

Table 5.4 shows a summary of the calculated inlet pressure dependence of the steady-state flux for Sets A and B at a range of sample temperatures. From this it can be seen that both sample thickness used in this study show good agreement for the inlet pressure dependence of the steady-state permeation flux in the applied temperature range. The 0.65 – 0.68 exponents observed indicate that the interfacial

transport processes of deuterium, i.e. the adsorption/desorption processes, are being slightly influenced by the presence of an oxide overlayer, or surface contaminants.

In all cases, for both samples sets, on removal from the UHV system it was noted that the exit surface (exposed to UHV) was shiny and metallic in appearance. In the absence of any cleaning procedures, the removal of the surface oxide from the outlet surface is assumed to occur by a diffusion-like process, whereby the oxygen is redistributed in the subsurface region [10]. In contrast, a thick brittle oxide overlayer had formed on the inlet surface of the samples. As the growth of the oxide proceeds, the significant mismatch between the crystal structures of the metal and the oxide destabilises the growth mode of the oxide, which leads to the formation of cracks and other discontinuities. All the samples used for the permeation studies were polycrystalline. Therefore, it would not be unreasonable to expect that there would have been a significant number of defects present in the oxide overlayers. Ultimately, this mismatch leads to the formation of a critical oxide thickness, above which the oxide will crack and flake off [20].

From Figures 5.3 and 5.4 it can be seen that, as expected, the steady-state permeation fluxes of Sets A and B both increase with increasing sample temperature, at a given inlet pressure. However, a comparison of the relative steady-state fluxes of Sets A and B shows that at a comparable sample temperature and at any given inlet pressure, the steady-state flux of Set A is considerably higher than that of Set B. This is not expected from two samples of the stated thickness, with similar surface conditions, because from Equation 3.43 the steady-state flux would be expected to be inversely proportional to the sample thickness [25]. Thus, it would be expected that the steady-state flux of Set A would be approximately five times lower than that expected for Set B. This suggests that the oxide overlayer is dominating the magnitude of the steady-state flux, and not the thickness of the metal membrane. One possible explanation for this is that there is a difference in the effective surface area between sample sets. This is highly probable considering that the oxide overlayers were air-formed and therefore there had been no attempt to control the oxide growth process. Also, differences in the metallurgical history of the two samples could possibly lead to differences in the number of defects present in the oxide overlayer.

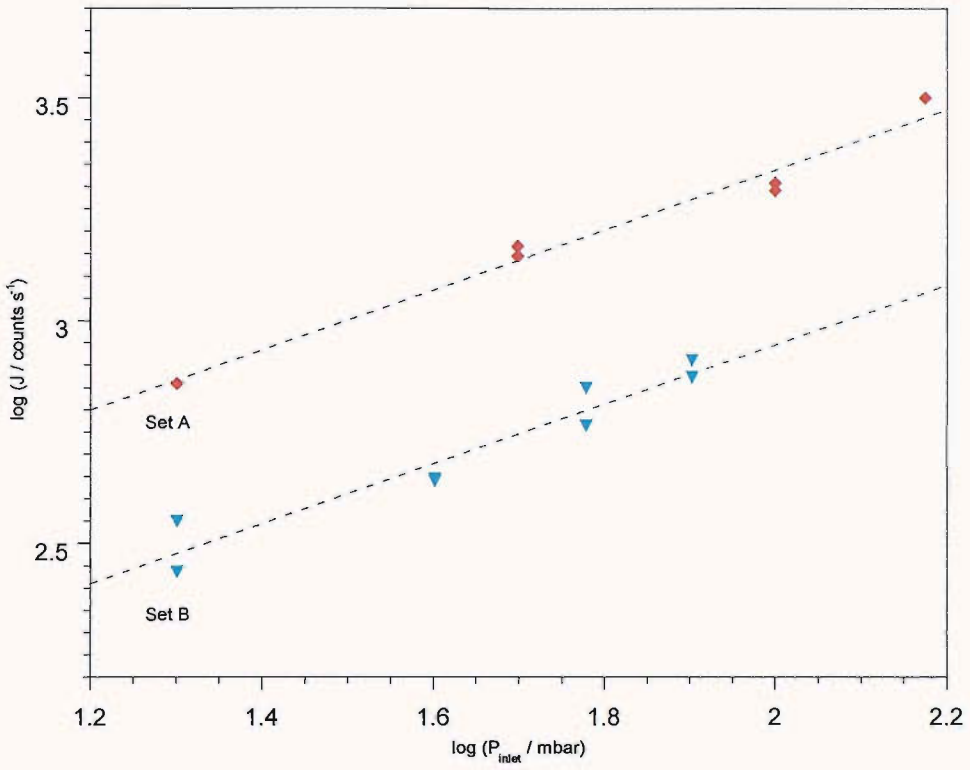

Figure 5.5 - Log-log plot comparing the relative steady-state flux of desorbing molecules for Set A and Set B, at 653 and 648 K respectively.

In order to further investigate the effect of the oxide overlayer and surface contamination upon the steady-state permeation flux, Set D was cleaned using a concentrated nitric acid solution prior to its introduction into the UHV system, see Section 2.2.3 for more details. Figure 5.6 shows the log (J) versus log (P_{inlet}) relationship for Set B and Set D, at 648 K and at 635 K respectively. Unfortunately, there were no surface analysis techniques available to establish the effectiveness of the sample cleaning procedure. However, the gradient of the best-fit line for Set D was calculated as 0.60 ± 0.02 (compared to 065 – 0.68 for Sets A and B), which is concomitant with a significant shift towards a more metallic surface and also a significant decrease in the amount of surface contaminants present. It is therefore expected that additional cleaning would further reduce the gradient to the half-power dependence associated with a diffusion mediated process through a clean metal. It should also be noted that there was a 30 minute delay between finishing the cleaning process and installing the sample in the UHV system, due to the technicallities of sample mounting. During this time, it is highly probable that a thin oxide overlayer

would have become restablished, decreasing the apparent effectivness of the cleaning process.

It can be seen that the cleaning procedure has had little effect upon the relative steady-state permeation flux for the two Sets. The slightly higher flux values for Set B compared to those of Set D can be related, at least in part, to the slightly higher surface temperature of the former samples. The comparable steady-state flux values and the decrease in the inlet pressure dependence exponent suggests that the nitric acid cleaning procedure decreased the thickness of the oxide overlayer, or the level of contamination, without changing the overall effective suface area of metal readily accessible via the presence of defects in the oxide overlayer.

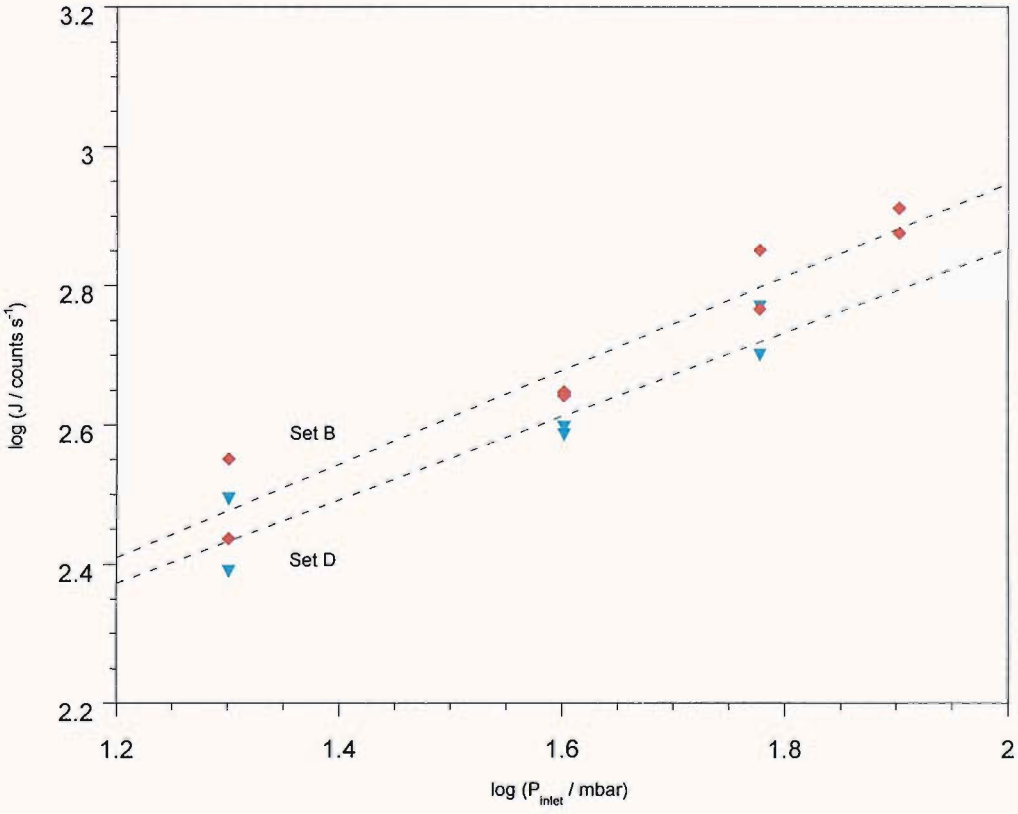

Figure 5.6 - Log-log plot of the relationship between the steady-state flux of desorbing molecules and the initial gas pressure for Set B (♦) and Set D (▼), at 648 and 635 K respectively.

From these results a number of conclusions can be made concerning which proposed model from Section 5.3 is appropriate for Sets A, B and D. All three Sets showed intermediary inlet pressure dependences of the steady-state permeation flux. This

indicates that neither the complete oxide overlayer of Model (1) or the "clean" uranium of Model (3) would be appropriate for these samples. Therefore, the defective oxide overlayer model of Model (2) can be applied to Sets A, B and D. However, from this data we can see that the oxide overlayer is not consistent between Sets, with probable variations in the number, and type, of defects present and also in the oxide thickness.

5.4.2 Deuterium Diffusion Coefficients

The diffusion coefficients were calculated using the membrane Time Lag method discussed in Section 3.5. Unless stated, the sample thickness used in these calculations was that of the overall metal membrane, Set A was 1 mm and Sets B, C and D were 0.178 mm thick. This assumes that the thickness of the metal membrane is controlling the diffusion process. The validity of this assumption will be addressed later in this section. All the permeation experiments were carried out using the method detailed in Section 5.2.

5.4.2.1 Palladium Coated Uranium Surface

A thin film of palladium was deposited onto the inlet surface of a uranium sample (Set C) and mounted in the UHV permeation system. Prior to deposition, the sample was cleaned using a concentrated nitric acid solution, detailed in Section 2.2.3. Palladium was chosen for deposition as it has been used in previous studies as a protective layer against oxidation [26; 27] and because it has a low activation energy for hydrogen permeation (13.89 $kJmol^{-1}$ [22]), compared to that of the uranium metal (63.77 $kJmol^{-1}$ [18]). Therefore, it is not expected to hinder the overall permeation process. Unfortunately, the samples instability precluded any pressure dependence measurements from being made. Therefore, it is not known if, as expected, the half-power pressure dependence would have been experienced by this sample.

Figure 5.7 shows an Arrhenius plot for the deuterium diffusion coefficients of Set C, with an inlet pressure of 20 mbar, compared with the published data for hydrogen diffusion through uranium metal [17; 18]. Only a small number of experiments were conducted using Set C before a technical problem halted experiments. These points had substantial errors associated with them due to experimental problems with dealing with such short time lags, shown in Figure 5.7. However, from these few points, a tentative equation for the diffusion coefficients can be estimated:

$$D = 3.26x10^{-3} \exp\left(-\frac{35.39kJmol^{-1}}{RT}\right) \qquad \text{Equation 5.8}$$

The apparent activation energy of deuterium diffusion through a palladium coated uranium sample was estimated to be 35.39 ± 11.61 $kJmol^{-1}$, with a D_0 value of $3.26x10^{-3} \pm 1.07x10^{-3}$ cm^2s^{-1}. The slight deviation of the diffusion coefficients for Set C compared to previous results for the metal may be the result of an isotope effect. From simple kinetic theory [28], the diffusion coefficient of a perfect gas is proportional to the mean free path length (λ) and the mean speed ($\bar{c}$) of the diffusing particles:

$$D = \frac{1}{3}\lambda\bar{c} \qquad \text{Equation 5.9}$$

Where,

$$\bar{c} = \left(\frac{8RT}{\pi M}\right)^{\frac{1}{2}} \qquad \text{Equation 5.10}$$

Thus, the diffusion coefficient would be expected to be inversely proportional to the square root of the particles mass, giving for the ratio D_H/D_D a value of $\sqrt{2}$ [29; 30]. Using this isotope ratio, the calculated hydrogen diffusion coefficients of Davis and Mallett can be used to estimate the relevant deuterium diffusion coefficients, Davis (D_2) and Mallett (D_2) respectively in Figure 5.7. From this it can be seen that

the results of Set C are in better agreement with those of Davis than Mallett, which adds further weight to the arguments of Davis.

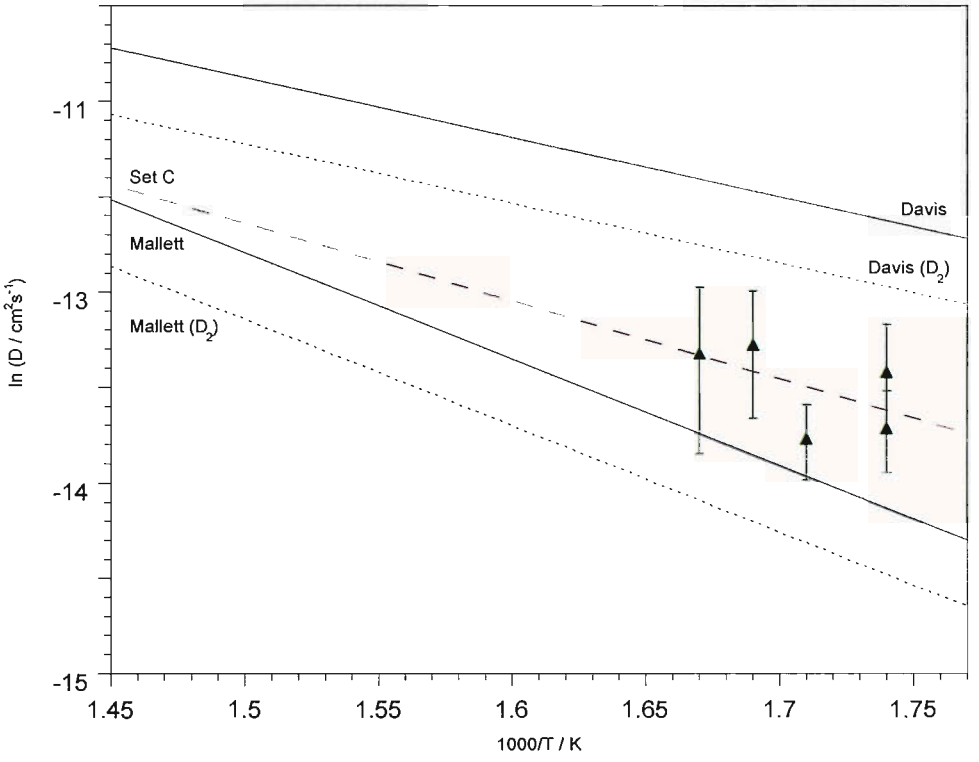

Figure 5.7 – Arrhenius plot of the palladium coated Set C, with an inlet pressure of 20 mbar. Also shown are the Arrhenius plots of hydrogen diffusion through U_{metal} from Davis and Mallett, with predicted plots for D_2 diffusion calculated from the isotope effect.

Figure 5.8 shows comparable permeation flux - time traces for each of the sample Sets studied, at an inlet pressure of 20 mbar. As discussed in the previous Section the difference in the relative steady-state fluxes between Set A and Sets B and D cannot be explained by differences in the metal membrane thickness, but more probably to differences in the influence, thickness and microstructure of the oxide overlayer. It is also evident from Figure 5.8 that the associated time lags vary between Sets; however, this will be discussed in more detail in Section 5.4.2.2. Immediately apparent is the vast increase in the steady-state flux of the palladium coated Set C. This flux was approximately 30 times higher than that of Sets B and D. The short time required to achieve a steady-state flux using Set C brought concerns about the possibility of a leak being present within the sample mounting; however, the slow decay after the gas-dosing line had been evacuated was indicative of a permeation process taking place. A leak would have manifested itself as an

almost instantaneous decline in the amount of gas detected back to the background level. This high steady-state flux is concomitant with a metal limited permeation process [24]. The steady-state permeation flux itself may not be the maximum possible for a completely clean sample, due to the nitric acid cleaning procedure not being completely comprehensive in removing the oxide overlayer before palladium was deposited.

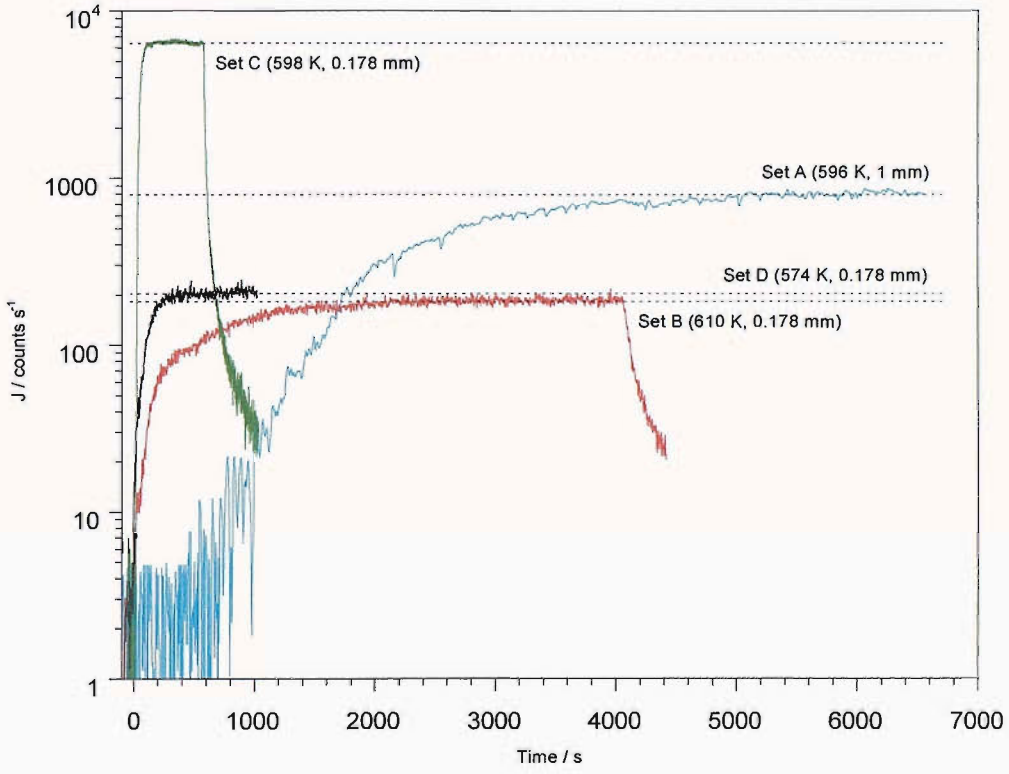

Figure 5.8 – Pressure-time traces for each of the sample Sets studied, at comparable surface temperatures with an inlet pressure of 20 mbar.

From these few results, we can predict a model for the palladium/uranium system under investigation, which is shown pictorially in Figure 5.9. There is expected to be a small amount of oxide present on the surface, which lowers the effective surface area and hence the steady-state permeation flux observed. The palladium film is continuous across the surface and inhibits the growth of any oxide that remains on the uranium surface. The palladium film is approximately 200 nm thick, which coupled with its low activation energy for hydrogen diffusion, specifies that the permeation of deuterium through this film will be very fast. Therefore, it is likely that the palladium film can act as a rich source of deuterium atoms. These atoms would quickly saturate the inlet surface of the sample, ensuring that the

surface processes are fast, and therefore negligible, in comparison to the diffusion process. Hence, it is diffusion through the metal that dominates the overall permeation process. The behavioural characteristics of this model will be expected to be the same as those of Model (3), defined in Section 5.3. We were not able to establish the inlet pressure dependence of the permeation process, due to the instability of the sample. However, the observed diffusion coefficients are in good agreement with the estimated deuterium diffusion coefficients of Davis, using the isotope ratio. Finally, the steady-state flux of Set C was significantly higher than the fluxes for Sets A, B and C, under similar experimental conditions. Therefore, Set C displays many of the characteristics associated with this model, enabling us to confidently predict that the deposition of a thin film of palladium onto a pre-cleaned sample allowed us to observe deuterium permeation through uranium without the interference from oxide overlayers.

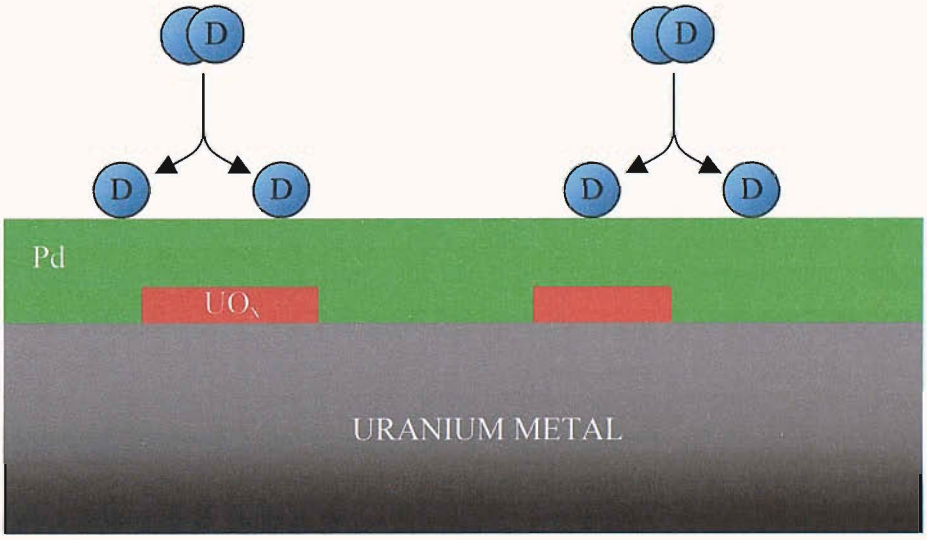

Figure 5.9 – Model of the palladium/uranium system of Set C. A small amount of UO_x may remain on the surface due to the difficulty in completely removing it.

Figure 5.10 shows the Arrhenius plots of Sets A, B, C and D, at an inlet pressure of 20 mbar. Also shown are the Arrhenius plots for hydrogen diffusion through uranium metal [18] and the predicted deuterium diffusion, using the isotope ratio discussed in the previous section. The associated Arrhenius equations are summarised in Table 5.5.

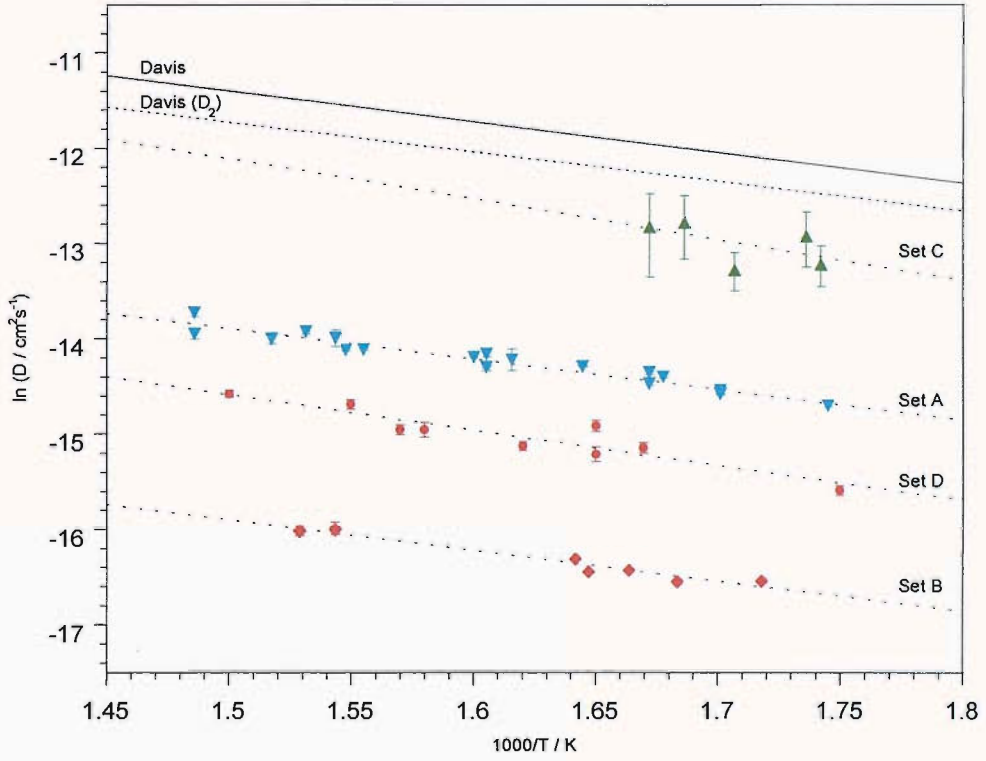

Figure 5.10 – Arrhenius plots of Sets A, B, C and D, at an inlet pressure of 20 mbar. Also shown are the Arrhenius plots of hydrogen and deuterium diffusion through uranium metal, using the results of Davis [17].

Set	Inlet Pressure / mbar	D_0 / cm^2s^{-1}	± Error / cm^2s^{-1}	E_D / $kJmol^{-1}$	± Error / $kJmol^{-1}$
A	20	1.12×10^{-4}	1.68×10^{-5}	26.60	4.00
B	20	1.50×10^{-5}	8.47×10^{-7}	26.56	1.50
C	20	3.26×10^{-3}	1.07×10^{-3}	35.39	11.61
D	20	1.15×10^{-4}	9.07×10^{-6}	30.56	2.41
Davis (H_2)	n/k	1.40×10^{-3}	n/k	26.01	n/k

Table 5.5 – Summary of the D_0 and E_D values for Sets A, B, C and D. Also, included are the values for hydrogen diffusion through uranium metal [17].

Immediately apparent from this data is the fact that there is no agreement between the diffusion coefficients observed for any of the sample Sets. The diffusion coefficients were calculated using Equation 3.45. This equation contained two variables, the time lag (L) and the membrane thickness (l). The time lag was calculated directly from the experimental observations; it is therefore highly improbable that the substantial variations in times necessary for the sample sets to all agree would have been due to an error within these calculations. For example, a thirty-fold decrease in the observed time lags of Set B would be necessary for there to be agreement with the diffusion coefficients of Set C, which we have assumed to be indicative of deuterium diffusion through uranium metal. A further source for error is the value of the assumed membrane thickness, initially taken as the metal membrane thickness. However, Table 5.6 shows the increase in membrane thickness necessary for the calculated diffusion coefficients to agree with Set C. If diffusion through the uranium metal had been the dominant factor, then it is expected that the observed diffusion coefficients of Sets A, B and D would be in good agreement with the values of Set C. This is obviously not the case with the necessary membrane thickness increases ranging from 110 to over 500 %, which are completely unfeasible. Therefore, we must consider the possibility that the presence of an oxide overlayer is in some way influencing the observed diffusion coefficients.

Set	Membrane Thickness / mm	Thickness Increase / mm	% Increase
A	1	1.1	110
B	0.178	0.9	506
D	0.178	0.4	225

Table 5.6 – Summary of the increase in membrane thickness necessary for the diffusion coefficients to agree with Set C.

Sets B, C and D were all 0.178 mm thick samples but with varying degrees of oxide overlayer thickness; Set B was covered in an air-formed oxide, Set C was pre-cleaned with nitric acid before a palladium film was deposited onto one surface and Set D was partially cleaned using nitric acid. From Figure 5.10 it can be seen that

the observed diffusion coefficients for these Sets appears to increase with decreasing oxide thickness.

Also, it is expected that the diffusion coefficients of Sets A and B would be comparable, due to the similar oxide preparation, detailed in Section 5.4.1. However, the observed diffusion coefficients for Set A are ten times higher than that of Set B. One possible explanation for this observation is that although the oxide overlayer present on both membranes would have been comparable there is a significant difference in the thickness of the uranium membranes, 0.1 and 0.178 mm for Sets A and B respectively. Therefore, as the membrane thickness decreases there is an increase in the contribution, and hence the influence, of the oxide to the total membrane thickness.

The apparent activation energy for deuterium diffusion calculated for all of the Sets were in good agreement (~27 – 35 $kJmol^{-1}$), although it should be noted that the errors associated with Set C are significantly large, due to the limited number of data points. The values calculated are comparable to the reported data of Davis (~26 $kJmol^{-1}$ [18]), which, assuming that this result is itself correct, implies that the activation energy being measured corresponds to diffusion through the uranium metal membrane. From the results of Wheeler and Aratono it can be seen that the activation energy of diffusion through uranium dioxide is significantly higher (~60 – 76 $kJmol^{-1}$ [14; 15]) than that through the metal. Therefore, if deuterium was initially diffusing through the oxide lattice sites then the calculated activation energy for Sets A, B and D should reflect this higher activation energy. However, this is not the case, which suggests that diffusion through the oxide occurs via low-energy pathways, such as through grain-boundaries or line defects.

One possible low-energy pathway is Knudsen flow down a pore in the oxide overlayer. The diffusion coefficients associated with Knudsen flow can be calculated using:

$$D_K = \frac{2}{3} r \left(\frac{8RT}{\pi M} \right)^{\frac{1}{2}} \qquad \text{Equation 5.11}$$

where r is the radius of the pore and M is the molecular mass of the diffusing species. The temperature dependence of the Knudsen diffusion coefficients leads to an apparent activation energy of diffusion of approximately 2.58 $kJmol^{-1}$, which is independent of the pore radius and the molecular mass. This low activation energy is consistent with the above results. However, for the Knudsen diffusion coefficients to be significantly small that it will hinder the overall diffusion process, the pore radius would need to be approximately 10^{-16} m (this value was calculated assuming an oxide overlayer of approximately 2 μm and a metal membrane of 0.178 mm), which is smaller then the diameter of hydrogen atoms (~53 pm). Therefore, it is unlikely that Knudsen flow down pores in the oxide has any significant effect on the diffusion process.

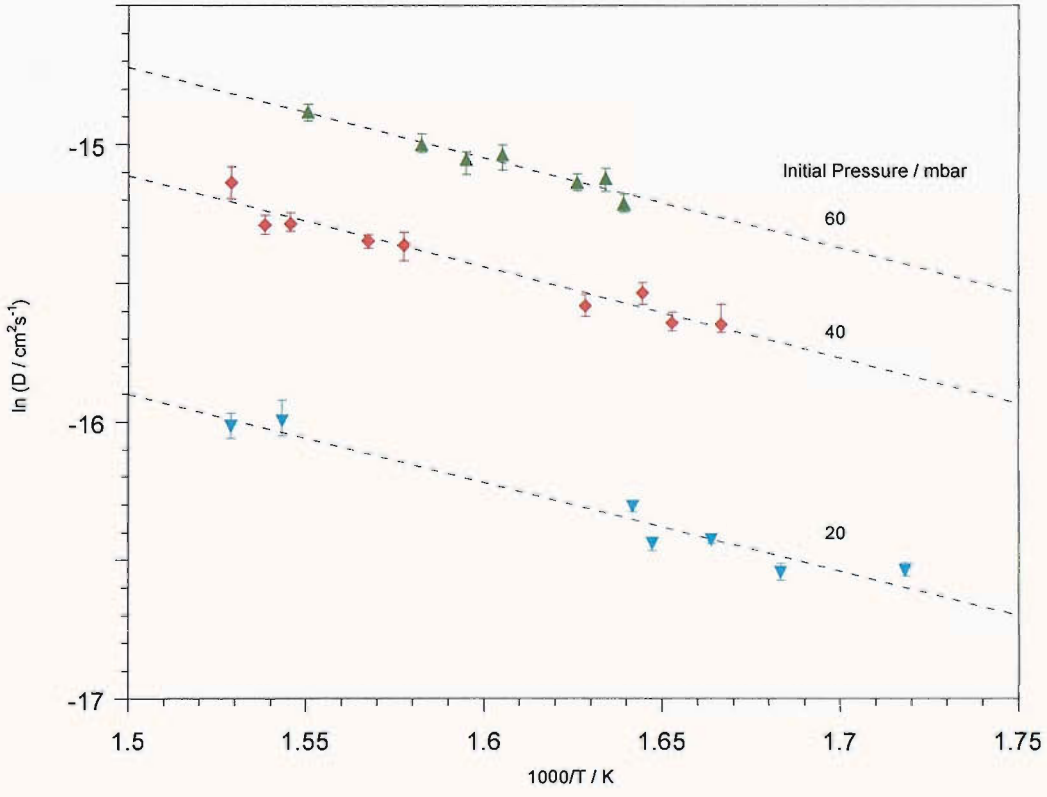

Figure 5.11 – Arrhenius plots for Set B at 20 (▼), 40 (♦) and 60 (▲) mbar inlet pressures.

Another possible diffusion pathway through the oxide overlayer is down grain boundaries or line defects and this transport pathway might explain some of the anomalous observed diffusion data (specifically the apparent variation of the

diffusion coefficient with inlet pressure). For example, hydrogen diffusion through nickel was found to be highly dependent on the microstructure of the samples [31; 32] with large permeation fluxes being observed for samples with small grain sizes due to the contribution of grain boundaries to the total hydrogen flux. Before annealing Marte [31] observed approximately 100 times the lattice diffusion coefficient of hydrogen in the metal; however, after annealing, structural relaxation of the grain boundaries resulting in them acting as trap sites for hydrogen with the effect that a lower diffusion coefficient was measured (approximately twice the lattice diffusion coefficient). Also, it is possible that flow down these defects is proportional to the inlet pressure. Hydrogen diffusion through nickel was found to increase with increasing hydrogen concentration at the inlet surface due to the presence of grain boundaries [31].

Figure 5.11, shows an increase in the apparent diffusion coefficients of Set B with increasing inlet pressure. The observed trend implies that the membrane is becoming more consistent with the data for the metal, with a reduction in the influence of the oxide overlayer at higher inlet pressures. One possible explanation for this is that before free transport of hydrogen through the oxide can occur some unspecified number of trap sites must first be occupied by diffusing hydrogen. Increasing the inlet pressure would be expected to fill these trap sites in a shorter time than at lower temperatures. From this we would not expect Set C to exhibit any inlet pressure dependence due to the sample being considered "clean". However, we would expect Sets A and D to exhibit inlet pressure dependences, due to the presence and influence of an oxide overlayer. Figure 5.12 shows the inlet pressure dependence of the calculated diffusion coefficients of Set A. The Arrhenius equations from Figures 5.11 and 5.12 are summarised in Table 5.7. It can be seen that there is excellent agreement between the calculated activation energies for diffusion for all of the inlet pressures measured (26.56 - 28.20 $kJmol^{-1}$), which is concomitant with the measured activation energy being related to diffusion through uranium metal. From a comparison of the calculated diffusion coefficients, with T_s = 623 K, it can be seen that for Set B, if the inlet pressure is trebled the associated diffusion coefficient will increase by approximately 2.5 times; however, for Set A, a five times increase in the inlet pressure only causes the associated diffusion coefficient to increase by approximately 1.5 times. This is consistent with the above

argument that the influence of the oxide is decreased for the thicker metal membrane. From these observations it is expected that by increasing the inlet pressure beyond a threshold value the influence of the oxide can be reduced to insignificant levels. Thus, allowing deuterium diffusion through the metal to be directly probed. By analogy, it would therefore be expected that Set C would not experience any inlet pressure dependence, due to the inlet surface being already saturated at relatively low pressures. whilst for the partially cleaned Set D we would expect an intermediate dependence between those observed for Sets A and B. However, we were not able to test this hypothesis due to the instabilities of the samples limiting the number of data points.

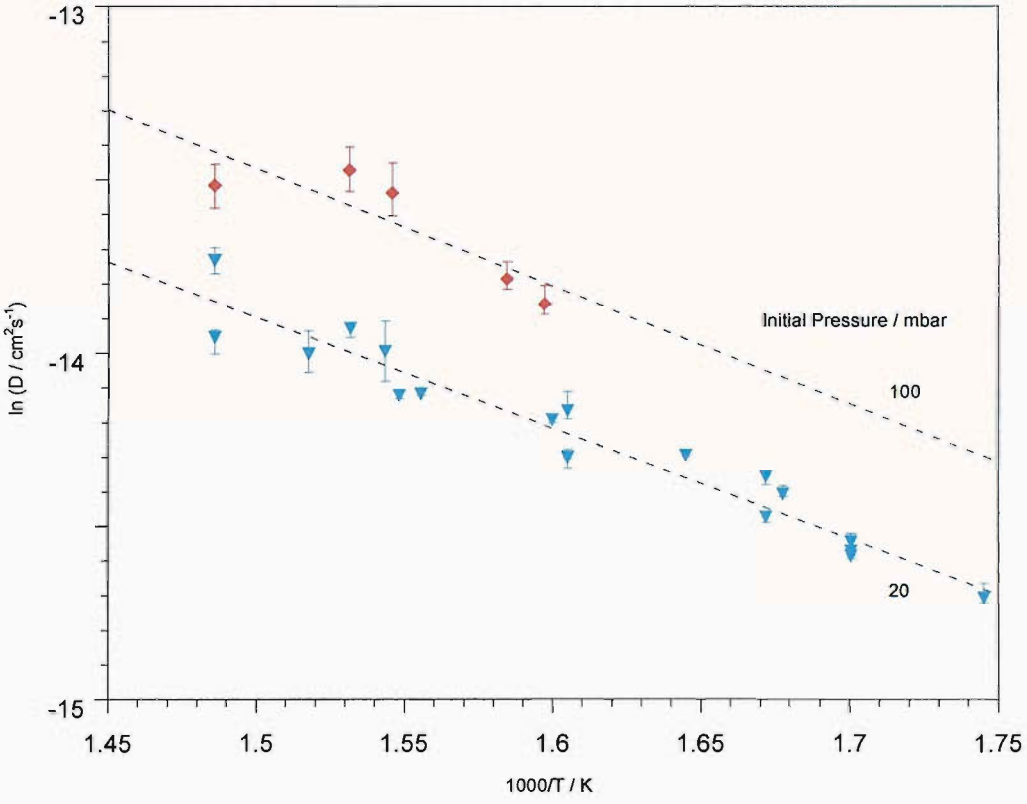

Figure 5.12 – Arrhenius plots for Set A at 20 (▼) and 100 (♦) mbar inlet pressures.

Set	Inlet Pressure / mbar	D_0 / cm^2s^{-1}	E_D / $kJmol^{-1}$	D / cm^2s^{-1} @ 623 K
A	20	1.12×10^{-4}	26.60	6.59×10^{-7}
	100	2.30×10^{-4}	28.22	9.90×10^{-7}
B	20	1.50×10^{-5}	26.56	8.89×10^{-8}
	40	3.80×10^{-5}	27.36	1.93×10^{-7}
	60	4.12×10^{-5}	27.10	2.20×10^{-7}

Table 5.7 – Summary of the D_0 and E_D values for sample Sets A and B, at various inlet pressures.

The presence of gas phase impurities in the dosing line might also affect the overall permeation process, both by affects on the surface and at grain boundaries. Bloch *et al* [33] studied the effect of oxygen and CO on the kinetics of uranium hydriding. They postulated that oxygen blocked the penetration (where penetration is the combined process of dissociation and transport) of hydrogen through the oxide overlayer, while CO adsorption blocked penetration through both the oxide and the hydride layers. If it is assumed that hydrogen dissociation generally occurs via surface defect sites, then it is likely that both the oxygen and the CO will preferentially adsorb at these defect sites reducing their accessibility for hydrogen adsorption and subsequent dissociation. This would be expected to lead to a decrease in the effective steady-state flux by reduction of the effective surface area available for permeation. Bulk impurities might also act as trap sites for hydrogen diffusion, increasing the observed time lags [31]. Dislocations and vacancies in aluminium have also been observed to act as hydrogen trap sites [34]. Lattice vacancies were found to have the higher binding energy and hence have more influence on hydrogen diffusion, e.g. $1x10^{-11}$ vacancies per lattice site was found to decrease hydrogen diffusion by a factor of 10 at 298 K. It is only after saturation of these traps sites that diffusion can occur via unaffected sites.

In summary, the apparent diffusion coefficient has been shown to be dependent on a number of factors. The main factor is the oxide to metal thickness ratio. For a given oxide overlayer thickness, the influence of the oxide increases as the metal thickness decreases, as evidenced by comparison of Sets A and B. Also, for a given metal

thickness, a reduction in the thickness of the oxide overlayer leads to an increase in the apparent diffusion coefficient towards a more metallic membrane, as seen by comparison of the results of Sets B, C and D.

Another factor to explain the observed diffusion data has been explained by a defective oxide overlayer. Diffusion through the oxide is not expected to be through oxide lattice sites because of the calculated low, metal-like activation energy for diffusion experienced by all sample Sets regardless of the oxide coverage. Therefore, oxide line defects or grain boundaries are considered to be the more likely pathway of deuterium diffusion through the oxide, but these pathways may also be populated by trap sites either inherent, due to the structure of the grain boundaries or line defects, or due to the presence of impurities. The filling of these trap sites may be responsible for the observed anomalous diffusion coefficient data. The presence of gas phase impurities may also lead to a blocking of surface defect sites, which will reduce the effective surface concentration of the hydrogen resulting in a lowering of the permeability.

5.5 Conclusions

Using the membrane Time Lag method the role of the uranium oxide overlayer in the permeation of deuterium through uranium metal has been investigated. From comparison with the literature, it has been established that the palladium coated Set C was a good representation of permeation through "clean" metal, Model (3). Sets A, B and D varied in metal membrane and oxide overlayer thickness. By consideration of these results a number of conclusions can be made about the deuterium diffusion process.

The coherent oxide overlayer model of Model (1) could not be applied to Sets A, B or D because of the calculated intermediate Sievert's exponents, which implied that the oxide overlayer present was heavily defective, as would be expected for Model (2). However, Model (2) covers a broad range of oxide overlayers that can vary in thickness and microstructure. Also, there appears to be a number of factors that

control the level of influence the oxide overlayer is seen to have on the diffusion process; the thickness of the oxide overlayer, the thickness of the metal membrane, the microstructure of the oxide overlayer and the level of impurities in the gas-phase and the bulk. It has also been noted that the inlet pressure has a inverse relationship with the level of oxide influence observed. By increasing the inlet pressure beyond a threshold value, it is expected that, the overall diffusion process will become purely dominated by diffusion through the metal.

The only factor found to be consistent between Sets was the calculated apparent activation energy of deuterium diffusion (~27 – 35 $kJmol^{-1}$), which we have associated with diffusion through uranium metal. From these factors, we can postulate some of the important steps in the diffusion of deuterium through a uranium membrane with a defective air-formed oxide overlayer on the inlet surface.

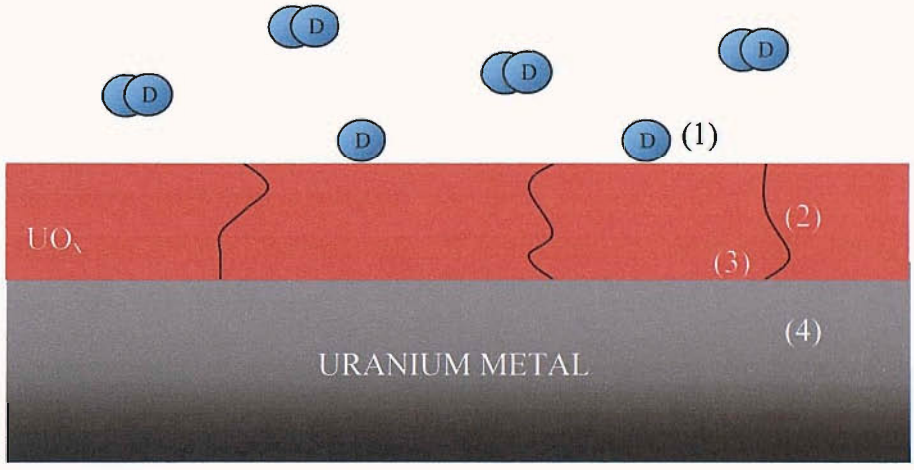

Figure 5.13 – Illustration of some of the important steps in the diffusion of deuterium through a uranium membrane with a defective oxide overlayer.

(1) The adsorption and dissociation of hydrogen on the oxide surface will be adversely affected by the presence of surface impurities blocking preferential dissociation sites. (2) It is expected that the deuterium species diffuse down low-energy pathways in the oxide overlayer, i.e. grain boundaries or line defects, rather than through oxide lattice sites. The presence of impurities might block these diffusion pathways, or even act as trap sites. Bulk trap sites, such as vacancies or dislocations must be filled before free transport through the oxide can occur, Step

(3). Once in the metal (4), the diffusion of deuterium occurs via metal lattice sites and becomes a relatively facile process.

5.6 References

[1] Haschke, J.M., T.H. Allen, L.A. Morales, J. Alloy. Compd. 314 (2001) 78-91.

[2] Haschke, J.M., J. Alloy. Compd. 278 (1998) 149-160.

[3] Bloch, J., M.H. Mintz, J. Alloy. Compd. 253-254 (1997) 529-541.

[4] Brill, M., J. Bloch, M.H. Mintz, J. Alloy. Compd. 266 (1998) 180-185.

[5] Arkush, R., A. Venkert, M. Aizenshtein, S. Zalkind, D. Moreno, M. Brill, M.H. Mintz, N. Shamir, J. Alloy. Compd. 244 (1996) 197-205.

[6] Moreno, D., R. Arkush, S. Zalkind, N. Shamir, J. Nuc. Mat. 230 (1996) 181-186.

[7] Balooch, M., W.J. Siekhaus, J. Nuc. Mat 255 (1998) 263-268.

[8] Shuai, M.B., H.R. Hu, X. Wang, P.J. Zhao, A.M. Tian, Journal of Molecular Structure-Theochem 536 (2001) 269-276.

[9] Allen, G.C., P.A. Tempest, Proc. R. Soc. London Ser. A-Math. Phys. Eng. Sci. 406 (1986) 325-344.

[10] Swissa, E., N. Shamir, M.H. Mintz, J. Bloch, J. Nuc. Mat. 173 (1990) 87-97.

[11] Bloch, J., E. Swissa, M.H. Mintz, Z. Phys. Chem. Neue Fol. 164 (1989) 1193-1198.

[12] Abrefah, J.D., D.F. Orlander, D.R., J. Phys. Chem. 94 (1990) 1937-1944.

[13] Wang, X., Y. Fu, R. Xie, J. Radioanalytical and Nuclear Chemistry 220 (1997) 113-116.

[14] Wheeler, V.J., J. Nuc. Mat. 40 (1971) 189-194.

[15] Aratono, Y., M. Nakashima, M. Saeki, E. Tachikawa, J. Nuc. Mat. 110 (1982) 201-207.

[16] Sherman, D.F., D.R. Olander, J. Nuc. Mat 166 (1989) 307-320.

[17] Mallett, M.W., M.J. Trezeciak, Trans. of the ASM 50 (1957) 981-993.

[18] Davis, W.D., GEC, Knolls Atomic Power Laboratory, New York, KAPL-1548, (1956)

[19] Powell, G.L., J.B. Condon, Oak Ridge Y-12 Plant, Union Carbide Corporation - Nuclear Division, Oak Ridge, Tennessee, Y-DA-5317, (1973)

[20] Ritchie, A.G., J. Nuc. Mat. 102 (1981) 170-182.

[21] Balooch, M., A.V. Hamza, J. Nuc. Mat. 230 (1996) 259-270.

[22] Yamakawa, K., M. Ege, B. Ludescher, M. Hirscher, H. Kronmuller, J. Alloy. Compd. 321 (2001) 17-23.

[23] Yamakawa, K., M. Ege, B. Ludescher, M. Hirscher, J. Alloy. Compd. 352 (2003) 57-59.

[24] Strehlow, R.A., H.C. Savage, Nuc. Tech. 22 (1974) 127-137.

[25] Crank, J., The Mathematics of Diffusion, Oxford, Oxford University Press, 1975.

[26] Katsuta, H., R.B. McLellan, K. Furukawa, J. Phys. Chem. Solids 43 (1982) 533-538.

[27] Nishimura, C., M. Komaki, M. Amano, J. Alloy. Compd. 293-295 (1999) 329-333.

[28] Atkins, P.W., Physical Chemistry, Oxford, Oxford University Press, 1998.

[29] Sicking, G., J. Less-Common Met. 101 (1984) 169-190.

[30] Jost, W., Diffusion in Solids, Liquids, Gases, New York, Academic Press, 1952.

[31] Marte, C., R. Kirchheim, Scripta Materialia 37 (1997) 1171-1175.

[32] Brass, A.M., A. Chanfreau, Acta Mater 44 (1996) 3823-3831.

[33] Bloch, J., D. Brami, A. Kremner, M.H. Mintz, J. Less-Common Met. 139 1988) 371-383.

[34] Young Jr, G.A., J.R. Scully, Acta Materialia 46 (1998) 6337-6349.

Chapter 6: Potential Energy Model of the Hydrogen/Uranium System

From these studies a potential energy model for the hydrogen/uranium system can be developed, Figure 6.1. The model is shown to contain ten parameters of which four have been determined experimentally in this study.

The TPD and supersonic molecular beam experiments in Chapter 4 allowed the clean uranium surface to be accurately probed. This model assumes that the hydrogen species desorbs from only one surface state, which is in agreement with the TPD spectra from Section 4.3.2. In the temperature range 160 – 800 K, only one hydrogen desorption feature was observed with the peak position decreasing from 450 to 410 K with increasing coverage. The desorption process was found to be approximately second – order with an activation energy (E_{des}) of 72 ± 10 $kJmol^{-1}$. This was in good agreement with the results of Balooch who determined E_{des} to be 79 ± 12 $kJmol^{-1}$ [1]. Note that in both cases a polycrystalline surface was investigated.

From the molecular beam studies the activation energy of hydrogen adsorption (E_a) can be estimated. The chemisorption of hydrogen onto clean uranium surfaces was found to be composed of two channels. The indirect dissociation channel decreases with increasing incident beam energy and "switches off" at ca. 250 meV. The opposing direct dissociation channel appears to be non-activated and steadily increases with increasing incident beam energy. Therefore, E_a is estimated to be 0 ± 20 meV, which equates to approximately 0 ± 1.93 $kJmol^{-1}$. The difference between the activation energies of adsorption and desorption is referred to as the heat of adsorption (ΔH_a). From this calculation a value of –74.58 ± 8.93 $kJmol^{-1}$ can be inferred.

The bulk kinetic and thermodynamic parameters were investigated in Chapter 5, using deuterium as the test gas in order to increase the sensitivity of the experimental measurements. The relative deuterium diffusion coefficients were calculated directly from measurements made using the Time Lag method. The

temperature dependence of this data allowed the activation energy of deuterium diffusion (E_D) to be calculated (26.56 - 35.39 $kJmol^{-1}$). This is in excellent agreement with the data presented by Davis (26.01 $kJmol^{-1}$ [3]).

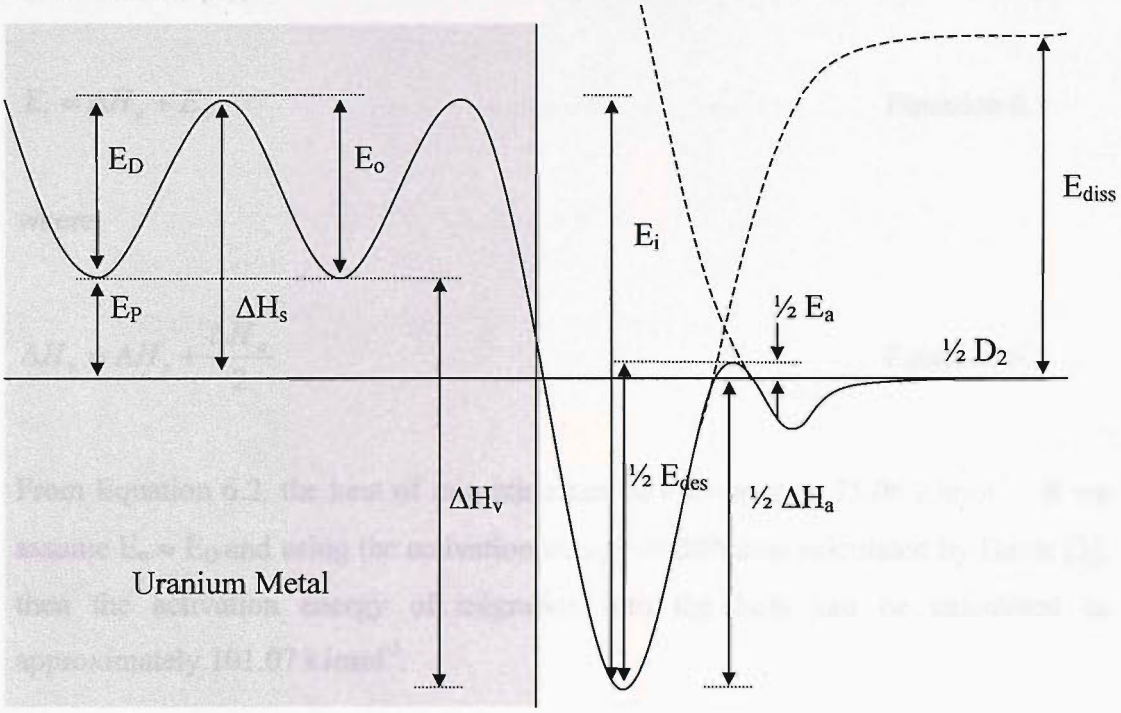

Figure 6.1 – Schematic of the hydrogen /uranium potential energy diagram.

	This Study / $kJmol^{-1}$	**Published Data / $kJmol^{-1}$**	**Estimated Values / $kJmol^{-1}$**
E_a	0 ± 1.93	-	-
E_{des}	74.58 ± 7	79 ± 12 [1]	-
ΔH_a	-74.58 ± 8.93	-	-
E_{diss}	-	443.50 [2]	-
E_i	-	-	101.07
ΔH_v	-	-	75.06
E_o	-	-	26.01
ΔH_s	-	37.77 [3]	-
E_P	-	63.77 [3]	-
E_D	26.56 – 35.39	26.01 [3]	-

Table 6.1 – Summary of the parameters contained within Figure 6.1

From this model, we can estimate the potentials controlling the transport between the surface and the bulk. The activation energy of migration into the bulk (E_i) is directly related to the heat of migration (ΔH_v) and the activation energy of migration to the surface (E_o):

$$E_i = \Delta H_v + E_o \qquad \text{Equation 6.1}$$

where,

$$\Delta H_v \approx \Delta H_s + \frac{\Delta H_a}{2} \qquad \text{Equation 6.2}$$

From Equation 6.2, the heat of migration can be estimated as 75.06 $kJmol^{-1}$. If we assume $E_o \approx E_D$ and using the activation energy of diffusion calculated by Davis [3], then the activation energy of migration into the bulk can be calculated as approximately 101.07 $kJmol^{-1}$.

The addition of an oxide overlayer onto the metal would greatly complicate the above potential energy model. From Section 4.3.3, we can see that there appears to be three desorption channels attributed to the presence of an oxide overlayer. Consequently, hydrogen dissolved in the metal may move to the surface and desorb by a different pathway to the adsorbed species. However, from the permeation experiments of Chapter 5 it has been established that for an air-formed oxide overlayer the preferential diffusion pathway through the oxide appears to be down oxide defects, such as grain boundaries or line defects, rather than through oxide lattice sites, which has a high associated activation energy of diffusion (60 – 76 $kJmol^{-1}$ [4; 5]). It is also complicated by the presence of surface and bulk trap sites, which must be filled before free transport through the oxide can occur, as evidenced by an increase in the measured time lag with increasing oxide influence and by the inlet pressure dependence of the deuterium diffusion coefficients of Sets A and B.

6.1 References

[1] Balooch, M., A.V. Hamza, J. Nuc. Mat. 230 (1996) 259-270.

[2] Lloyd, P.B., J.W. Kress, B.J. Tatarchuk, Applied Surf. Sci. 119 (1997) 275-287.

[3] Davis, W.D., GEC, Knolls Atomic Power Laboratory, New York, KAPL-1548, (1956)

[4] Aratono, Y., M. Nakashima, M. Saeki, E. Tachikawa, J. Nuc. Mat. 110 (1982) 201-207.

[5] Wheeler, V.J., J. Nuc. Mat. 40 (1971) 189-194.

Chapter 7: Further Work

There are a number of questions and issues, which have risen during this investigation, which we would have liked to answer.

From Chapter 4, the main issue still outstanding is the peak assignment for the oxide-covered surface. The most probable peak assignment has been established from the available data. However, there are a few TPD experiments, which we would have liked to perform. Pre-dosing with hydrogen before exposing to oxygen and dosing water would have given further information concerning whether the desorption peaks we observed were related to hydroxyl or sub-oxide hydrogen species. Also, we would like to have tried to charge the sample with hydrogen in an attempt to observe the desorption temperature of bulk hydrogen species; how is this affected by the presence of an oxide overlayer?

Also, there were a number of questions still remaining from Chapter 5. Palladium coating the inlet surface of a pre-cleaned sample has been shown to allow the diffusion of deuterium through "clean" uranium metal to be probed without interference from the oxide overlayer. We would have liked to have taken this further and completely cleaned the surface of a sample using sputter/anneal cycles, as used in Chapter 4, prior to deposition of the palladium film. Again the palladium-coated surface would have formed the inlet surface during experiments. It is then proposed that the exit surface would also be sputter/anneal cleaned before a series of permeation experiments performed; is the data in better agreement with that reported by Davis? An oxide overlayer can then be grown on the exit surface. Do the diffusion coefficients change as expected from the results of an air-formed oxide overlayer, decreasing diffusion coefficient with increasing oxide thickness? For an oxygen grown oxide, does diffusion through the oxide appear to be switching from grain boundaries or line defects to lattice sites? Does the activation energy of diffusion change for an oxygen grown oxide?

Appendix A: The Hard-Cube Model

For a molecule to be successfully trapped on a surface it must lose sufficient normal kinetic energy either by transference to the surface (classical) or to another degree of freedom (selective adsorption, resonance). The ability of a surface to absorb the kinetic energy of a molecular collision has been successfully modelled using the classical hard-cube model. The first theoretical studies of Goodman [1], Trilling [2] and Oman [3] neglected the thermal motion of the surface during collision and therefore, could not account for the net energy transfer from the gas to the surface.

In order to address these shortcomings, Logan and Stickney [4] proposed a model that was based on a few basic assumptions:

- An impulsive force of repulsion represents the interaction of a gas species and a surface, i.e. the gas and surface particles can be considered to be rigid elastic particles.
- The potential energy well for a gas-surface interaction is uniform across the surface, indicating a perfectly flat surface. The tangential velocity remains unchanged and thus there are no forces acting parallel to the surface.

In order for these two assumptions to be combined it becomes convenient for the surface atoms to be considered as cubes with motion only in the direction normal to the surface. The gas particle (spherical, rigid and elastic) only interacts with one surface cube, with the normal velocity changing according to Newton's laws.

- The surface atoms are represented by independent particles (cubes) confined by square-well potentials (rigid boxes). The impinging gas particle enters the box and interacts with a surface cube before departing.
- A Boltzmann distribution was assigned to the normal velocity of the surface cubes.

One of the main results of this approach is that for only a single collision to occur the mass ratio of the gas to the surface particles must be less than 1/3, which is not as much of a restriction as in practise this is often the case.

The Molecular Velocity In The Potential Well

The velocity of molecule V_{vac} impinging on a surface, with a square potential of well depth U, will be accelerated by V_{add} as a result of the well.

$$V_{vac} = -\sqrt{\frac{2E_i}{M}} \qquad \text{Equation A.1}$$

$$U = \frac{MV_{add}^2}{2} \qquad \text{Equation A.2}$$

where, M is the mass of the incident particle. Note that velocities are defined as positive for particles moving away from the surface and negative when impinging. The resulting velocity of the particle on impact with the surface is:

$$V_{well} = -\sqrt{\left(V^2 + \frac{2U}{M}\right)} \qquad \text{Equation A.3}$$

The Molecular Velocity After Collision With The Surface

From the conservation of momentum:

$$MV_{well} + mV_{cube} = MV'_{well} + mV'_{cube} \qquad \text{Equation A.4}$$

where, V_{cube} is the velocity of the surface cube before the collision, V'_{well} and V'_{well} are the respective velocities after collision and m is the mass of the surface sites. From Newton's experimental law for an elastic collision:

$$V_{well} + V_{cube} = V'_{well} + V'_{cube} \qquad \text{Equation A.5}$$

substituting Equation A.5 into Equation A.4 gives:

$$MV_{well} + mV_{cube} = MV'_{well} + m\left(V'_{well} - V_{cube} + V_{well}\right) \qquad \text{Equation A.6}$$

$$MV'_{well} + mV'_{well} = MV_{well} - mV_{well} + 2mV_{cube} \qquad \text{Equation A.7}$$

dividing by m gives:

$$\mu V'_{well} + V'_{well} = \mu V_{well} - V_{well} + 2V_{cube} \qquad \text{Equation A.8}$$

$$V'_{well}(\mu + 1) = V_{well}(\mu - 1) + 2V_{cube} \qquad \text{Equation A.9}$$

Hence:

$$V'_{well} = \frac{V_{well}(\mu - 1) + V_{cube}}{(\mu + 1)} \qquad \text{Equation A.10}$$

where, μ is the reduced mass.

Velocity Of The Cube Below Which The Impinging Molecule Will Trap

The energy required to escape the potential well after collision is U. Therefore, the minimum velocity required is:

$$V_{escape} = \sqrt{\frac{2U}{M}} \qquad \text{Equation A.11}$$

To remain trapped in the well, $V'_{well} < V_{escape}$. Therefore:

$$\frac{V_{well}(\mu - 1) + V_{cube}}{(\mu + 1)} < \sqrt{\frac{2U}{M}} \qquad \text{Equation A.12}$$

$$V_{cube} < \frac{(\mu+1)}{2}\sqrt{\frac{2U}{M}} - \frac{V_{well}(\mu-1)}{2}$$ Equation A.13

substituting in Equation A.3 gives:

$$V_{cube} < \frac{(\mu+1)}{2}\sqrt{\frac{2U}{M}} + \frac{(\mu-1)}{2}\sqrt{\left(V_{vac}^2 + \frac{2U}{M}\right)}$$ Equation A.14

If we state that:

$$V_{\lim it} = \frac{(\mu+1)}{2}\sqrt{\frac{2U}{M}} + \frac{(\mu-1)}{2}\sqrt{\left(V_{vac}^2 + \frac{2U}{M}\right)}$$ Equation A.15

Then for trapping to occur:

$$V_{cube} < V_{\lim it}$$ Equation A.16

Fraction Of Surface Cubes Capable Of Collision And Trapping A Particle

The probability of a surface cube having velocity v (P(v)) is dependent in the energy of the state (E) and the surface temperature (T_s). The Boltzmann distribution is used to depict the probability of occupying a particular state. From this the probability of a surface cube being capable of collision and having a velocity below V_{limit} is:

$$P_c(v) = \int_{-\infty}^{V_{\lim it}} Pc(v).P(v)dv$$ Equation A.17

where, Pc(v) is the probability of a particle colliding with a surface cube of velocity v. The probability of a surface cube have velocity v (P(v)) is:

$$P(v) = \frac{\exp\left(-\frac{mv^2}{2kt}\right)}{Q}$$ Equation A.18

where, Q is the partition function:

$$Q = \int_{-\infty}^{+\infty} \exp\left(-\frac{mv^2}{2kt}\right) dv \qquad \text{Equation A.19}$$

Using the standard integral:

$$\int_{0}^{+\infty} \exp\left(-bv^2\right) dv = \frac{1}{2}\sqrt{\frac{\pi}{b}} \qquad \text{Equation A.20}$$

and letting:

$$a^2 = \frac{m}{2kt} \qquad \text{Equation A.21}$$

Hence, Equation A.20 becomes:

$$\int_{0}^{+\infty} \exp\left(-a^2v^2\right) dv = \frac{1}{2}\sqrt{\frac{\pi}{a^2}} \qquad \text{Equation A.22}$$

From this:

$$Q = \frac{\sqrt{\pi}}{a} \qquad \text{Equation A.23}$$

substituting Equation A.23 into Equation A.18:

$$P(v) = \frac{a}{\sqrt{\pi}} \exp\left(-a^2v^2\right) \qquad \text{Equation A.24}$$

If the surface is moving away from the impinging particle then the probability will be small, being zero if the surface is moving with the same velocity as the impinging

particle (V_{well}). The maximum probability will be when the surface and the particle are moving towards each other. Hence:

$$Pc(v) = \frac{V_{well} - v}{V_{well}} = 1 - \frac{v}{V_{well}} \qquad \text{Equation A.25}$$

substituting Equations A.24 and A.25 into Equation A.17:

$$P_c(v) = \int_{-\infty}^{V_{limit}} \left(1 - \frac{v}{V_{well}}\right)\left(\frac{a}{\sqrt{\pi}}\exp\left(-a^2v^2\right)\right)dv$$

$$= \int_{-\infty}^{V_{limit}} \left(\frac{a}{\sqrt{\pi}}\exp\left(-a^2v^2\right)\right)dv - \int_{-\infty}^{V_{limit}} \frac{v}{V_{well}}\left(\frac{a}{\sqrt{\pi}}\exp\left(-a^2v^2\right)\right)dv \qquad \text{Equation A.26}$$

Using the identity:

$$\int_{-\infty}^{z} dv = \int_{-\infty}^{0} dv + \int_{0}^{z} dv \qquad \text{Equation A.27}$$

$$\int_{-\infty}^{V_{limit}} \left(\frac{a}{\sqrt{\pi}}\exp\left(-a^2v^2\right)\right)dv = \frac{a}{\sqrt{\pi}}\left(\int_{-\infty}^{0}\exp\left(-a^2v^2\right)dv + \int_{0}^{V_{limit}}\exp\left(-a^2v^2\right)dv\right)$$

Equation A.28

As, $\exp(-x^2)\{0,\infty\}$ is a reflection of $\exp(-x^2)\{0,-\infty\}$, then:

$$\int_{-\infty}^{0}\exp\left(-a^2v^2\right)dv = \int_{0}^{-\infty}\exp\left(-a^2v^2\right)dv = \frac{1}{2}\sqrt{\frac{\pi}{a^2}} \qquad \text{Equation A.29}$$

Hence:

$$\int_{-\infty}^{0}\frac{a}{\sqrt{\pi}}\exp\left(-a^2v^2\right)dv = \frac{1}{2} \qquad \text{Equation A.30}$$

Using the identity:

$$erf(z) = \frac{2}{\sqrt{\pi}} \int_0^z \exp(-x^2)dx \qquad \text{Equation A.31}$$

and by substituting in $u = av$:

$$\int_0^z \exp(-x^2)dx = \int_0^{av} \exp(-u^2)\frac{dv}{du}du \qquad \text{Equation A.32}$$

Therefore,

$$\int_0^{V_{\lim it}} \exp(-a^2v^2)dv = \frac{\sqrt{\pi}}{2a} erf(aV_{\lim it}) \qquad \text{Equation A.33}$$

Using Equations A.29 and A.33, Equation A.28 becomes:

$$\int_{-\infty}^{V_{\lim it}} \left(\frac{a}{\sqrt{\pi}}\exp\left(-a^2v^2\right)\right)dv = \frac{a}{\sqrt{\pi}}\left(\frac{1}{2}\frac{\pi}{\sqrt{a^2}} + \frac{\sqrt{\pi}}{2a} erf(aV_{\lim it})\right)$$

$$= \frac{1}{2} + \frac{1}{2} erf(aV_{\lim it}) \qquad \text{Equation A.34}$$

$$\int_{-\infty}^{V_{\lim it}} \frac{V}{V_{well}}\left(\frac{a}{\sqrt{\pi}}\exp(-a^2v^2)\right)dv = \frac{a}{\sqrt{\pi}V_{well}} \int_{-\infty}^{V_{\lim it}} v\exp(-a^2v^2)dv \qquad \text{Equation A.35}$$

By substituting $u = -a^2v^2$ and $\frac{dv}{du} = -2a^2v$:

$$\frac{a}{\sqrt{\pi}V_{well}} \int_{-\infty}^{V_{\lim it}} v\exp(-a^2v^2)dv = \frac{a}{\sqrt{\pi}V_{well}} \int_{-\infty}^{V_{\lim it}} v\exp(u)\frac{dv}{du}du$$

$$= \frac{a}{\sqrt{\pi V_{well}}} \int_{-\infty}^{-a^2 V_{\lim it}} \frac{v}{-2a^2 v} \exp(u) du$$

$$= \frac{1}{2a\sqrt{\pi V_{well}}} \int_{-\infty}^{-a^2 V_{\lim it}} \exp(u) du \qquad \text{Equation A.36}$$

$$= \frac{1}{2a\sqrt{\pi V_{well}}} \exp(-a^2 V_{\lim it}^2)$$

By substituting Equations A.34 and A.36 into Equation A.26, the trapping probability becomes:

$$P_c(v) = \frac{1}{2} + \frac{erf(aV_{\lim it})}{2} + \frac{\exp(-a^2 V_{\lim it}^2)}{2a\sqrt{\pi V_{\lim it}}} \qquad \text{Equation A.37}$$

References

[1] Goodman, F.O., Proc. Intern. Symp. Rarefied Gas Dyn. 4th Toronto 1964 2 (1965) 366.

[2] Trilling, L., J. de Mecanique 3 (1964) 215.

[3] Oman, R.A., A. Bogan, C.H. Li, Proc. Intern. Symp. Rarefied Gas Dyn. 4th Toronto 1964 2 (1965) 396.

[4] Logan, R.M., R.E. Stickney, J. Chem. Phys. 44 (1966) 195-201.